The Structure of the Crust and Distribution of Earthquakes in Southern California

Thesis by

Julie Jeannine Nazareth

In Partial Fulfillment of the Requirements

for the degree of

Doctor of Philosophy

California Institute of Technology

Pasadena, California

2002

(Defended December 5, 2001)

Acknowledgements

I would like to thank everyone who believed in me, even when I did not believe in myself. I would not be here today, writing these last few sentences of my Ph.D. thesis, if it were not for their support and encouragement. I would like to especially thank my advisors Rob Clayton and Egill Hauksson. Thank you for always listening and for caring about more than just the research. I would also like to thank the people at Caltech who made my graduate experience about more than just academics and science, yet contributed to both in more ways than they probably realized - my office mates, fellow students, the administrative and support staff, the professors, members of the Pasadena USGS office, the Lovewaves softball team(s), and many others too numerous to name. Thanks to Caltech, the Southern California Earthquake Center (SCEC), and especially my advisors for supporting my research through the long years. I would like to thank Jeanne Hardebeck for all of the interesting discussions we had about static stress as we prepared for our oral qualifying exams, and especially for all of her hard work and leadership on our collaborative research on the static stress change triggering of earthquakes model (chapter 4). I thank my thesis committee (Rob Clayton, Mike Gurnis, Egill Hauksson, Hiroo Kanamori, and Joann Stock) and other members of the Seismo Lab through the years who have offered many helpful comments on my work. Special thanks must go out to Katrin Hafner, Patricia Persaud, Magali Billen, and Martha Kuykendall, for all of those wonderful and numerous conversations we had, but especially for listening and caring. Thanks to my family (both of blood and through marriage) for their support and encouragement. Last but not least, I would like to thank my husband Sean for all his unwavering love, encouragement, support, sacrifice, and especially patience throughout the long years.

Abstract

The lithologically and tectonically complex crust of southern California and the current broad deformation zone accommodating the relative motion between the Pacific and North American plates, result in significant variations in style, depth distribution, and rate of earthquakes, and thus also in the seismic hazard across southern California. Although the thickness of the seismogenic crust is an important parameter in seismic hazard analysis, it has never been determined systematically for southern California. Seismogenic thickness can be predicted by the depth distribution of the moment release of regional seismicity. The seismogenic thickness of southern California is highly variable, ranging from less than 10 km in the Salton Trough to greater than 25 km at the southwestern edge of the San Joaquin Valley. On average, the seismogenic thickness of southern California is 15.0 km. Seismogenic thickness along the major strike slip systems of southern California can vary significantly along strike. Fault segmentation based upon surface features does not correspond to the variation in seismogenic thickness and thus the potential down-dip width of the fault. A model of the broad scale features of the crust and upper mantle structure of the borderland-continent transition zone adjacent to Los Angeles constrains the crustal thickness and the location and width of the transition zone. The data require the Moho to deepen significantly to the north, dramatically increasing the crustal thickness over a relatively short distance of 20-25 km. The Moho is coherent and laterally continuous beneath the Inner California Borderland and transition zone. The Inner Borderland seems to be modified and thickened oceanic crust, with the oceanic upper mantle intact beneath it. The static stress change triggering model has some validity and can be useful in explaining apparently triggered seismicity within one fault length of a large

mainshock. However, because its applicability varies between different sequences, its general application to seismic hazard evaluation requires more refinement and the inclusion of parameters such as tectonic regime, regional stress state, and fault strength.

Table of Contents

List of Figures

List of Tables

CHAPTER 1 *Summary*

The tectonically and lithologically complex crust of southern California is a rich tapestry that tells the story of both the current and past deformation of this portion of the western margin of North America. Each phase of deformation intertwines with the previous ones and influences the future ones. Although subduction ceased off the coast of southern California approximately 28 Ma, the legacy of 200 m.y. of subduction on the continent remains in the crustal structure and rocks of the great batholiths, sedimentary basins, and metamorphic complexes. The current broad zone of deformation accommodating the relative motion between the Pacific and North American plates is overwriting the remnants of the subduction boundary with the story of an evolving transform boundary. As the crust is cut and modified by today's active faults, the tapestry, and the story it tells, continues to evolve.

This thesis looks at the structure of the crust of southern California and the current state of deformation as described by the distribution and occurrence of earthquakes. The different chapters view the crust at different length scales and vary in scope of study. Chapter two looks at the seismogenic thickness of the crust for all of southern California,

yet views the crust in detail (large scope, small length scale). The third chapter is concerned with the broad scale crust-upper mantle structure of one region of southern California (moderate scope, large length scale). Chapter four tests the static stress triggering model for two southern California aftershock sequences (small scope, small length scale).

In chapter two, the thickness of the seismogenic crust is quantitatively estimated in a systematic fashion for all of southern California from the depth distribution of the moment release of ~19 years of seismicity. The thickness of the seismogenic crust is an important parameter in seismic hazard analysis. Improving the accuracy of this parameter is key to improving the seismic hazard estimate and possibly reducing the overall uncertainty. Additionally, a detailed estimate of the seismogenic thickness is important because the largest ground motions at a site are not always due to the largest potential earthquake in the region (e.g., a large earthquake on the San Andreas fault similar to the 1857 earthquake in magnitude and rupture length), but can result from a smaller earthquake on a closer fault.

The technique is calibrated by comparing the maximum depth of rupture during moderate to large magnitude southern California earthquakes to the pre-mainshock background seismicity of the mainshock region. The depth above which 99.9% of the moment release of seismicity occurs reliably estimates the maximum depth of rupture during moderate to large earthquakes (as described by published finite source models). These moderate to large magnitude events contain most of the seismic moment release and thus contribute most to the seismic hazard of a region. Therefore, from a seismic hazard standpoint, seismogenic thickness is synonymous with the maximum depth of rupture during

these larger earthquakes, and thus, the seismogenic thickness can be estimated in a systematic and widespread fashion for southern California from the seismicity of the region.

The seismogenic thickness of southern California is estimated from two different viewpoints which provide varying levels of detail. The regional view uses 0.1°x0.1° bins to divide up southern California on an even grid, covering as much area of southern California as possible at a reasonable level of detail. The fault view concentrates on the along strike details of the three major strike-slip fault systems of southern California (the San Andreas fault system, the San Jacinto fault system, and the Elsinore fault system), providing detailed estimates of seismogenic thickness for these high seismic potential faults whose relatively high seismicity rates support a high level of detail.

The seismogenic thickness of southern California is highly variable, ranging from less than 10 km in the Salton Trough to greater than 25 km at the southwestern edge of the San Joaquin Valley. On average, the seismogenic thickness of southern California is 15.0 km (+1.2/-1.1 km). Seismogenic thickness along the major strike slip systems can vary significantly along strike, even within defined fault segments. Surface segmentation of these major strike-slip faults does not reflect the variation in seismogenic thickness and the potential down-dip width of the fault. For seismic hazard purposes, segmentation should be redefined to better represent the both the potential lengths and down-dip widths of the rupture surfaces of these faults.

The third chapter discusses the crustal structure of the oceanic borderland-continent transition zone adjacent to Los Angeles. This region is the physical boundary between the ocean and the land, and therefore, the observational data, especially crustal

scale seismic data, is limited. From a geological point of view, the transition zone is merely a description for the region where the crust changes from the structure and (~20 km) thickness of the Inner California Borderland to that of the (~30 km) "southern California crust."

Seismic refraction data from the onshore-offshore component of LARSE (Los Angeles Region Seismic Experiment) is used to model the broad scale features of the mid-crust to upper mantle beneath a north-south transect that spans the borderland. Rather than develop a single velocity model that satisfies the data, I explore the end member structural models that define the range of possible velocity models that satisfy the data. This approach is not required by the data, but rather is an attempt to better understand what constraints on crustal structure the data provides, and what it does not.

A composite velocity model constrains the crustal thickness and location and width of the transition zone. The data require the Moho to deepen significantly to the north, dramatically increasing the crustal thickness over a relatively short distance of 20-25 km. The strong, coherent, and continuous Pn phase seen in the LARSE data indicates the Moho is coherent and laterally continuous beneath the Inner California Borderland and transition zone. The Inner Borderland seems to be modified and thickened oceanic crust, with the oceanic upper mantle intact beneath it.

Chapter four contains a test of the static stress triggering model. This study was conducted by a fellow student, Jeanne Hardebeck, and myself, and was published in 1998 (*Journal of Geophysical Research*, vol. 103, p. 24427-24437). We use the 1992 M_w 7.3 Landers and the 1994 M_w 6.7 Northridge earthquake sequences to quantitatively test static

stress change as a mechanism of earthquake triggering. Specifically, we test whether the fraction of aftershocks consistent with static stress change triggering is greater than the fraction of random events which would appear consistent by chance. Although static stress changes appear useful in explaining the triggering of some aftershocks, the model's capability to explain aftershock occurrence varies significantly between sequences. The model works well for Landers aftershocks. Approximately 85% of the events between 5 and 75 km distance from the mainshock fault plane are consistent with static stress change triggering, compared to ~50% of random events. The minimum distance is probably controlled by limitations of the modeling, while the maximum distance may result because static stress changes of <0.01 MPa trigger too few events to be detected. The static stress change triggering model, however, cannot explain the first month of the Northridge aftershock sequence significantly better than it explains a set of random events. The difference between the Landers and Northridge sequences may result from differences in fault strength, with static stress changes being a more significant fraction of the failure stress of weak Landers-area faults. Tectonic regime, regional stress levels, and fault strength may need to be incorporated into the static stress change triggering model before it can be used reliably for seismic hazard assessment.

The static stress change triggering model helps us to better understand how the stress release from one fault affects another. Although quantitative tests show that the model works to varying degrees, the static stress change triggering model can still contribute to seismic hazard assessment. Static stress triggering is a part of the earthquake process, but not the only component. These tests have simply shown us what we always have known, but never like to admit - the earth is a wonderfully complicated place.

CHAPTER 2

Quantitative Constraints on Seismogenic Thickness in Southern California

2.1 Introduction

Although the thickness of the seismogenic crust is an important parameter in seismic hazard analysis, it has never been determined systematically for southern California. The lithological and tectonic complexity of the southern California crust results in the significant variations in style, and depth distribution of seismicity across the region. Seismic hazard analysis is a challenge in not only identifying and mapping faults on the surface, but also in determining their depth extent.

Much of southern California lies in the broad zone of deformation along the Pacific-North America plate boundary (Figure 2.1). Faulting is not restricted to a single major transform fault (the San Andreas fault), nor even the three major strike-slip systems south of the Transverse Ranges (the San Andreas, San Jacinto, and Elsinore fault systems), but is distributed across more than two-thirds of the width of the state. Most of the major faults can be traced on the surface, but their depth extent is uncertain or unknown. Scientists and the inhabitants of southern California have become painfully aware in the last 20 years that not all faults have a surface trace but can pose a substantial seismic haz-

ard nonetheless (e.g., "blind thrusts" and offshore faults). Unfortunately, these faults do not always become apparent until they rupture in a damaging earthquake. In southern California, the majority of moderate-large earthquakes in the last 20 years have occurred off the major known fault systems, where most of the seismic hazard is projected to come from.

One of the reasons why the seismic hazard may be underestimated is that there is a lack of information (especially the depth extent) away from the major studied fault systems. For faults with known orientations, but without aligned seismicity, the seismogenic thickness can be used to calculate the down-dip width of the fault, and thus improve the estimate of maximum rupture area for a given fault. For regions where the nature of the faults is not precisely known, seismogenic thickness can provide a bound on the depth extent of rupture. A better estimation of rupture area and potential moment release is critical for all of southern California because waveform modeling of various fault rupture scenarios for sites in the Los Angeles region shows that the largest ground motions result from rupture on the nearest fault to the site rather than a larger earthquake on the San Andreas fault [*Eisner*, 2001].

Although previous studies in California have linked the depth of hypocenters to physical factors that affect crustal rheology [*Doser and Kanamori*, 1986; *Sanders*, 1987; *Miller and Furlong*, 1988; *Hill et al.*, 1990; *Sanders*, 1990; *Magistrale and Zhou*, 1996], they do not take the next step and reverse the process, predicting the brittle behavior of the crust in a widespread fashion based upon the influencing factor or factors of their study. A combination of physical factors seem to influence the depth extent of brittle fracture

within the crust, so individual physical factors are indirect evidence at best. The only direct measurement of brittle fracture within the crust is earthquakes.

Using earthquakes as a measure of brittle fracture is not a new idea. Scientists have used along fault projections of hypocenters to visually estimate the down-dip width of major faults (e.g., *Peterson et al.*, [1996]). *Magistrale and Zhou* [1996], apparently qualitatively compared the depth extent of background seismicity to that of the aftershock zone (as proxy for maximum depth of mainshock rupture) of major earthquakes in southern California, and concluded that the depth extent of rupture during future earthquakes could be determined from the background seismicity. Prior systematic, quantitative studies estimating the down-dip width of faults, or seismogenic thickness are lacking.

This study was initiated to estimate the thickness of the seismogenic crust in a systematic fashion for all of southern California, using the relatively widespread and abundant information we already possess on brittle fracture in the crust – *earthquakes*. We use the depth distribution of earthquakes to estimate the maximum depth of rupture for moderate to large earthquakes. We focus on the maximum depth of rupture in moderate to large earthquakes because they contain most of the seismic moment release and thus contribute the most to the seismic hazard of a region.

We define the maximum depth of rupture to be the depth above which, the vast majority of the moment release (or hypocenters) within a depth column occurs. The term "vast majority" is not easy to define. Previous studies have used the depth above which a certain percentage of hypocenters occur (e.g., 90%, *Miller and Furlong*, 1988; 95%, *Williams*, 1996). Unfortunately, there is no justification given for the choice of percentage, so it is unclear just what this depth means in terms of brittle failure. In this study, we equate

the maximum depth of rupture with the *percent depth*, the depth above which, a quantitatively determined percentage of moment release (or hypocenters) occurs. We emphasize the moment release over hypocenters because the hypocenter distribution tells us where earthquake rupture starts in the crust, while the moment release distribution tells us about where earthquakes rupture in the crust.

2.2 *Previous Seismic Hazard Models*

Seismic hazard assessments use seismic moment release to measure the seismic potential of a fault or a region. A model of the sources of seismic hazard describes the magnitude, location and rate of earthquakes that pose a significant hazard to the region in question. The seismic hazard source model is used to calculate the probability of damaging ground motions.

As the foundation of the seismic hazard assessment, improving the definition of the seismic hazard source model is key to improving the hazard estimate and possibly reducing the overall uncertainty. In the past, scientists have focused on the major strike-slip fault systems with sufficient geological and historical earthquake data to create a seismic hazard source model [*WGCEP*, 1988]. Expected magnitudes on the fault segments were based upon informed opinion, and rounded to the nearest half magnitude unit.

In the Southern California Earthquake Center (SCEC) Phase II report [1995], the *Working Group on California Earthquake Probabilities* updated the 1988 report with new data and expanded the model to consider seismic sources from all of southern California, providing the first "Master Model." The study divided southern California into sixty-five seismotectonic zones and combined geodetic, geological, and seismicity data to estimate the seismic hazard of each zone. Seismic moment release was calculated from a combina-

tion of characteristic earthquakes on major faults, and distributed events defined by a modified Gutenberg-Richter distribution.

Seismogenic thickness was a key component of both the characteristic and distributed earthquake moment rate contribution. A major assumption of the study is that the thickness of the brittle crust is 11 km, chosen so that the predicted moment rate would agree with that from the historic earthquake catalog since 1850. The authors reasoned that negligible seismic moment release or aseismic deformation would occur in the top few kilometers of the crust in the sedimentary section, so a thickness of 11 km would be "consistent with the deepest earthquakes" of southern California.

Rather than assuming a constant seismogenic thickness, or estimating the maximum magnitude of a fault segment from its surface length, two succeeding seismic hazard studies used the updated CDMG/USGS fault database that includes down-dip width estimates for simplified fault traces [*Peterson et al.*, 1996; *Field et al.*, 1999]. The depth of the seismogenic rupture zone was estimated from the hypocenters of earthquakes surrounding the faults. The database also lists rupture top and bottom, but except for "blind" thrusts of the Transverse Ranges and Los Angeles basin and the Brawley Seismic Zone in the Salton Trough, the top of the rupture plane coincides with the surface of the earth. The maximum magnitudes for most of the fault segments are calculated from the fault-area regression of *Wells and Coppersmith* [1994].

Field et al. [1999] presented a new seismic hazard source model for southern California that satisfies regional moment and historical seismicity rates without requiring great earthquakes, aseismic strain release, or an anomalously low seismicity rate in the last 150 years. This model was created in response to the apparent earthquake deficit (M6-7) in the

historical catalog suggested by the SCEC Phase II report [*WGCEP*, 1995]. The model is based upon the fault segmentation, segment length, down-dip width, and slip rate for the 95 southern California fault segments of the CDMG/USGS fault database [*Peterson et al.*, 1996]. Geological moment rate is explicitly conserved on each fault segment as well as for the whole southern California region. The magnitudes for the various rupture scenarios are computed from the fault area regression formula of *Wells and Coppersmith* [1994].

2.3 Data

Our dataset consists of 257,918 earthquakes recorded by the Southern California Seismic Network between April 1981 and July 2000 and range in magnitude from 0.1 to 7.3 (Figure 2.2). These earthquakes have been relocated using the 3-D velocity model of *Hauksson* [2000], so biases due to the effects of 3-D crustal structure are removed. This earthquake dataset represents a significant improvement over the seismic network catalog which is located using a 1-D velocity model and other previous relocated catalogs covering limited areas.

Figure 2.3 shows the range in horizontal error, vertical error, number of observations, and RMS residual for our initial dataset of 333,085 earthquakes. We rejected 75,167 events because they did not satisfy one or more of the following criterion: 1) the hypocenter must be vertically constrained; 2) vertical error in the location of the hypocenter must be equal to or less than 2.0 km; 3) the horizontal error of the hypocenter cannot exceed 1.5 km; 4) the earthquake must be recorded by at least 10 stations, unless the distance to the nearest station is less than twice the depth of the hypocenter; 5) the magnitude must be constrained. The allowed vertical error is larger than the horizontal error to allow for better spatial coverage in our dataset. Although we allow earthquakes to have horizon-

tal and vertical errors up to 1.5 and 2.0 km, respectively, 86% of the earthquakes have a horizontal error of less than or equal to 0.5 km, and 87% of the earthquakes have a vertical error of less than or equal to 1.0 km. Seventy-one percent of the earthquakes have between 10 and 30 observations, but the events in our dataset have as great as 255 or as few as 4 observations. We assume an earthquake can still be well located with fewer than 10 observations, if the earthquake occurred close to a seismic station.

In addition to hypocenter and magnitude information, we have focal mechanisms for 74,774 earthquakes in our dataset. This allows us to factor in the effect of dip on the depth distribution of moment of the earthquake. For smaller magnitude earthquakes, the dip of the fault plane has little effect on the depth distribution of moment because of the small size of the fault planes. However, for larger earthquakes (i.e., larger in that they contain a large portion of the moment release in a region), fault plane dip can have a significant effect on moment distribution by compressing more moment release into a smaller proportion of the depth column. Earthquakes without focal mechanism information are assumed to have vertical rupture planes.

2.4 Calculating the Depth Distribution of Seismic Moment Release

To calculate the distribution of seismic moment release with depth, we divide the depth column into bins. We center the fault plane at the earthquake hypocenter and distribute the moment into the depth bins that the fault plane overlaps. We estimate the moment release from magnitude after *Hanks and Kanamori* [1979]

$$Mo = 10^{((1.5 \times M_l) + 9.05)} \qquad \text{(EQ 2.1)}$$

where Mo is the seismic moment, and M_l the local magnitude (we use moment magnitude for $M \geq 6$). The down-dip width of the fault plane is estimated from the magnitude

$$w = \sqrt{10^{((M_l - 4.07)/0.98)}} \qquad \text{(EQ 2.2)}$$

(from *Wells and Coppersmith*, 1994) where w is width (assuming a square rupture plane), and M_l is local magnitude. If the plane overlaps more than one depth bin, the moment is divided among the depth bins according to the proportion of overlap between the fault plane and the respective depth bin. When the plane intersects the surface, we put the top of the rupture plane at the surface and distribute the moment downward from there.

Two potential errors can affect the moment release depth distribution technique described above: 1) the potential mislocation in the depth of the hypocenter (vertical error); and 2) the uncertainty in the distribution of the moment release about the hypocenter. For small magnitude earthquakes, the vertical error often exceeds the width of the rupture plane. A M_l 3.5 earthquake has an estimated rupture width of approximately 0.5 km which is equal to the vertical error for 55% of the earthquakes in our database. Uncertainty in the distribution of moment release about the hypocenter means that we do not know where the rupture progressed after initiation at the hypocenter. We have assumed in the above technique that half of the rupture occurred above and half below the hypocenter. For small earthquakes, it is reasonable to assume that the hypocenter is the center of a small patch of slip. Although it has been suggested that most large earthquakes initiate near the base of the seismogenic crust and rupture mostly up dip of the hypocenter [*Sibson*, 1982], a sufficient number of larger earthquakes have initiated at shallow depths to disallow that simple assumption. In fact, the largest error in estimating the depth distribution of moment release from large earthquakes is that the slip is variable, and it is no longer appropriate to assume a square rupture plane and constant slip on the plane. As a result, we choose to distribute the moment release evenly above and below the hypocenter

for small earthquakes (which comprise most of our dataset), and use published finite source models wherever possible for the moderate to large earthquakes in our dataset. Moderate to large earthquakes without finite source models are treated like the small earthquakes (with even depth distribution of moment release).

The errors discussed above have little effect on the depth distribution of moment within a region, except if an earthquake contains a significant proportion of the moment release of the region and occurs relatively deep within the depth column. We can evaluate the effect of the errors by considering the extremes in distributing the moment release. We combine the two errors listed above, and compare the change in the depth distribution of the region. One extreme shallows the moment distribution by subtracting the vertical error from the hypocenter depth (depth positive) and assuming the earthquake ruptures up from the hypocenter (moment is distributed above the hypocenter). This shallow extreme puts more moment higher in the crust and reduces the maximum depth of seismic rupture. The other extreme deepens the moment distribution by adding the vertical error to the hypocenter depth and assuming the plane ruptures down from the hypocenter (moment is distributed below the hypocenter). Thus, the deep extreme puts more moment deeper in the crust and increases the maximum depth of seismic rupture. Although it is highly unlikely that either extreme of moment distribution with depth actually occurs for all earthquakes within a region, the extremes allow us to place reasonable error bounds on our results.

2.5 *Finite Source Models*

We use finite source slip models for large moment earthquakes ($M > 5$), whenever available, because the hypocenter is no longer representative of the location or extent of

rupture during the earthquake. We have assembled 19 finite source models for 12 moderate to large earthquakes (Table 2.1). These models are used to establish the appropriate level of percent depth in comparison with background seismicity, as well as in our prediction of seismogenic thickness for southern California. We consider multiple models for several earthquakes during our comparison to background seismicity so that we can evaluate the effect of the choice of slip model on our results. During the seismogenic thickness prediction phase of our project, we use the slip model that we consider to be best, based upon the dataset(s) used to create the finite source model.

In Table 2.2 we list the overall rupture dimensions of the slip models. Some models consist of more than one plane. In many slip models, the rupture plane or planes overestimates the "true" rupture area of the earthquake to ensure that all of the slip can be accommodated on the plane during the inversion [*Somerville et al.*, 1999; *Mai and Beroza*, 2000]. This overestimation of the rupture area results in rows or columns on the edges of the model that have very little or even zero slip. We use the trimming criterion of *Somerville et al.* [1999] to trim rows and columns from our slip models. The criterion is simply: if the average slip per sub-fault of the row or column located on the edge of the model is less than 0.3 times the average slip of the whole fault, then the row or column is removed from the reference model. One edge row or column is removed at a time, starting with the lowest average slip first and continuing until all edge rows or columns have the requisite average slip.

The results of the trimming process are shown in Table 2.3. Thirteen of the models required trimming. The reduction in moment release of the models was 7% on average, which resulted in an average decrease in event magnitude of 0.02 units. The 16 models

used for the comparison with background seismicity (the reference models) are NPS, WN, ER, SH-W, SH-L, SM, JT-B, JT-HD, L, N-W, N-DR, N-HU, N-HV, N-S, HM-J, and HM-K. Three of the slip models were not used in the analysis because of insufficient quality (UP and BB) or because they represented an aftershock (AN). We did not use model BB because we had to estimate the depth extent of rupture plane and assumed constant slip. The main plane of the model UP was sufficiently defined, but the location and orientation of the large asperity with 30% of the total moment was ill-defined. Even though the three models have large uncertainties associated with them, we use the three models in the prediction portion of our project, because the moment release is better defined than it would be if we had to use empirical formulas. The twelve models used to represent the moment release of the earthquakes for the prediction phase are marked with an asterisk (*) in Table 2.3.

2.6 Comparison of Finite Source Models to Pre-mainshock Regional Seismicity

If regional seismicity is a predictor of maximum rupture depth during moderate to large earthquakes, then we can use published finite source models to quantitatively define the appropriate value of percent depth for southern California, and estimate the range in this value due to identifiable errors in the data. We compare 16 distinct finite source models for 9 moderate to large earthquakes in southern California to the pre-mainshock seismicity of the mainshock region (Table 2.3). The mainshock region is based upon the regional extent of the first 24 hours of aftershocks.

We pose a simple test for the pre-mainshock regional seismicity: What percent of total moment release or of total number of hypocenters within the defined region are shallower or equal depth to the bottom of the finite source model in question? This is a simple

test for earthquake hypocenters because regardless of magnitude, as points in space, the hypocenters can be put in increasing depth order and simply counted. The two-dimensional nature of moment release requires us to sort the moment release of various magnitude earthquakes, and therefore various rupture areas, into depth bins. These depth bins correspond to the depth ranges of the sub-faults that make up a finite source model.

In the following sections, we examine depth distribution of both hypocenters and moment release of the regional seismicity to show that the depth distribution of regional pre-mainshock seismicity provides a reasonable estimation of the maximum depth of rupture during the moderate to large magnitude mainshock. We test which method of earthquake representation is a better predictor of the maximum depth of rupture during moderate to large earthquakes. Finally, assuming that the maximum depth extent of rupture during a moderate to large earthquake in southern California is synonymous with the seismogenic thickness of the region, we calculate the appropriate value of percent depth to use when estimating the seismogenic thickness of southern California.

2.6.1 Moment Release Distribution Test

We first consider the depth distribution of moment release as a predictor of the maximum depth of rupture during moderate to large southern California earthquakes. The percent of total moment released by the background seismicity shallower than the bottom of the finite source model rupture planes was greater than 99.7% for 14 of the 16 reference models (Figure 2.4(a)). The two exceptions are NPS and N-HU.

The North Palm Springs (model NPS) earthquake occurred on the boundary between two regions with maximum earthquake depths that differ by 5 km [*Magistrale and Sanders*, 1996]. The fault plane dips to the northeast and bottoms into the corner of

the step in earthquake hypocenters. Most of the slip model fault plane lies over the region of deeper seismicity, so the background seismicity has over 55% of moment release deeper than the bottom of the slip model. However, the slip model rupture plane bottoms in the region of shallower seismicity, so the bottom of the rupture plane is consistent with the depth of the background seismicity of the region on the northeast side of the step in seismicity. If only background seismicity to the northeast of the slip model hypocenter is considered, the percent of moment release of background seismicity shallower than the bottom of the slip model rupture plane is 99.3%, which is consistent with the other reference models. The other exception, Model N-HU, is a constant slip finite source model based only on geodetic data and the bottom of the slip model is 3.6 to 6.0 km shallower than that in the four other models of the Northridge mainshock. The bottom of the slip model is shallower even than the hypocenter of the earthquake at 18.7 km [*Hauksson et al.*, 1995]. We therefore exclude both the NPS and N-HU models from our calculation of the appropriate value of moment percent for the prediction of seismogenic thickness in southern California.

This test is not complete, however, without considering the effect of known errors and assumptions: 1) the vertical error of the hypocenter; 2) the distribution of moment release about the hypocenter; and 3) the definition of the 24 hour aftershock zone. We consider the effects of error/assumption 1 and 2 by looking at the shallow and deep extremes in distributing the moment release. The difference in percent moment shallower than the bottom of the slip model between the shallow and deep error extremes is often less than 0.1%. When the difference is greater, the extreme moment release distributions show that the background seismicity dataset includes one or a few earthquakes that con-

tain a significant proportion of the total moment release of the region, are modeled with large uncertainty (e.g., model SH-L). When these earthquakes are located deeper in the crust, the uncertainty in distributing the moment release about the hypocenter significantly changes the distribution of moment release near the bottom of the slip model. We investigated the effect of error/assumption 3 by considering both "tight" and "loose" interpretations of the aftershock zone and found little difference in the results of the test. (The aftershock zone comparison is discussed in more detail in Appendix A.)

The consistency of the estimate of the percent of background seismicity moment release shallower than the bottom of the rupture planes of moderate to large earthquakes for the southern California earthquakes tested above, as well as the very small difference between the shallow and deep distribution extremes, suggests that the distribution of moment release of regional seismicity is an accurate and stable estimator of the seismogenic thickness of the region. The accuracy of the technique can be evaluated by comparing the predicted depth extent with the rupture bottom of the slip models (Figure 2.4(b)). If the prediction were perfect, the two depths would be identical. Part of the inaccuracy arises from errors and differences in the slip models. Overall, the moment release percent depth predicts the maximum rupture depth of moderate to large earthquakes very well.

2.6.2 Hypocenter Distribution Test

We now consider the distribution of hypocenters as a predictor of the depth extent of rupture for moderate to large earthquakes. The percent of background seismicity hypocenters shallower than the bottom of the finite source model rupture planes was greater than 94% for 15 of the 16 reference models (Figure 2.5(a)). The exception, model NPS,

had a much lower percentage than the other models because the earthquake occurred along a step in the maximum depth in seismicity (as outlined previously in the discussion of the moment release test). When considering only the background seismicity to the northeast of the NPS hypocenter (the shallower side of the step), the percent of hypocenters shallower than the bottom of the slip model rupture plane is 86%, still inconsistent with the rest of the models.

Unlike the extreme limits in the moment distribution calculation, the extreme limits for the hypocenter test are only based upon the vertical error in the hypocenter. The difference in percent of hypocenters shallower than the bottom of the slip model between the shallow and deep error extremes ranges is 2% on average, one order of magnitude greater than the range for the moment distribution test. This larger range cannot be attributed solely to the smallest allowable step in percentage defined by the percentage of the total number contained in one hypocenter. Perhaps the larger range in error extremes is due to the imprecision of using the hypocenter to represent the rupture of earthquakes regardless of magnitude and rupture area.

The estimate of the percent of background seismicity hypocenters shallower than the bottom of the rupture planes tested above is not as consistent as that of moment release. Accuracy and stability suffer as a result. The predicted rupture depth extent from hypocenters is compared with the rupture bottom of the slip models in Figure 2.5(b). As in Figure 2.4(b), if the prediction were perfect, the two depths would be identical and fall on a line with slope of 1. The predictions are more varied and, in general, fall much further from the perfect prediction line than the moment release predictions. Overall, the percent depth of hypocenters provides a fair prediction of the seismogenic thickness.

2.6.3 Defining the Percent Value for Estimating the Seismogenic Thickness

We have shown that the percent of background seismicity moment release and hypocenters shallower than the bottom of the mainshock rupture plane is consistent for a number of moderate to large earthquakes in southern California over the last 20 years. This analysis has shown that background seismicity in the region of the future mainshock predicts the maximum depth extent of rupture during the mainshock. Although the distribution of hypocenters reasonably predicts the maximum depth, the percent results for moment release have less variation, have smaller error extremes, and are more accurate and precise because the rupture extent of the background seismicity is taken into account.

The 12 models used to calculate the appropriate percent value for the estimation of seismogenic thickness are ER, SH-W, SH-L, JT-B, JT-HD, L, N-W, N-DR, N-HV, N-S, HM-J, and HM-K (the circled data points in Figure 2.4(a) and Figure 2.5(a)). We have excluded the reference models NPS, WN, SM, N-HU as previously discussed. The mean percent of background seismicity shallower than the bottom of the mainshock rupture plane is 99.9% (±0.1%) for the moment release distribution and 98.3% (± 1.8%) for the hypocenter distribution. The percent for moment release is a much more stable and precise value. We now have a quantitatively estimated value to apply to the background seismicity to predict the seismogenic thickness for all of southern California.

2.7 Regional Predictions of Seismogenic Thickness for Southern California

In southern California, faulting is not restricted to a few major faults, nor are all the faults identified and well described. Therefore, estimating seismogenic thickness from a regional viewpoint is vital to improving seismic hazard assessments. To determine seismogenic thickness across the region, we divide southern California into 0.1°x 0.1° bins,

and calculate the depth distribution of moment release of all earthquakes with epicenters located within each regional bin. We use finite source models to represent the moment release for the 12 earthquakes marked by an asterisk (*) in Table 2.3. This allows the moment release to be distributed across a number of regional bins, rather than forcing all the moment release into the regional bin where the epicenter is located. For each regional bin, the seismogenic thickness is the depth above which 99.9% of the moment release occurs. We estimate the error range of this prediction by calculating the shallow and deep moment release distribution extremes.

The regional 0.1°x 0.1° bins provide the most detailed look at the variations in seismogenic thickness across southern California. The greater than 258,000 earthquakes in our dataset are located in just 1823 regional bins. Figure 2.6 shows the number of earthquakes located within each regional bin. Most of the bins with few earthquakes and thus an unreliable seismogenic thickness estimate are located on the edge of southern California, in the deserts of eastern California, the western Peninsular Ranges, the western Mojave Desert, the Coast Ranges, and the Continental Borderland. These regions tend to have few recognized faults, and/or are on the fringes of the Southern California Seismic Network (SCSN) where fewer earthquakes can be accurately identified and relocated. As a result, the estimate of seismogenic thickness in these regions produces a mostly incoherent checkerboard pattern (see Figure 2.7). Therefore, the seismogenic thickness prediction is considered unreliable in regions with few earthquakes (here taken to be less than ten earthquakes per regional bin), as well as regions beyond the seismic network (e.g., the Continental Borderland outboard of Santa Catalina Island; south of the international border in Baja California).

The regional bins containing earthquakes cover approximately 70% of the land area of southern California below N36° latitude (excluding the Continental Borderland and Baja California). The average seismogenic thickness for all regional bins is 12.5 km. Approximately 54% of the regional bins contain less than ten earthquakes per bin, limiting the reliability of the seismogenic thickness estimate for those bins. When we exclude the regional bins with less than ten earthquakes (Figure 2.8), the average seismogenic thickness increases to 15.0 km. Excluding bins with few earthquakes also increases the spatial coherence of the seismogenic thickness prediction.

The spatial coherence can also be improved by applying a gaussian filter (length = 30 km) to the regional seismogenic thickness estimate (Figure 2.9). The areas with the greatest seismogenic thickness predictions (> 20 km) are the Ventura Basin, the San Jacinto – San Gorgonio Pass region, the west San Joaquin Valley, northern Baja California, and portions of the Eastern California Shear Zone, the Santa Monica Mountains/San Fernando Valley, the San Jacinto fault system and the Elsinore fault system. Regions with the smallest seismogenic thickness predictions are the Salton Trough, the Coso region, portions of the Continental Borderland, and the Coast Ranges. Applying a gaussian filter to regional bins with at least ten earthquakes (Figure 2.10), results in a similar distribution of areas with greater and lesser seismogenic thickness, although some regions previously noted now lack seismogenic thickness estimates (e.g., much of the west San Joaquin Valley, portions of Baja California, the Continental Borderland, and the Coast Ranges).

The error in the seismogenic thickness predictions is quantified by calculating the shallow and deep moment release depth distributions and finding the percent depth of the new distributions. Figure 2.11 shows the difference between the percent depths calculated

for the deep and shallow moment release distribution extremes for all regional bins with data. On average, the difference in seismogenic thickness predictions is 2.3 km, or +1.2/-1.1 km. The average difference between extreme predictions decreases as the number of earthquakes per regional bin increases. Bins on the edge of southern California tend to have a much larger error range than those in the center. Individual bins may have larger or smaller error ranges depending on the distribution of earthquakes with depth within the regional bin. A large difference between moment release distribution extremes is usually due to larger earthquakes ($M > 5$) without finite source slip models, or earthquakes with large vertical errors near the base of the moment release distribution.

2.7.1 Moment Release vs. Hypocenter Prediction

Using the depth distribution of hypocenters to predict the seismogenic thickness of the crust in a regional sense yields a very similar picture to the moment release prediction. The average seismogenic thickness for all bins is 12.8 km. If you exclude regional bins with fewer than ten earthquakes, the average increases to 14.9 km. These averages are nearly indistinguishable from those of the moment release estimate. The average error range in the hypocenter prediction of 1.9 km is slightly smaller than that of the moment release prediction, but not greatly so. A smaller average error is expected for the hypocenter estimate because the errors are based solely on the vertical error in the hypocenter, while the error in the moment release includes the vertical error in the hypocenter and the distribution of moment release about the hypocenter.

Although the hypocenter and moment release seismogenic thickness predictions seem nearly identical on average, in detail the difference can be quite large for select regional bins. The difference between the moment release prediction and hypocenter pre-

diction ranges from –14.6 km to +9.3 km, but 78% of the regional bins have absolute differences of less than 1 km. A negative difference (where the hypocenter prediction exceeds the moment release prediction) usually is the result of rounding in the hypocenter prediction calculation such that the deepest earthquake in the regional bin is chosen for the percent depth. In other words, the percentage of the earthquakes in the regional bin that is closest to the wanted percent of 98.3% is 100%. This suggests that at least 30 earthquakes are needed within a regional bin in order to make the hypocenter seismogenic thickness prediction reasonable and reliable. When a regional bin contains 30 earthquakes, each hypocenter accounts for 3.3% of the total. This means that 29 hypocenters account for 96.7% of the total, which is closer to 98.3% than 100% is. It is important to determine the depth down to which most of the hypocenters occur (the definition of percent depth), rather than the depth that includes all of them. A positive difference (where the moment release prediction exceeds the hypocenter prediction) occurs when one or a few earthquakes dominate the moment release depth distribution of the regional bin. This can occur when a large portion of the moment release is contained in the sub-faults of a large earthquake, controlling the percent depth. Unlike the moment release distribution, the hypocenter of the large earthquake counts the same as a small magnitude earthquake for the hypocenter calculation, and thus, the hypocenter percent depth can be shallower than the moment release percent depth. A positive difference can also occur when an earthquake near or at the bottom of the depth profile contains a significant proportion of the moment release, setting the moment release percent depth deeper than would be assumed by simply counting all hypocenters equally. These situations show how important it is to exam-

ine the moment release depth distribution of earthquakes, rather than treating all hypocenters the same, regardless of earthquake magnitude.

2.8 *Predictions of Seismogenic Thickness for the Major Strike-Slip Fault Systems*

The three major strike-slip fault systems in southern California contribute a significant proportion of the seismic hazard to the region. Better estimates of the down-dip width of the fault segments should improve the estimation of fault area that could rupture during a large earthquake. We have quantitatively estimated the down-dip width of the segments of the San Andreas fault system (Cholame southward), the San Jacinto fault system, and the Whittier-Elsinore fault system. We use the simplified fault segment definitions of the CDMG/USGS database [*Petersen et al.*, 1996]. Fault segments are divided into sub-segments based upon the straight line segments in the CDMG map definition. The sub segments are named for the whole fault segment and numbered from north to south (Table 2.4).

The moment release of seismicity within 5 km of the fault is used to calculate the percent depth. This limits the estimate to earthquakes close to the fault, but provides enough earthquakes for a reliable seismogenic thickness estimate in most cases. It reduces the overlap in seismicity for sub-parallel fault segments (e.g., SJF-Anza-2 [18] and SJF-Coyote Creek [19]), and excludes some fault-parallel seismicity that is not clearly linked to the fault systems in question (e.g., SAF-Coachella-1 [11] and seismicity from the 1992 Joshua Tree sequence).

We estimate the seismogenic thickness from the seismicity along each whole CDMG/USGS sub-segment, and for 5 km along-strike bins. If the last along-strike bin of a sub-segment is less than 2.5 km, the seismicity is combined with the next to last segment

for the seismogenic thickness estimation. In most cases, the 5 km along-strike bins provide a sufficient seismicity for a reliable prediction. We smooth the seismogenic thickness prediction with a five point average, including along-strike bins from succeeding sub-segments when the sub-segments are connected (e.g., the San Andreas sub-segments).

We use the difference between the shallow and deep extreme distribution of moment release to provide error bars on the seismogenic thickness. On average, the range in seismogenic thickness prediction is 1.7 km, or +0.8/-0.9 km. This error is an improvement on the CDMG/USGS error estimate of ± 2 km. The average error in seismogenic thickness is similar for all three strike-slip systems

2.8.1 San Andreas Fault System

The rate and depth distribution of the background seismicity within 5 km of the San Andreas Fault, from the Cholame segment south to the Coachella Valley, varies significantly along the strike of the fault (Figure 2.12). Most of the moment release and the deepest seismicity occur at the two ends of the "big bend," a 160 km wide left-step in the fault. The Banning-San Gorgonio Pass region (sub-segments 9-11) lies at the southern end of the "big bend." Seismicity extends to 23 km depth and contains 91% of the moment release (excluding the 1986 *M*6.1 North Palm Springs earthquake) of the San Andreas projected seismicity, but only 21% of the fault length. The northern end of the left-step in the Carrizo plain (sub-segments 4-5) increases in rate and maximum depth extent of seismicity compared to the surrounding fault segments, but contains significantly less moment release and a shallower maximum depth of seismicity than the southern end.

Seismogenic thickness estimates can differ by as much as 7 km within a CDMG/USGS fault segment. This is especially true along the San Bernardino segment [9-10]

where the thickness estimate increases from 15 km to 22 km and then decreases back to 15 km, all over a length of 106 km. Such a large variation along strike is somewhat unusual for a high seismicity rate fault segment. Most of the segments or sub-segments with large variations in seismogenic thickness along strike have sections with sparse seismicity, which reduces the reliability of the estimate.

Seismogenic thickness predictions for whole sub-segments over-estimate the maximum rupture depth for most of the sub-segment. The whole sub-segment seismogenic thickness estimate is usually identical to or less than 1 km shallower than the deepest non-smoothed estimate from the 5 km along-strike bins. Because smoothing inevitably reduces the maximum through averaging, the whole sub-segment seismogenic thickness is 1.5 km thicker on average than the largest smoothed 5 km along-strike bin estimate, although the difference ranges from –2.0 km to 4.6 km. Comparing the average smoothed seismogenic thickness and the whole sub-segment seismogenic thickness, the average difference increases to 3.5 km. However, in most cases, the average seismogenic thickness of the smoothed 5 km along-strike bins would be a more appropriate whole sub-segment result, as it reduces the effect of a small region on the whole sub-segment. Additionally, the along-strike variation in seismogenic thickness of a sub-segment is approximated by the standard deviation of the mean. Ultimately, the best solution is to actually account for the along-strike variation in seismogenic thickness, rather than reducing the variation to one or two numbers for a whole fault segment.

2.8.2 San Jacinto Fault System

The San Jacinto fault system is more complex than the San Andreas fault system, with overlapping sub-parallel and parallel segments, and steps between the southern seg-

ments (Figure 2.13). The entire system has a high seismicity rate, but only one segment, Superstition Hills, has ruptured in a significant earthquake in the last 20 years. Two areas of significant, off-the-main-trace, fault-parallel seismicity (Hot Springs and Buck Ridge faults) are not included in the CDMG/USGS fault database. Some seismicity perhaps better attributed to these faults, lies within the 5 km limit of the CDMG/USGS trace, but most is excluded. The CDMG/USGS defined fault segments are not always well aligned with either the mapped surface trace or seismicity alignments. This is especially true for the San Bernardino segment [13-14], where both the mapped fault and the seismicity follow a curved path to the northeast. As a result, the "San Jacinto fault seismicity" has strike-perpendicular distances of 3-7 km from the defined straight line segment. A comparison of seismogenic thickness for seismicity ±5 km versus 0-10 km (the northeast side) from the defined segment yields nearly identical results, so we continue to use ±5 km for this segment.

Figure 2.13 shows the projected seismicity and seismogenic thickness estimates for the San Jacinto fault system. The maximum depth of seismicity shallows relatively smoothly from 19 km at the northern end of the Anza segment [17] south to 10-11 km at the parallel Superstition Mountain [21] and Superstition Hills [22] segments. The northernmost 10 km of the Imperial fault [23] continues the trend, but further south, the maximum hypocenter depth deepens. The shallowing trend correlates with an increase of heat flow to the south as the fault approaches the Salton Trough [*Doser and Kanamori*, 1986; *Sanders*, 1987].

The seismogenic thickness of the San Jacinto fault system varies significantly along strike (Figure 2.13). The largest variation occurs along the Imperial fault [23],

where the large seismogenic thickness at the southernmost end is controlled by a M2.56 earthquake at 23.3 km depth which contains 0.9% of the moment release of the along strike bin. Although we present results for locations south of the international border, the seismogenic predictions should be used extremely cautiously because the hypocenter data is considered unreliable. The second largest variation occurs along the Coyote Creek segment [19] where the seismogenic thickness decreases 6 km over 41 km segment length, resulting in an approximate dip of 8° in the seismogenic thickness. Sub-segments to the north and south of Coyote Creek [19] have dips in the seismogenic thickness of 2-3°. The sub-parallel Anza-2 [18] sub-segment shows a similar increase in dip relative to the surrounding segments, although the dip of 5° is smaller than that for the Coyote Creek [19] segment. A 4 km step in the maximum depth of hypocenters results in moderate variation in seismogenic thickness along the San Bernardino-1 [13] sub-segment. This step in hypocenters along the northern San Jacinto fault was noted by *Sanders and Magistrale* [1996] and linked to a change in basement lithology *Magistrale and Zhou* [1996]. The smoothing process has smeared the step in seismogenic thickness, but it is easily located between the fourth and fifth along strike bins in the raw seismogenic thickness estimate.

The differences between the whole segment/sub-segment seismogenic thickness estimates and the average for a segment or sub-segment tend to be small. Half of the system segments are too short to support along strike bins or have only small variations along strike so their averages are comparable to the whole segment estimates. The whole sub-segment percent depth still fails to account for significant changes in seismogenic thickness along strike.

2.8.3 Elsinore Fault System

The Elsinore fault system is the third major component of the Pacific-North American plate boundary south of the Transverse Ranges in southern California. The Elsinore fault system and other less active faults to the west carry 10-15% of the plate boundary slip in southern California [*WGCEP*, 1995]. The Elsinore system has some sub-parallel fault segments, and splits at the northern end into the Whittier fault [24], and the Chino-Central Avenue fault [31] in the Chino-Puente Hills. Near-fault seismicity occurs predominantly to the northeast side of the fault system, except for the Whittier segment [24] at the north end.

Seismogenic thickness varies from 10-21 km for the entire fault system (Figure 2.14). The deepest well constrained seismicity occurs along the northern half of the Julian segment [27]. Seismogenic thickness decreases rapidly along the southern half of the Julian segment [27], as the percent depth shallows 7 km over a length of 35 km. This decrease suggests an apparent dip in the bottom of the seismogenic layer of 11° along this section of the Elsinore fault. Percent depth levels rapidly along the Julian-Coyote Mountain segment boundary [27/28] to a dip of less than 2°. The thinning of the seismogenic crust continues along the northern 20 km of the Laguna Salada segment [29-30]. This decrease in seismogenic thickness corresponds with a relative increase in heat flow to the southeast. Seismicity along the rest of the Laguna Salada segment [29-30] is extremely sparse, and the few hypocenters are considered poorly constrained because of their location a substantial distance south of the international border. As a result, the percent depths are erratic and the seismogenic thickness predictions for the Laguna Salada-2 sub-segment [30] are poorly constrained.

The whole sub-segment percent depth prediction tends to overestimate the seismogenic thickness of the system sub-segments, as compared to the average thickness of the smoothed along strike bins. The overestimation is less than 1.3 km for half of the sub-segments. These sub-segments tend to have less variation in the percent depth values of the along strike bins, so the average of the small length estimation is comparable to the estimation for the entire length of the sub-segment. The highly questionable Laguna Salada-2 sub-segment [30] has the largest difference between whole sub-segment seismogenic thickness and the average of the along strike bins seismogenic thickness (12 km). Otherwise, the largest difference is only 3.2 km for the Whittier segment [24]. Regardless, the whole sub-segment seismogenic prediction fails to reflect the significant along strike variations among the northern Elsinore fault system segments.

2.8.4 Moment Release vs. Hypocenters

On average, there is no difference between the moment release and hypocenter along strike seismogenic thickness predictions. In detail however, the difference can be significant. When there are few earthquakes within a bin, the hypocenter prediction overestimates the seismogenic thickness because a whole number of hypocenters are required to calculate the percent depth. A low seismicity rate within a bin also affects the reliability of the moment release prediction, but fewer earthquakes are needed than the hypocenter calculation to make the seismogenic thickness estimate reasonable (~10+ vs. ~30+). Large differences can also occur when a bin contains the sub-faults of a large earthquake, or an earthquake at or near the bottom of the depth profile with a significant proportion of the moment release within the bin. The difference occurs because unlike the hypocenter prediction, the moment release prediction takes into account of the size of the earthquake.

Estimating seismogenic thickness from the moment release of earthquakes looks at the rupture extent of earthquakes in the crust, while using hypocenters only looks at the locations in the crust where earthquakes start. Therefore, seismogenic thickness is most appropriately predicted by the moment release estimation.

2.9 Discussion

2.9.1 Factors Affecting Seismogenic Thickness

The thickness of the seismogenic crust varies across southern California on scales from a few kilometers to tens of kilometers. The factors that affect the depth of the transition zone from seismic to aseismic deformation include the geothermal gradient or temperature structure of the crust, crustal composition, fluid pressure, strain rate, water content, and the geometry and mode of faulting [*Sibson*, 1984]. The most significant of these factors are believed to be temperature and, secondarily, composition [*Sibson*, 1984; *Doser and Kanamori*, 1986; *Bryant and Jones*, 1992; *Williams*, 1996]. Seismogenic thickness variations caused by the temperature structure of the crust are likely to occur over length scales similar to the thickness of the crust, while abrupt changes in seismogenic thickness may correspond to abrupt changes in crustal composition [*Sibson*, 1984]. We extend previous studies that have related the variation in the depth of earthquake hypocenters in limited regions of southern California to the temperature structure of the crust, basement lithology, shear stress, and strain rate.

2.9.2 Temperature

The effect of temperature on the seismogenic crust is perhaps the easiest factor to consider, because of the larger distance scale associated with the effect. In this study, we use surface heat flow as a proxy for relative changes in the crustal geotherm. We assume

the crustal geotherm is elevated (e.g., greater relative temperatures at shallower depths than normal) when heat flow is higher than normal, and a depressed crustal geotherm (e.g., cooler relative temperatures at deeper depths than normal) when the heat flow is lower than normal. We compare our estimates of seismogenic thickness with published data on heat flow to evaluate the effects of temperature on the thickness of the seismogenic crust in southern California.

Two regions in Figure 2.8 have a significantly lower seismogenic thickness and correspond to regions of higher heat flow: the Salton trough, and the Coso region. The higher heat flow of the Salton trough [*Lachenbruch et al.*, 1985] also affects the seismogenic thickness of the San Jacinto and Elsinore fault systems, which shallow systematically to the south and correlate with heat flow along strike [*Doser and Kanamori*, 1986; *Sanders*, 1987]. The Coso region has high heat flow as also demonstrated by the presence of young cinder cones [*Jennings*, 1994]. Figure 2.8 also shows the seismogenic thickness of the southern Eastern California Shear Zone (ECSZ) decreasing to the east, and somewhat less to the north. There is a significant difference in maximum hypocenter depths between the 1992 Landers earthquakes and the 1999 Hector Mines earthquake sequence further east. Heat flow increases dramatically to the east, with the highest values forming a ridge to the east of the northwest striking faults of the ECSZ [*Lachenbruch et al.*, 1985]. *Williams* [1996] showed that aftershock activity along strike of the 1992 Landers rupture shallows to the north, and corresponds to the depth variation in the 250° C isotherm.

The effect of temperature is also present in regions of lower than normal heat flow as a thickening of the seismogenic portion of the crust (Figure 2.8). The best example of this is the Ventura Basin, a narrow region of very low heat flow [*De Rito et al.*, 1989]. The

anomalously large seismogenic thickness is likely caused by rapid shortening across the basin which led to a thick sedimentary section and a deep Moho [*Bryant and Jones*, 1992]. Other than the Ventura basin, the deepest earthquake hypocenters south of the Garlock fault are located beneath the San Gorgonio Pass-San Jacinto Mountains region. The San Jacinto Mountains lie at the northern reaches of the Peninsular Ranges, a province known to have low heat flow [*Lachenbrach et al.*, 1985]. A north-south alignment of increased seismogenic thickness in the Peninsular Ranges extending from the San Jacinto Mountains south to the Elsinore fault system (and perhaps a far south as northwest Baja California) coincides with the low heat flow core region bounded on the east and west by the elevated heat flow of the Salton Trough and the Inner Borderland. The greatest seismogenic thickness of the north south alignment coincides with an area of very low heat flow. On the north of the San Gorgonio Pass, the seismogenic thickness beneath the San Bernardino Mountains is a few kilometers greater than the overall average for southern California, possibly reflecting the low to normal heat flow of this mountain range. However, the abrupt increase in seismogenic thickness of the crust to the south of the San Bernardino Mountains cannot be explained by temperature, because the San Jacinto-Santa Rosa Mountains also have low to normal heat flow [*Lee*, 1983]. Similarly, the west San Joaquin Valley has deep seismicity and moderately low heat flow, but low heat flow alone cannot reasonably account for the significant seismicity that occurs down to 25 km depth.

Heat flow alone cannot explain the distribution of seismogenic thickness variations in southern California. The effect of temperature seems to account well on a qualitative level for most of the regions with relative thin or thick seismogenic crust, but often fails to explain the differences in detail. These failures in detail vary from an incomplete

explanation for the extreme thickness of the seismogenic crust beneath the western edge of the San Joaquin Valley, a region of moderately low heat flow, but not very low heat flow, to the inability to explain the abrupt increase in seismogenic thickness in the San Gorgonio Pass region. Additionally, it is difficult to use heat flow in a predictive fashion for seismogenic thickness because it is unclear what temperature isotherm appropriately maps out the aseismic-seismic transition for more than a limited area.

2.9.3 Shear Stress and Strain Rate

One way to assess the effect of shear stress or strain rate on brittle deformation in the crust is to compare the major fault zones to the surrounding crustal blocks. It is reasonable to assume that stress and strain may be different between these two types of regions, and therefore may result in different depth distributions of earthquakes and moment release. *Sanders* [1990] considered the depth distribution of 1665 good quality hypocenters located south and east of the Cajon Pass, and noted that the major strike slip fault zones (San Jacinto and San Andreas fault systems) have predominantly deep earthquakes, while the surrounding crustal blocks have predominantly shallow earthquakes. The maximum depth of seismicity for the seismicity in the fault zones was 5 km greater than that in the surrounding crustal blocks (the central and western Peninsular Ranges, the San Bernardino Mountains, and the southern part of the ECSZ).

If strain is locally high because it is concentrated in a narrow region along the fault zone, then the depth of the aseismic-seismic transition will deepen and increase the thickness of the seismogenic crust along the fault zone relative to the surrounding crustal blocks [*Sanders*, 1990]. The depth distribution of the hypocenters was also markedly different between the fault zones and the crustal blocks. Seismicity along the fault systems

was concentrated at the bottom of the fault (characteristic depths 11-18 km), while most of the hypocenters in the crustal blocks were located at shallow depths (characteristic depths 1-6 km). Approximately 85% of the earthquakes shallower than 10 km were located in crustal blocks, while 84% of the earthquakes deeper than 10 km were located in fault zones. Lower levels of shear stress in the crustal blocks would limit brittle failure within these regions to shallower depths, and thus seismicity would be predominantly shallower than that of the fault zones [*Sanders*, 1990; *Miller and Furlong*, 1988].

We have expanded on this analysis by considering all of southern California, and using the SCEC source zones [*WGCEP*, 1995] to define fault zones (Type A and B zones) and crustal blocks (Type C zones). These seismotectonic zones were designed to highlight the major faults as well as account for regions of diverse or hidden faults. We have considered both the distribution of hypocenters and the distribution of moment release within the SCEC source zones. Our analysis shows that there are only minor differences between fault zones and crustal blocks. There is more variation within the fault zone or crustal block categories than between the categories. Assuming that seismogenic thickness is equivalent to the "maximum depth" of Sanders [1990], we find that both crustal blocks and fault zones have on average maximum depths of 16 km from hypocenters, and 17 km from moment release. Crustal blocks and fault zones also have similar characteristic depths. Fault zones tend to have earthquakes from the surface to 17 km, although portions of some faults may have shallow and/or deep concentrations of earthquakes. Earthquakes in crustal blocks tend to occur between the surface and 13 km. The depth of peak earthquake occurrence on average in crustal blocks is a few kilometers shallower than in fault zones, because the crustal blocks tend to have a less peaked earthquake distribution with

depth than many of the fault zones. More earthquakes shallower than 10 km occur in the crustal blocks (59%) than the fault zones (41%), but this is not surprising because the crustal blocks cover approximately 61% of the surface area of the region versus 39% for the fault zones. The crustal blocks dominate the moment release of the regions in question, containing 90% of the moment release occurring shallower than 10 km, and 70% occurring deeper than 10 km. Most of the moment release can be attributed to the 1992 Landers earthquake and the 1999 Hector Mines earthquake, which account for 52% and 40% respectively, of the moment release contained in the crustal blocks.

Our analysis using an expanded region and much larger dataset shows that the conclusions of *Sanders* [1990] do not apply to all of southern California. The fault zones were limited to the San Jacinto and portions of the San Andreas fault systems. Both of these faults have significant variations in the distribution of earthquakes along the strike of the fault. Most of the earthquakes along the San Andreas fault in Sanders dataset occur in the San Gorgonio Pass region, which likely does not have a thru-going strike-slip segment, and has significant seismicity occurring at least 6 km deeper than the segments on either side. The Elsinore fault system has significant shallow seismicity along most of its length, but was included with the western and central Peninsular Ranges in the southwest crustal block of *Sanders* [1990]. This contributed to the perception that shallow seismicity did not occur characteristically along major fault zones. Local variations in stress and strain rate may likely account for variations in seismogenic thickness along faults or between different regions, but on average, does not cause a difference in seismogenic thickness and characteristic depth distribution of earthquakes between fault zones and crustal blocks.

2.9.4 Lithology

The effect of lithology on the seismogenic thickness is difficult to consider within the scope of this report because of the broad coverage area of this study. Compositional variations in the basement rocks could lead to abrupt and/or small scale variations in the thickness of the seismogenic crust that may not be visible in the regional analysis because of the size or alignment of the regional bins. Magistrale and Zhou [1996] found steps (width scale < 5 km) and slopes (width scale ~ tens of km) in the maximum depth of hypocenters that correlate with boundaries of proposed regions of schist basement rock. Unless the boundaries of the regional bins fortuitously aligned with the step in hypocenters, our analysis would obscure the step or cause an apparent shift in the location. The San Gorgonio Pass region shows the only obvious continuous step in seismogenic thickness in our regional analysis, but the location appears to be shifted to the north by approximately one-half bin size relative to the step of *Magistrale and Zhou* [1996; Figure 2a]. Other steps mentioned by *Magistrale and Zhou* [1996] can be identified once the location is already known, but are not clear enough on the regional seismogenic thickness map to locate without additional information. Slopes in seismogenic thickness are easier to identify because they occur over the scale of a few regional bins. The slopes across the Tehachapi Mountains and the southern Sierra Nevada can be identified in Figure 2.8.

Variations in seismogenic thickness due to compositional variations (if they exist) should be more obvious in the along strike analysis of the major strike slip systems of southern California. The step in the San Gorgonio Pass region noted by *Magistrale and Zhou* [1996] is more than 5 km north of the CDMG/USGS San Andreas fault segments in virtually all of the 5 km along strike bins, so the step is not seen in the projected seismic-

ity. For all three strike-slip systems, we compared the seismicity of the 5 km along-strike bins from one side of the fault segments to the other (+/-), and found no obvious consistent difference in seismogenic thickness or maximum depth of hypocenters. The only step we can identify in the along-strike projections occurs parallel to strike along the San Bernardino segment of the San Jacinto fault. This 4 km step in the maximum depth of hypocenters has been identified by *Magistrale and Zhou* [1996], and linked to the same change in basement lithology as the San Gorgonio fault. The step appears along strike of the San Jacinto fault, rather than from one side to the other as expected for a major strike-slip fault because the fault offsets the change in basement lithology [*Magistrale and Zhou*, 1996].

The study of the effect of compositional changes in the basement lithology of southern California on the seismogenic thickness of the crust requires detailed studies and abundant earthquakes. Sharp steps and small scale variations require abundant data to precisely identify the location and the size of the variation in seismogenic thickness. Although compositional variations in the basement have a significant effect on the seismogenic thickness of the crust, this study is not really designed to identify lithological control, because of the broad and large scale of the analysis relative to the small scale of the compositional changes. The along-strike analysis of the San Andreas, San Jacinto, and Elsinore fault systems is of appropriate scale for comparison to compositional changes in basement lithology. Because the San Jacinto and Elsinore fault systems are located within the Peninsular Ranges province, large compositional changes in basement lithology are not expected. The San Andreas fault system does show evidence for compositional changes across the strike-slip system, but does not appear in our along-strike analysis because of the alignment of the fault segments in the San Gorgonio Pass region. Other

segments of the San Andreas fault system have insufficient seismicity to test for seismogenic thickness changes that might correlate with changes in basement lithology.

2.9.5 The Seismogenic Thickness of Tectonically Defined Regions

In this study, we estimated the seismogenic thickness in a regional sense by dividing southern California into 0.1°x0.1° bins. This provided a detailed view of seismogenic thickness at a resolution deemed the finest appropriate for the earthquake population of most parts of southern California. Although a detailed view tells you the most about the value in question, it involves an immense amount of data. Additionally, a detailed view of the seismogenic thickness has not been previously available for southern California. The solution to either the lack of data or an overwhelming amount of data is to divide southern California into larger regions, based upon geological data such as the trace of major faults, basement lithology, and deformation style. It is not clear whether features at depth, such as crustal thickness or seismogenic thickness, correspond to the boundaries seen in the surface and near-surface data.

The 65 source zones of the SCEC Phase II report [*WGCEP*, 1995] provide an excellent opportunity to test whether dividing southern California into polygons based upon geological information is a reasonable alternative to the detailed regional bins. Of these zones (Type A and B) 41 are narrow polygons (usually ~15-20 km wide) centered on the major faults. The remaining 24 zones (Type C) cover the rest of southern California in-between and adjacent to the zones containing faults.

We compared the seismogenic thickness estimate calculated from all seismicity located within each source zone, to the average of the seismogenic thickness predictions of the regional bins located inside each source zone. A regional bin is considered to be

inside, if the center of the regional bin is located inside the source zone polygon. The average seismogenic thickness is based upon regional bins with ten or more earthquakes.

For most of the SCEC source zones, the seismogenic thickness is not appropriately described by a single value such as the mean seismogenic thickness. Seismogenic thickness often varies significantly within a source zone. The variation of seismogenic thickness within a source zone (as measured by both the standard deviation of the mean, and the difference between the minimum and maximum values) is proportional to the area of the polygon. This is not too surprising, because the larger the region, the more chance you have to encounter differences in the physical parameters that control the seismogenic thickness.

Another consideration is how the polygon is drawn. One bin or a small region can dominate the whole polygon seismogenic thickness estimate or skew the average. This is a special concern for polygons with limited earthquakes. The normal tendency is to cover a region with sparse earthquakes with a large polygon because you have no basis to make detailed estimates for most of the area. The seismogenic thickness estimate for a small corner or area of the polygon will be extended for the large area of the polygon. If the polygon boundary is not correct, or the small area with earthquake has an anomalous seismogenic thickness, then you will be extending the incorrect or anomalous seismogenic thickness inappropriately across the entire region defined by the polygon.

2.9.6 Improvements to the CDMG/USGS Fault Database

Seismic hazard assessments use seismic moment release to measure the seismic potential of a fault or region. A model of the sources of seismic hazard is created that describes the magnitude, location and rate of earthquakes that pose a significant hazard to

the region in question. The seismic hazard source model is then used to calculate the probability of damaging earthquakes and/or to calculate the probability of damaging ground motions. The detail and accuracy of the seismic hazard source model is crucial to the usefulness and applicability of the seismic hazard assessment. The CDMG/USGS fault database for California [*Peterson et al.*, 1996] improved upon the fault database of the SCEC Phase II report [*WGCEP*, 1995] by adding the down-dip width, rupture top, and rupture bottom of the fault segments. This study improves upon the CDMG/USGS database by quantitatively estimating the seismogenic thickness (equivalent to the down-dip width for vertical faults that break the surface) systematically and in detail for the San Andreas, San Jacinto, and Elsinore fault systems.

Table 2.4 lists our estimates of the seismogenic thickness, *H*, as well as the CDMG/USGS rupture bottom, *RB* (equivalent to our seismogenic thickness for these segments because the rupture top is at the surface). We list the whole sub-segment (WSS) estimate, as well as the sub-segment smoothed 5 km along-strike bins mean, minimum, and maximum, to show the variation of the seismogenic thickness within the sub-segment. The whole sub-segment seismogenic thickness tends toward the maximum of the segment, so it often overestimates the seismogenic thickness for much of the sub-segment when there is large variation along strike. The maximum seismogenic thickness of the smoothed 5 km along-strike bins is usually less than the whole sub-segment estimate because the smoothing process reduces the maximum value by averaging with the surrounding, lesser values.

The whole sub-segment seismogenic thickness is equivalent to or exceeds the CDMG/USGS rupture bottom for the San Andreas and San Jacinto fault systems. The dif-

ference can exceed 7 km at the ends of the "big bend" of the San Andreas fault. Of course, the large seismogenic thickness estimate at the ends of the "big bend" is not necessarily appropriate for the surrounding sub-segments, and the between our WSS estimate and the CDMG/USGS value is much smaller (~0-4 km). In general, the WSS seismogenic thickness estimate and the CDMG/USGS rupture bottom are close for the Elsinore fault system. Except for the Julian segment and the unreliable Laguna Salada segment, the difference is ± 2 km, which is the stated error in the depths for the CDMG/USGS values.

The mean of the smoothed 5 km along-strike bins seismogenic thickness is within 3 km of the CDMG/USGS estimate. Often, the difference is 2 km or less which is within the stated error for the CDMG/USGS database. If the average thickness of the segment was the same as the database, then the rupture plane would have the same area, and for constant slip along strike during rupture, then total moment release would be the same. Far enough away from the fault segment, the difference in fault plane definition (5 km along strike variable depth rectangles versus a single rectangle with identical area) would not matter. Locally, the difference in segment definition could result in significant differences in ground motion, especially if slip is variable along strike of the segment.

The largest error in the CDMG/USGS database is not that the whole segment rupture bottom estimates are wrong (which they are at times), but that the database does not describe the significant variation in seismogenic thickness within a segment or even a sub-segment. In most cases, using one value (e.g., an average or a maximum) for the seismogenic thickness of a segment or sub-segment is inappropriate. Fault segmentation should be smaller than has been utilized in the past, and should be redesigned taking into account the variations in seismogenic thickness along strike. A key point here is that seg-

mentation of the major strike-slip faults of southern California based upon surface features does not correspond to the variations in seismogenic thickness along strike and the potential down-dip width of the fault.

2.9.7 Seismic Hazard Implications

The characteristic magnitude or maximum magnitude of a fault or region is often based upon the area of that fault or region. Assuming a constant value for a whole fault or region leads to over- and underestimating that seismic potential of the fault or region. Either can be damaging to the reliability and usefulness of a seismic hazard analysis.

For example, the SCEC Phase II report [*WGCEP*, 1995] estimated the moment rate contribution from characteristic earthquakes using an assumed seismogenic thickness of 11 km for all of southern California. From the regional analysis, the average seismogenic thickness (from reliable regional bins) is 15.0 km. We can calculate the change in magnitude, m, by combining equations (1) and (2) from the SCEC report [*WGCEP*, 1995].

$$\Delta m = \left(\frac{2}{3}\right)\log\left(\frac{H_2}{H_1}\right) \qquad \text{(EQ 2.3)}$$

The change in magnitude due to an increase of 4 km in seismogenic thickness (from H_1 = 11 km to H_2 = 15 km) is 0.09. While this seems small, it is on the same order as the rounding of magnitudes that was cited as one of the reasons why the SCEC Phase II report overestimated the rate of magnitude 6 and 7 earthquakes, relative to the historic rate.

Seismogenic thickness is also a key component of geological and geodetic constraints on seismic source models. Both the geological (from faults) and geodetic (from strain) moment rate estimates depend linearly on the seismogenic thickness. The seismic hazard is therefore dependent on the seismogenic thickness used.

2.10 *Conclusions*

Regional pre-mainshock seismicity can predict the maximum depth of rupture for moderate to large earthquakes in southern California. We have quantitatively established that the depth down to which 99.9% of the moment release of earthquakes occurs reliably estimates the maximum depth of rupture during moderate to large earthquakes. Unlike previous studies, we use the moment release depth distribution of seismicity rather than simply the hypocenter distribution, because moment release produces more precise estimates with smaller errors. Hypocenters tell you where earthquakes start, while moment release tells you where in the crust they rupture. We assume that the maximum depth of rupture during these larger events is synonymous with seismogenic thickness, and therefore we can estimate the seismogenic thickness in a systematic and widespread fashion for southern California.

We predict the seismogenic thickness for a regional viewpoint using 0.1°x0.1° bins. The average seismogenic thickness for southern California is 15.0 km (+1.2/-1.1 km). Seismogenic thickness qualitatively correlates with regions of anomalous heat flow, but heat flow cannot be used in a predictive fashion because seismogenic thickness is controlled by a combination of factors. Local variations in stress and strain rate may account for variations in seismogenic thickness along faults or between different regions, but on average, do not cause a difference in seismogenic thickness and characteristic depth distribution of earthquakes between fault zones and crustal blocks.

We predict seismogenic thickness for the three major strike-slip systems in southern California, using seismicity within 5 km of the simplified CDMG/USGS fault database. We seek to update the fault database. Seismogenic thickness can vary significantly

within a fault segment. In most cases, using one value (e.g., an average or a maximum) for the seismogenic thickness of a segment or sub-segment is inappropriate. Fault segmentation should be smaller than has been utilized in the past, and should be redesigned taking into account the variations in seismogenic thickness along strike. Surface segmentation of the major strike-slip faults of southern California does not reflect the variations in seismogenic thickness and the potential down-dip width of the fault.

Assuming a constant value for a whole fault or region leads to over- and underestimating that seismic potential of the fault or region. The change in magnitude due to an increase of 4 km in seismogenic thickness (from H_1 = 11 km to H_2 = 15 km) is 0.09. While this seems small, it is on the same order as the rounding of magnitudes that was cited as one of the reasons why the SCEC Phase II report overestimated the rate of magnitude 6 and 7 earthquakes, relative to the historic rate. Both the geological (from faults) and geodetic (from strain) moment rate estimates depend linearly on the seismogenic thickness. The seismic hazard is therefore dependent on the seismogenic thickness used.

2.11. References

Bennett, R.A., R.E. Reilinger, W. Rodi, Y. Li, M.N. Toksoz, and K. Hudnut, Coseismic slip associated with the 1992 Mw 6.1 Joshua Tree, California, earthquake: Implications for the Joshua Tree-Landers earthquake sequence, *J. Geophys. Res.*, *100*, 6443-6461, 1995.

Bryant, A.S., and L.M. Jones, Anomalously deep crustal earthquakes in the Ventura Basin, southern California, *J. Geophys. Res.*, *97*, 437-447, 1992.

Doser, D.I., and H. Kanamori, Depth of seismicity in the Imperial Valley region (1977-1983) and its relationship to heat flow, crustal structure, and the October 15, 1979, earthquake, *J. Geophys. Res.*, *91*, 675-688, 1986.

Dreger, D.S., Empirical Green's Function study of the January 17, 1994, Northridge, California, earthquake, *Geophys. Res. Lett.*, *21*, 2633-2636, 1994.

Dreger, D., The large aftershocks of the Northridge earthquake and their relationship to mainshock slip and fault zone complexity, *Bull. Seism. Soc. Am.*, *87*, 1259-1266, 1997.

Dreger, D.S., and D.V. Helmberger, Complex faulting deduced from broadband modeling of the 28, February 1990 Upland earthquake (M_L = 5.2), *Bull. Seism. Soc. Am.*, *81*, 1129-1144.

Eisner, L., A reciprocity method for multiple source simulations, Ph.D. Thesis, 90 pp., California Institute of Technology, Pasadena, 2001.

Field, E.H., D.D. Jackson, and J.F. Dolan, A mutually consistent seismic-hazard source model for southern California, *Bull. Seism. Soc. Am.*, *89*, 559-578, 1999.

Hanks, T.C., and H. Kanamori, A moment magnitude scale, *J. Geophys. Res.*, *84*, 2348-2350, 1979.

Hartzell, S., Comparison of seismic waveform inversion results for the rupture history of a finite fault: Application to the 1986 North Palm Springs, California, earthquake, *J. Geophys. Res.*, *94*, 7515- 7534, 1989.

Hartzell, S., and M. Iida, Source complexity of the 1987 Whittier Narrows, California, earthquake from the inversion of strong ground motion records, *J. Geophys. Res.*, *95*, 12475-12485, 1990.

Hauksson, E., Crustal structure and seismicity distribution adjacent to the Pacific and North American plate boundary in southern California, *J. Geophys. Res.*, *105*, 13875-13903, 2000.

Hauksson, E., L.M. Jones, and K. Hutton, The 1994 Northridge earthquake sequence in California: Seismological and tectonic aspects, *J. Geophys. Res.*, *100*, 12335-12355, 1995.

Hill, D.P., J.P Eaton, and L.M. Jones, Seismicity, 1980-86, in The San Andreas Fault System, California, *USGS Prof. Paper 1515*, R.E. Wallace, ed., p.115-152, 1990.

Hough, S.E., and D.S. Dreger, Source parameters of the April 23, 1992, M 6.1 Joshua Tree, California, earthquake and its aftershocks: Empirical Green's Function analysis of GEOS and TERRAscope data, *Bull. Seis. Soc. Am.*, *85*, 1576-1590, 1995.

Hudnut, K.W., Z. Shen, M. Murray, S. McClusky, R. King, T. Herring, B. Hager, Y. Feng, P. Fang, A. Donnellan, and Y. Bock, Co-Seismic displacements of the 1994 Northridge, California, earthquake, *Bull. Seis. Soc. Am.*, *86*, S19-S36, 1996.

Jennings, C.W., Fault activity map of California and adjacent areas, with locations and ages of recent volcanic eruptions, 1:750,000 scale, *Geol. Data Map No. 6*, Calif. Div. Mines and Geol., Sacramento, CA, 1994.

Jennings, P., Fault map of California with volcanoes, thermal springs and thermal wells, 1:750.000 scale, *Geol. Data Map 1*, Calif. Div. Mines and Geol., Sacramento, CA, 1975.

Ji, C., D.J. Wald, and D.V. Helmberger, Source description of the 1999 Hector Mine, California earthquake; Part II: Complexity of slip history, submitted to *Bull. Seism. Soc. Am.*, 2000.

Kaverina, A., D. Dreger, and E. Price, Source process of the October 16, 1999 Hector Mine earthquake (M_w 7.2) from the inversion of broadband regional data, submitted to *J. Geophys. Res.*, 2000.

Lachenbruch, A.H., J.H. Sass, S.P. Galanis, Jr., Heat flow in southernmost California and the origin of the Salton Trough, *J. Geophys. Res.*, *90*, 6709-6736, 1985.

Larsen, S., R. Reilinger, H. Neugebauer, and W. Strange, Global Positioning System measurements of deformations associated with the 1987 Superstition Hills earthquake: Evidence for conjugate faulting, *J. Geophys. Res.*, *97*, 4885- 4902, 1992.

Lee, T., Heat flow through the San Jacinto fault zone, southern California, *Geophys. J. R. Astr. Soc.*, *72*, 721-731, 1983.

Magistrale, H., and C. Sanders, Evidence from precise earthquake hypocenters for segmentation of the San Andreas fault in San Gorgonio Pass, *J. Geophys. Res.*, *101*, 3031-3044, 1996.

Magistrale, H., and H. Zhou, Lithologic control of the depth of earthquakes in southern California, *Science*, *273*, 639-642, 1996.

Mai, P.M., and G.C. Beroza, Source scaling properties from finite-fault-rupture models, *Bull. Seis. Soc. Am.*, *90*, 604-615, 2000.

Miller, C.K., and K.P. Furlong, Thermal-mechanical controls on seismicity depth distributions in the San Andreas fault zone, *Geophys. Res. Lett.*, *15*, 1429-1432, 1988.

Peterson, M.D., W.A. Bryant, C.H. Cramer, T. Cao, M.S. Reichle, A.D. Frankel, J.J. Lienkaemper, P.A. McCrory, and D.P. Schwartz, Probablistic seismic hazard assessment for the state of California, *U.S. Geol. Surv. Open-File Report 96-0706*, 1996.

Sanders, C.O., Seismotectonics of the San Jacinto fault zone and the Anza seismic gap, Ph.D. thesis, 180 pp., California Institute of Technology, Pasadena, 1987.

Sanders, C.O., Earthquake depths and the relation to strain accumulation and stress near strike-slip faults in southern California, *J. Geophys. Res.*, *95*, 4751-4762, 1990.

Shen, Z, B.X. Ge, D.D. Jackson, D. Potter, M. Cline, and L. Sung, Northridge earthquake rupture models based on the Global Positioning System measurements, *Bull. Seis. Soc. Am.*, *86*, S37-S48, 1996.

Sibson, R.H., Fault zone models, heat flow, and the depth distribution of earthquakes in the continental crust of the United States, *Bull. Seis. Soc. Am.*, *72*, 151-163, 1982.

Sibson, R.H., Roughness at the base of the seismogenic zone: Contributing factors, *J. Geophys. Res.*, *89*, 5791-5799, 1984.

Somerville, P., K. Irikura, R. Graves, S. Sawada, D. Wald, N. Abrahamson, Y. Iwasaki, T. Kagawa, N. Smith, and A. Kowada, Characterizing crustal earthquake slip models for the prediction of strong ground motion, *Seis. Res. Lett.*, *70*, 59-80, 1999.

Wald, D.J., Strong motion and broadband teleseismic analysis of the 1991 Sierra Madre, California, earthquake, *J. Geophys. Res.*, *97*, 11033-11046, 1992.

Wald, D.J., and T.H. Heaton, Spatial and temporal distribution of slip for the 1992 Landers, California earthquake, *Bull. Seism. Soc. Am.*, *84*, 668-691, 1994.

Wald, D.J., T.H. Heaton, and K.W. Hudnut, The slip history of the 1994 Northridge California, earthquake determined from strong ground motion, teleseismic, GPS, and leveling data, *Bull. Seism. Soc. Am.*, *86*, S49-S70, 1996.

Wald, D.J., D.V. Helmberger, and S.H. Hartzell, Rupture process of the 1987 Superstition Hills earthquake from the inversion of strong-motion data, *Bull. Seis. Soc. Am.*, *80*, 1079-1098, 1990.

Wells, D.L., and K.J. Coppersmith, New Empirical Relationships among magnitude, rupture length, rupture width, rupture area, and surface displacement, *Bull. Seis. Soc. Am.*, *84*, 974-1002, 1994.

Williams, C.F. Temperature and the seismic/aseismic transition: Observations from the 1992 Landers earthquake, *Geophys. Res Lett.*, *23*, 2029-2032, 1996.

Working Group on California Earthquake Probabilities, Pobabilities of large earthquakes occurring in California on the San Andreas fault, *U.S. Geol. Surv. Open-File Report 88-398*, 62 p., 1988.

Working Group on California Earthquake Probabilities, Seismic hazards in southern California: probable earthquakes, 1994 to 2024, *Bull. Seism. Soc. Am.*, *85*, 379-439, 1995.

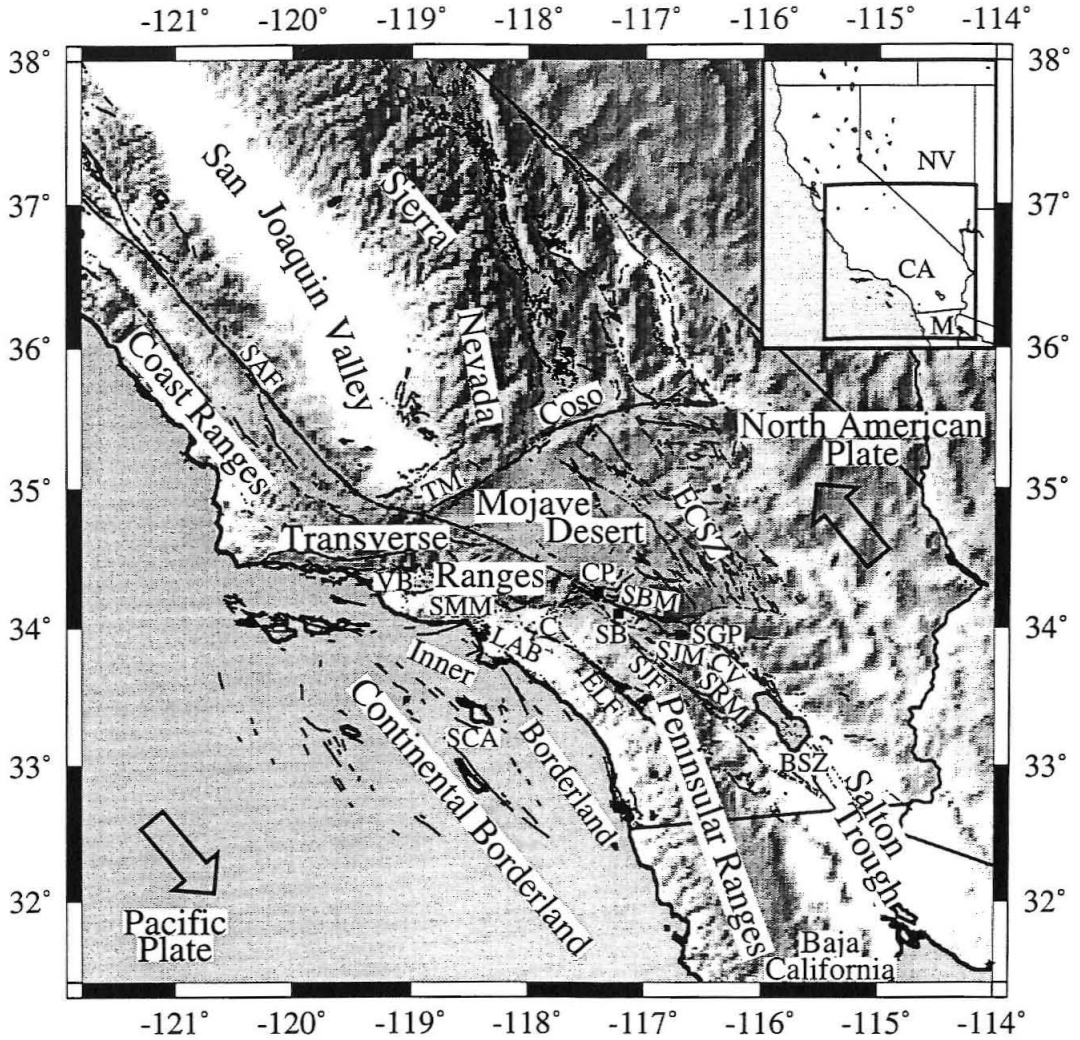

Figure 2.1 Tectonic and physiographic provinces of southern California in study area. Mapped surface traces of faults (Jennings, 1975) shown as thin black lines. The arrows show the approximate relative motion of the Pacific and North American plates. BSZ - Brawley Seismic Zone; C - Chino-Puente Hills; CA - state of California; CP - Cajon Pass; CV - Coachella Valley; ECSZ - Eastern California Shear Zone; LAB - Los Angeles Basin; NV - state of Nevada; M - Mexico; SB - San Bernadino (city); SBM - San Bernadino Mountains; SCA - Santa Catalina Island; SGP - San Gorgonio Pass; SJM - San Jacinto Mountains; SMM - Santa Monica Mountains; SRM - Santa Rosa Mountains; TM - Tehachepi Mountains; VB - Ventura Basin.

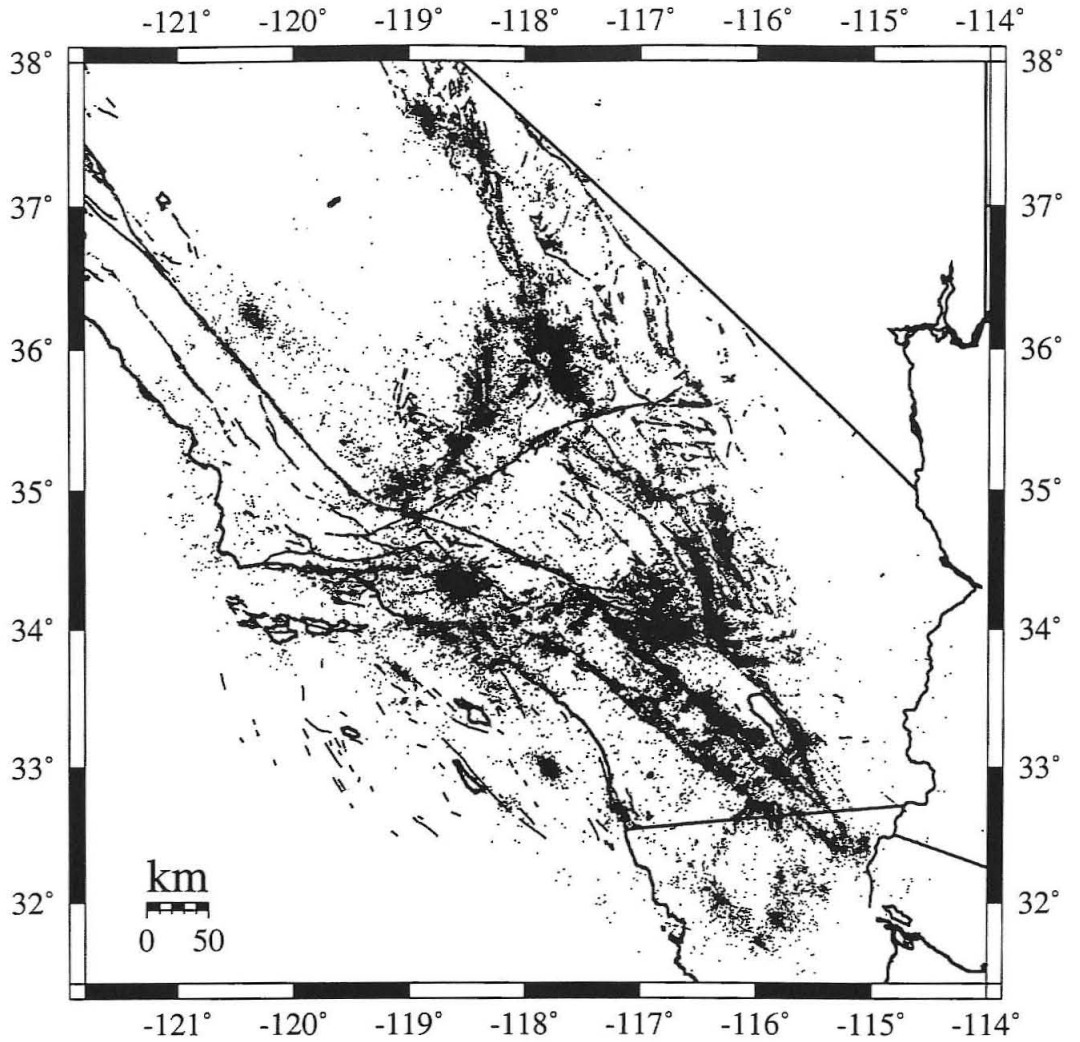

Figure 2.2 Earthquakes used in this study. Our dataset consists of ~258,000 earthquakes recorded by the Southern California Seismic Network (SCSN) between April 1981 and July 2000. These earthquakes have been relocated using the 3-D velocity model of Hauksson (2000) and range in magnitude from 0.1 to 7.3. Vertical and horizontal errors in the hypocenter do not exceed 2.0 km and 1.5 km, respectively. Mapped surface traces of faults (Jennings, 1975) shown as thin black lines.

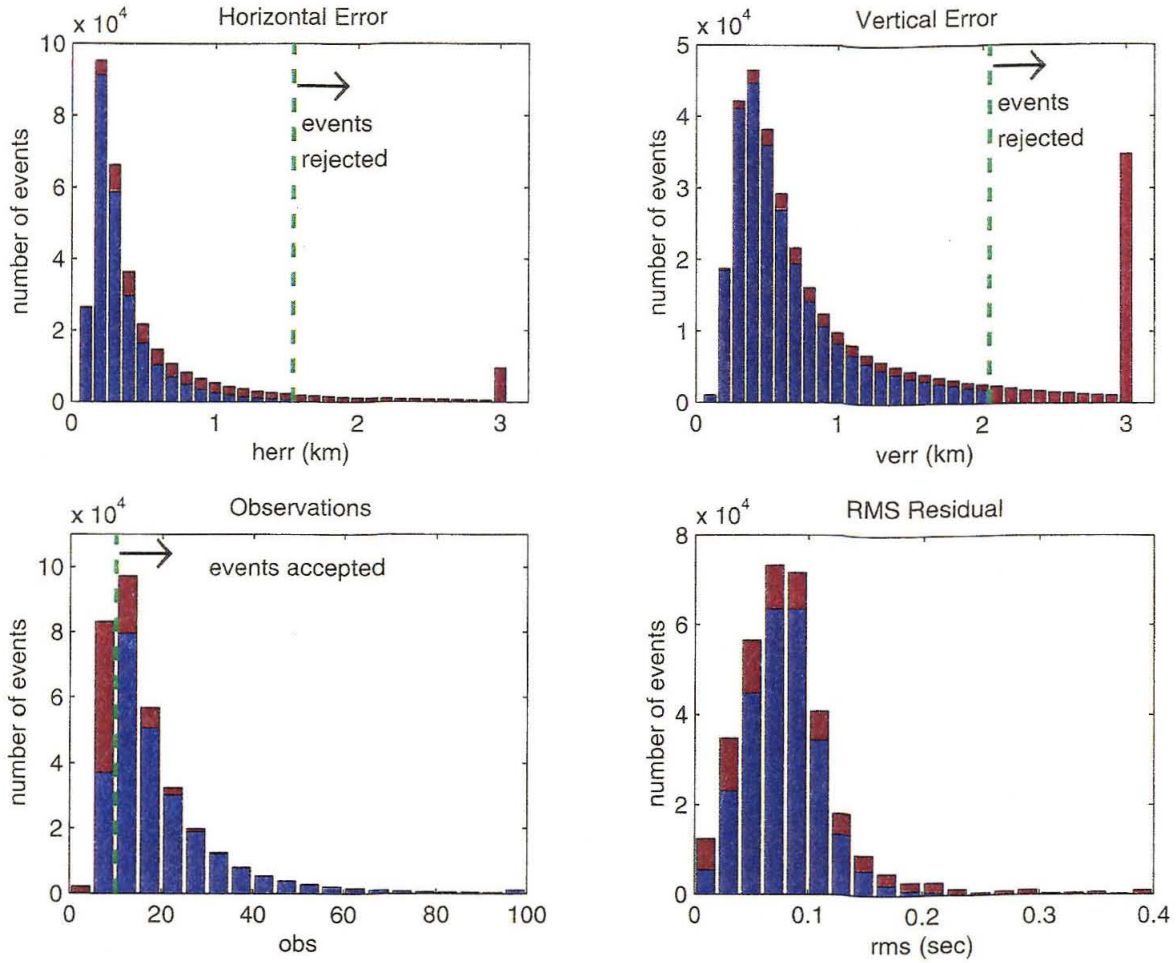

Figure 2.3 Errors in the full earthquake dataset. Events with acceptable errors and sufficient observations are represented by the blue columns (257,918 earthquakes). The brown regions represent the errors of the 75167 earthquakes rejected for one or more unacceptable errors. The green dashed lines show the division between acceptable and unacceptable values. Some events are considered acceptable with less than ten observations if the distance to the nearest seismic station is less than twice the depth. RMS was not used as a sorting criterion. The bar farthest to the right represents all events equal or greater than the bin value, and thus appear much larger than the surrounding bins.

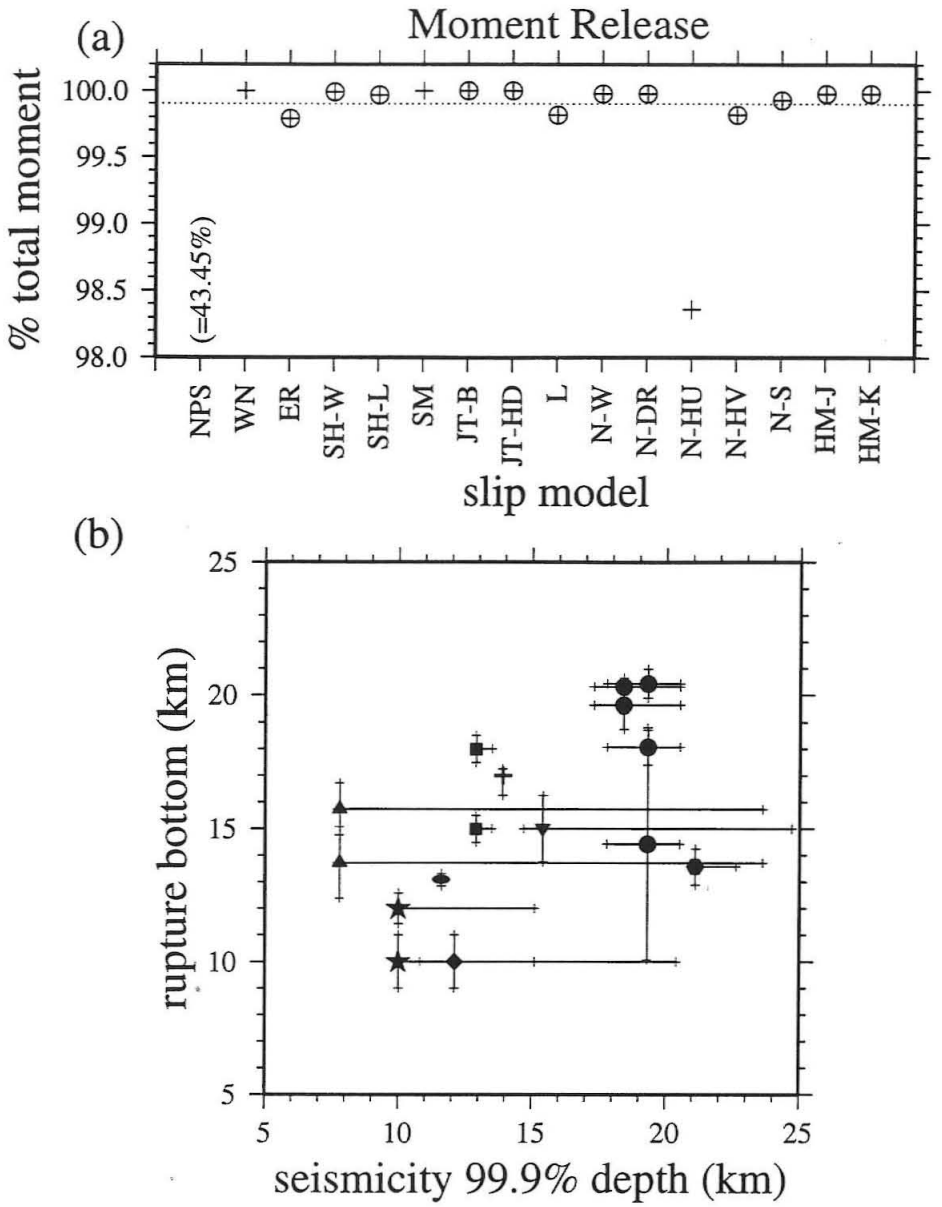

Figure 2.4 **(a) Percent of total moment release of pre-mainshock seismicity that occurred shallower or equal to the rupture bottom of the slip model (see Table 2.1 for slip model references). Circled data points are the values used to calculate the percent depth for southern California (% = 99.9; shown as a dotted line). (b) The 99.9% depth of the pre-mainshock seismicity versus the rupture bottom of the slip model. If the prediction were perfect, the two values would be equal. Horizontal error bars indicate the percent depths for 99.8% and 99.99% (± one standard deviation). Fewer earthquakes occur at depths approaching the maximum depth, so a small change in percent of total moment results in a large change in percent depth. Vertical error bars indicate one-half the width of the slip model sub-faults. Slip model symbols: NPS, hexagon; WN, cross; ER, diamond; SH, star; SM, ellipse; JT, square; L, inverted triangle; N, circle; HM, triangle.**

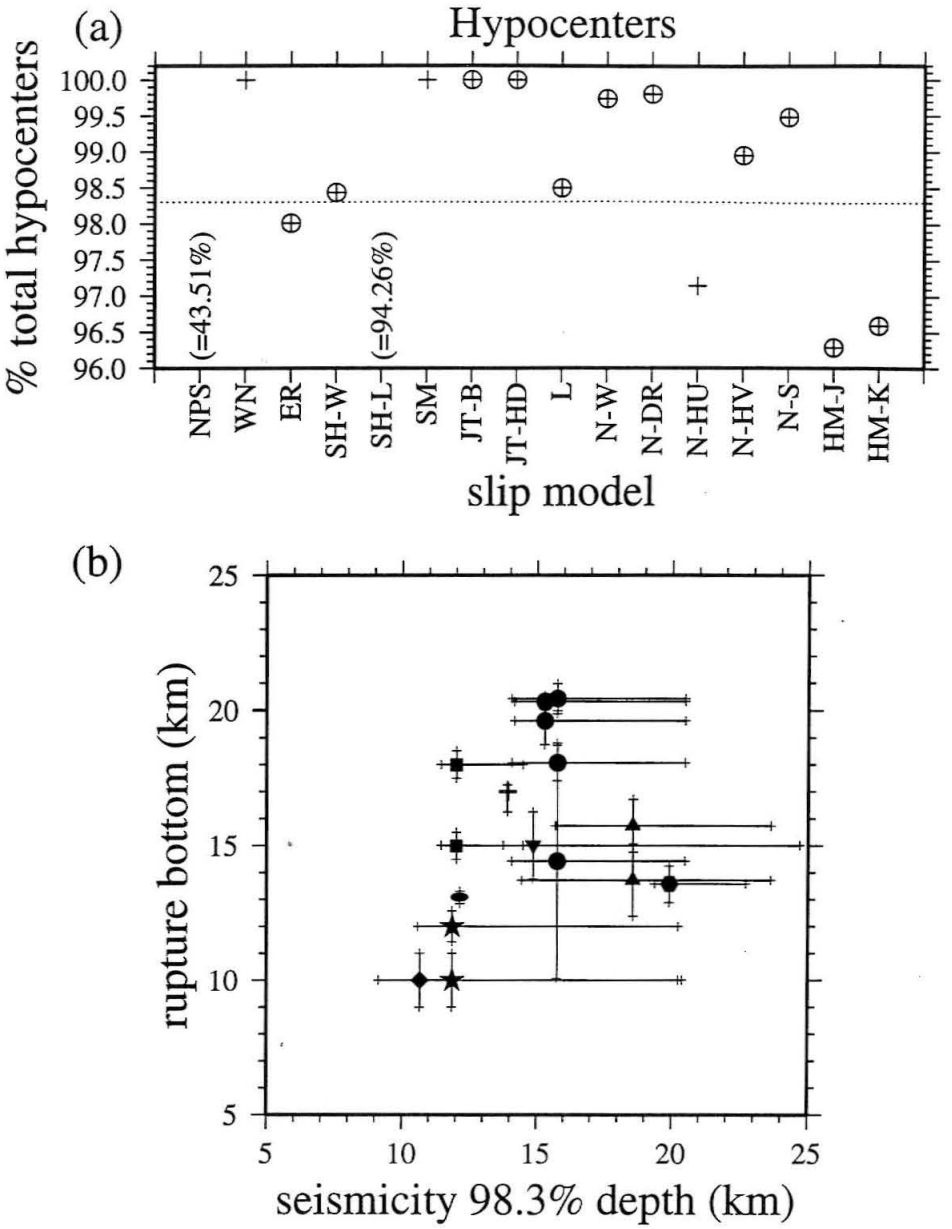

Figure 2.5 **(a) Percent of total hypocenters of pre-mainshock seismicity that occurred shallower or equal to the rupture bottom of the slip model (see Table 2.1 for slip model references). Circled data points are the values used to calculate the percent depth for southern California (% = 98.3; shown as a dotted line). (b) The 98.3% depth of the pre-mainshock seismicity versus the rupture bottom of the slip model. If the prediction were perfect, the two values would be equal. Horizontal error bars indicate the percent depths for 96.5% and 100% (± one standard deviation). Fewer earthquakes occur at depths approaching the maximum depth, so a small change in percent of total hypocenters results in a large change in percent depth. Vertical error bars indicate one-half the width of the slip model sub-faults. Slip model symbols: NPS, hexagon; WN, cross; ER, diamond; SH, star; SM, ellipse; JT, square; L, inverted triangle; N, circle; HM, triangle.**

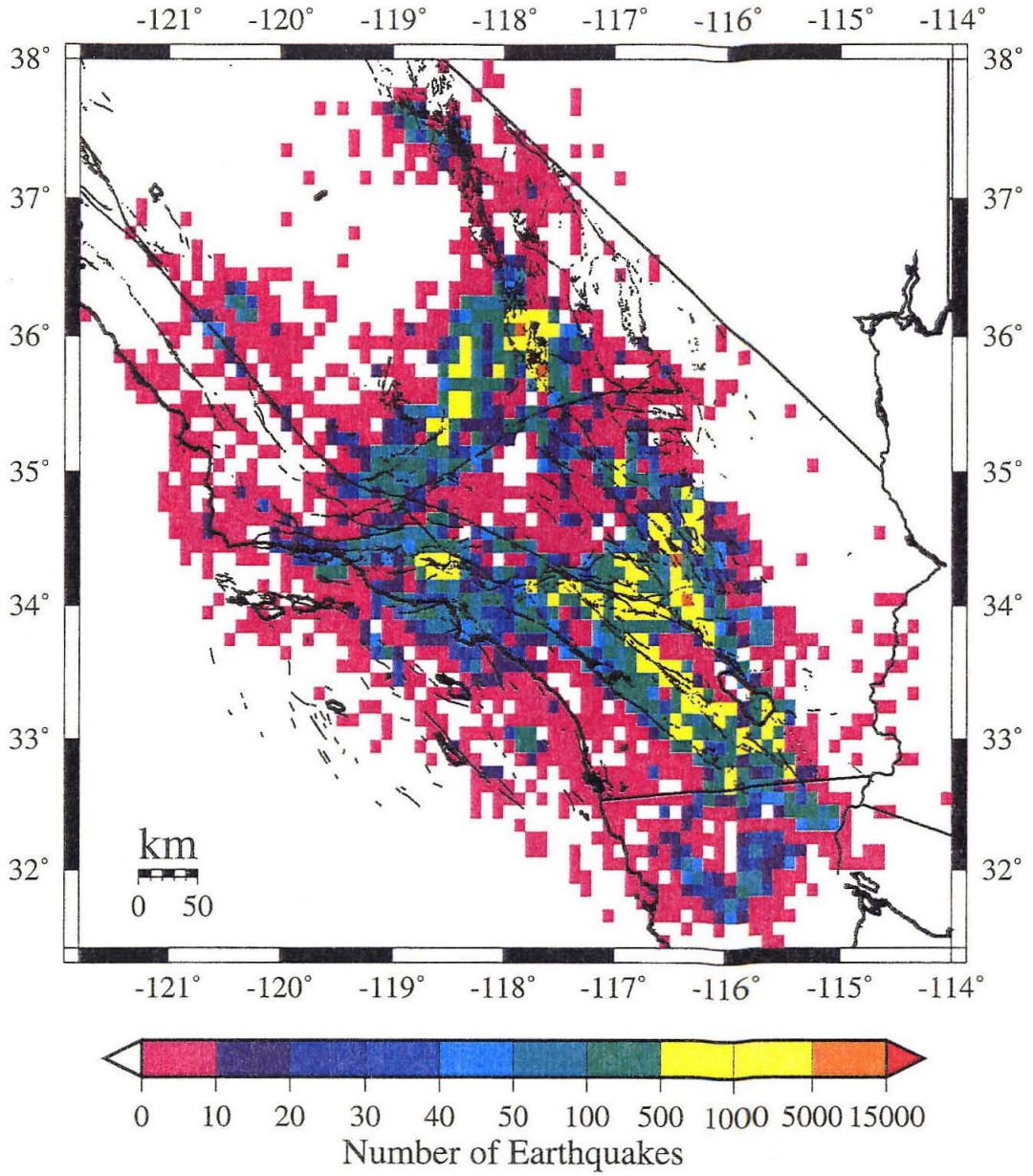

Figure 2.6 Number of earthquakes per regional 0.1x0.1 degree bin. Mapped surface traces of faults (Jennings, 1975) shown as thin black lines.

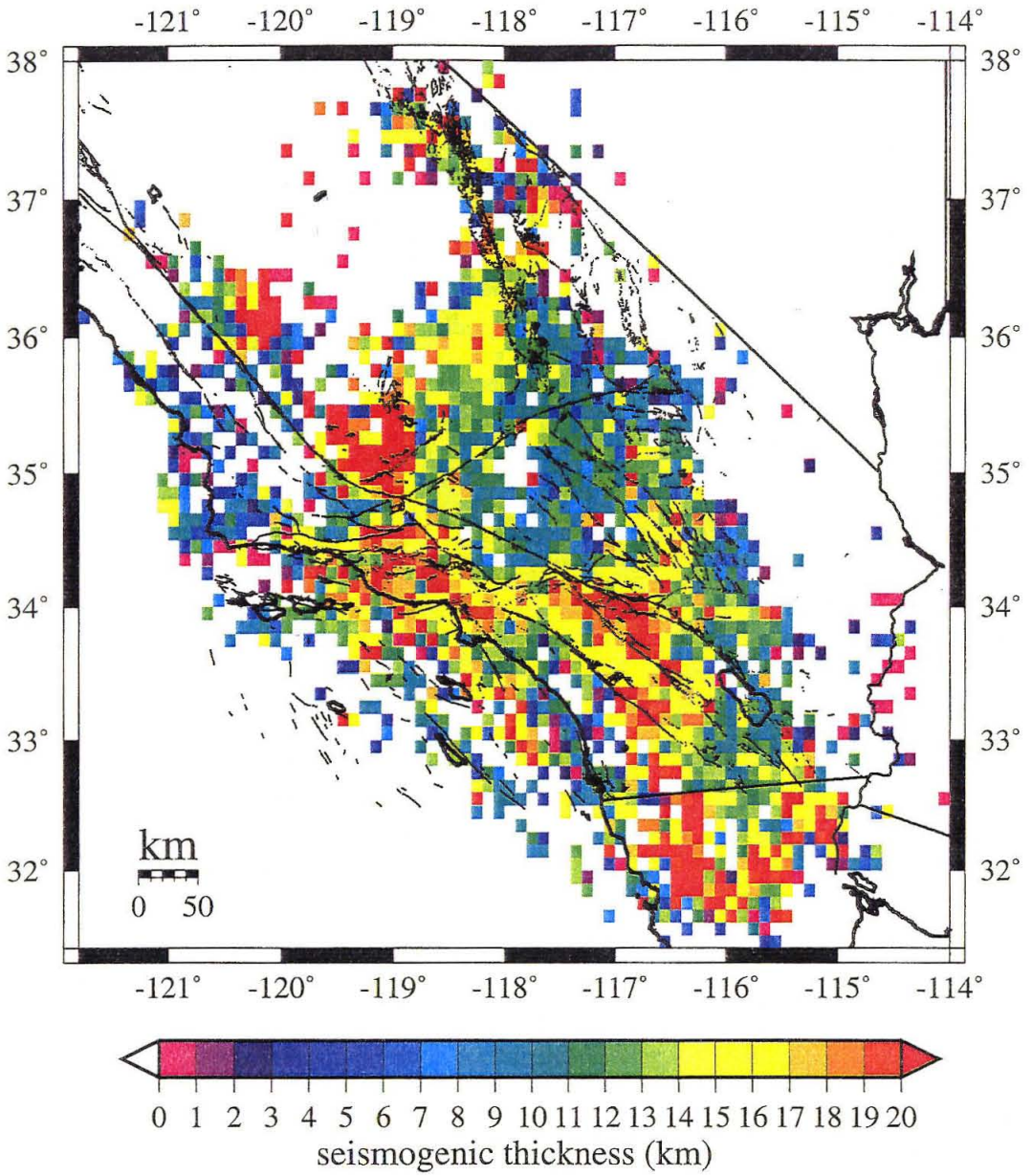

Figure 2.7 The seismogenic thickness for all regional 0.1x0.1 degree bins with data, estimated from the depth distribution of moment release of seismicity located within each regional bin.

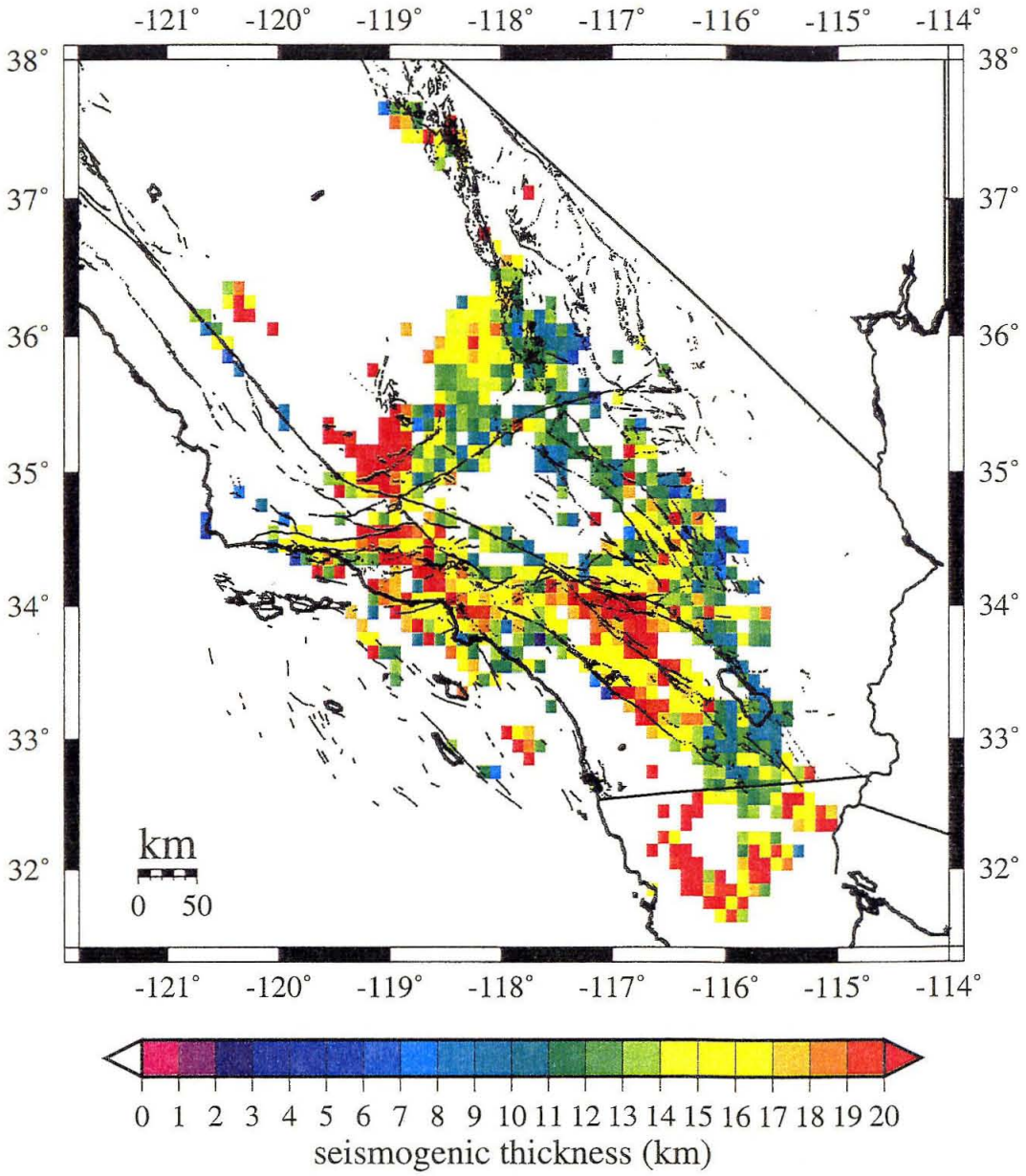

Figure 2.8 The seismogenic thickness for regional bins with ten or more earthquakes, estimated from the depth distribution of moment release.

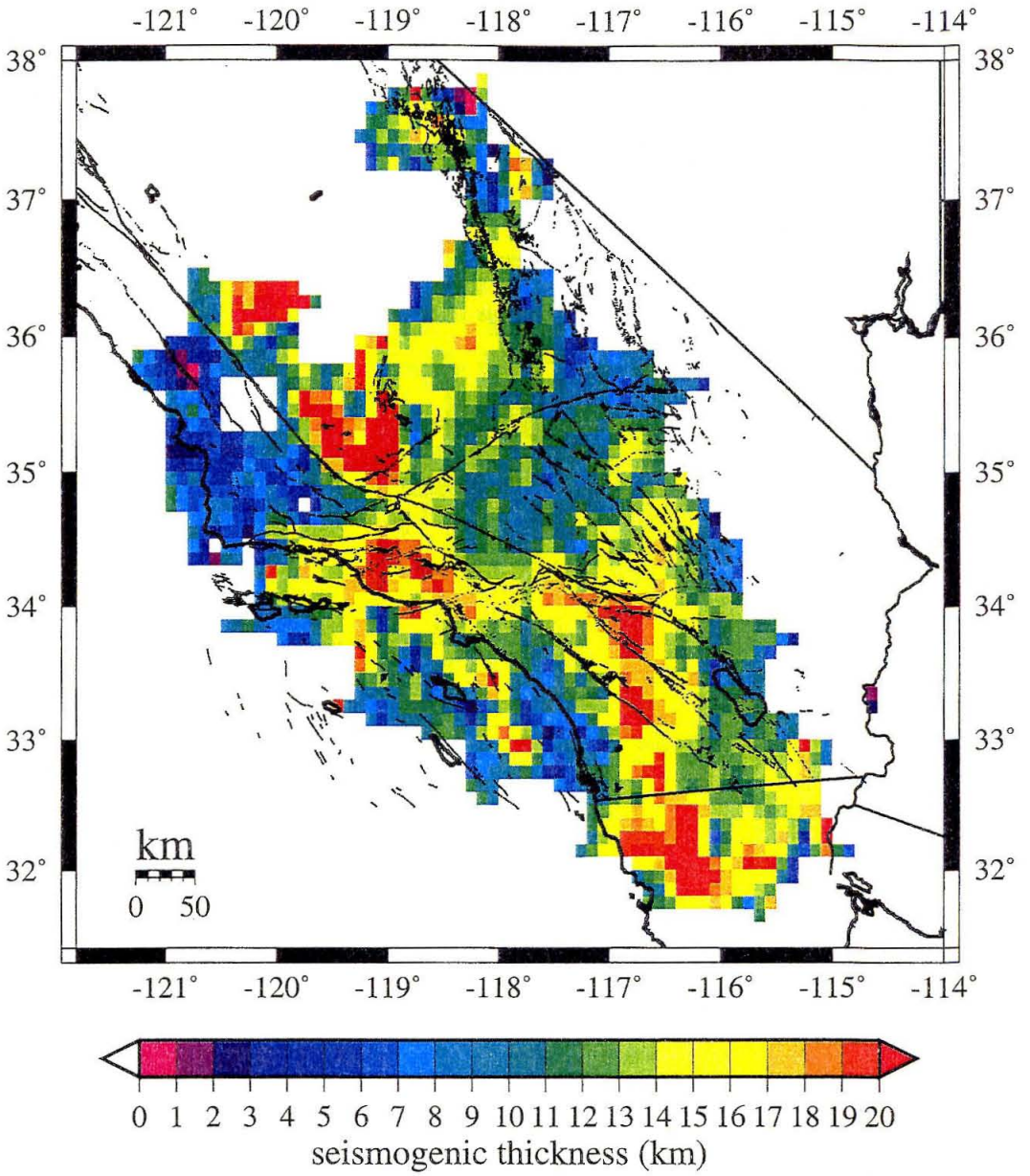

Figure 2.9 Smoothed seismogenic thickness for all regional bins. A gaussian filter (length = 30 km) has been applied to the moment release seismogenic thickness estimate to improve the spatial coherence of the image.

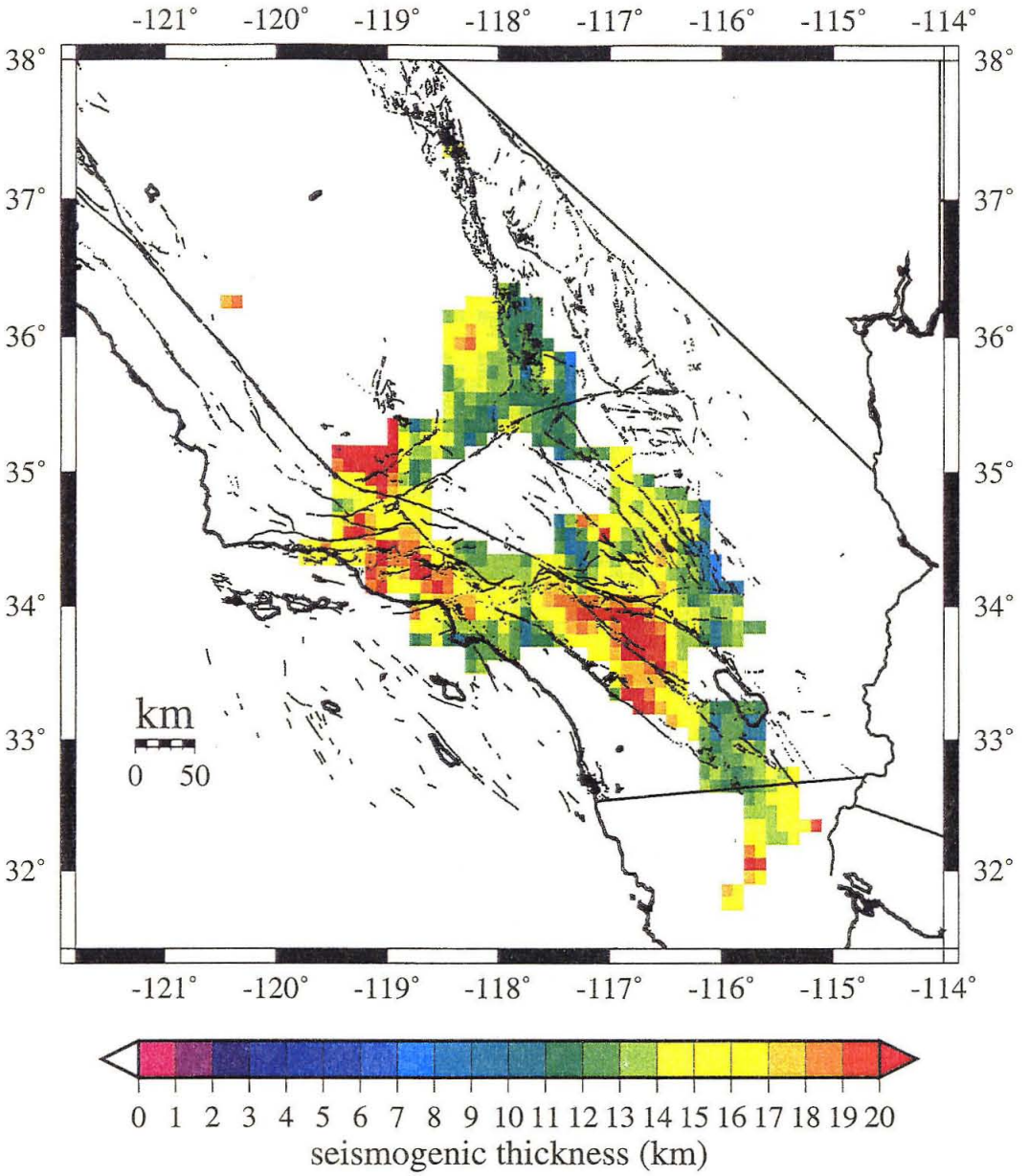

Figure 2.10 Smoothed seismogenic thickness for regional bins with ten or more earthquakes. A gaussian filter (length = 30 km) has been applied to the moment release seismogenic thickness estimate of regional bins with ten or more earthquakes to improve the spatial coherence of the image.

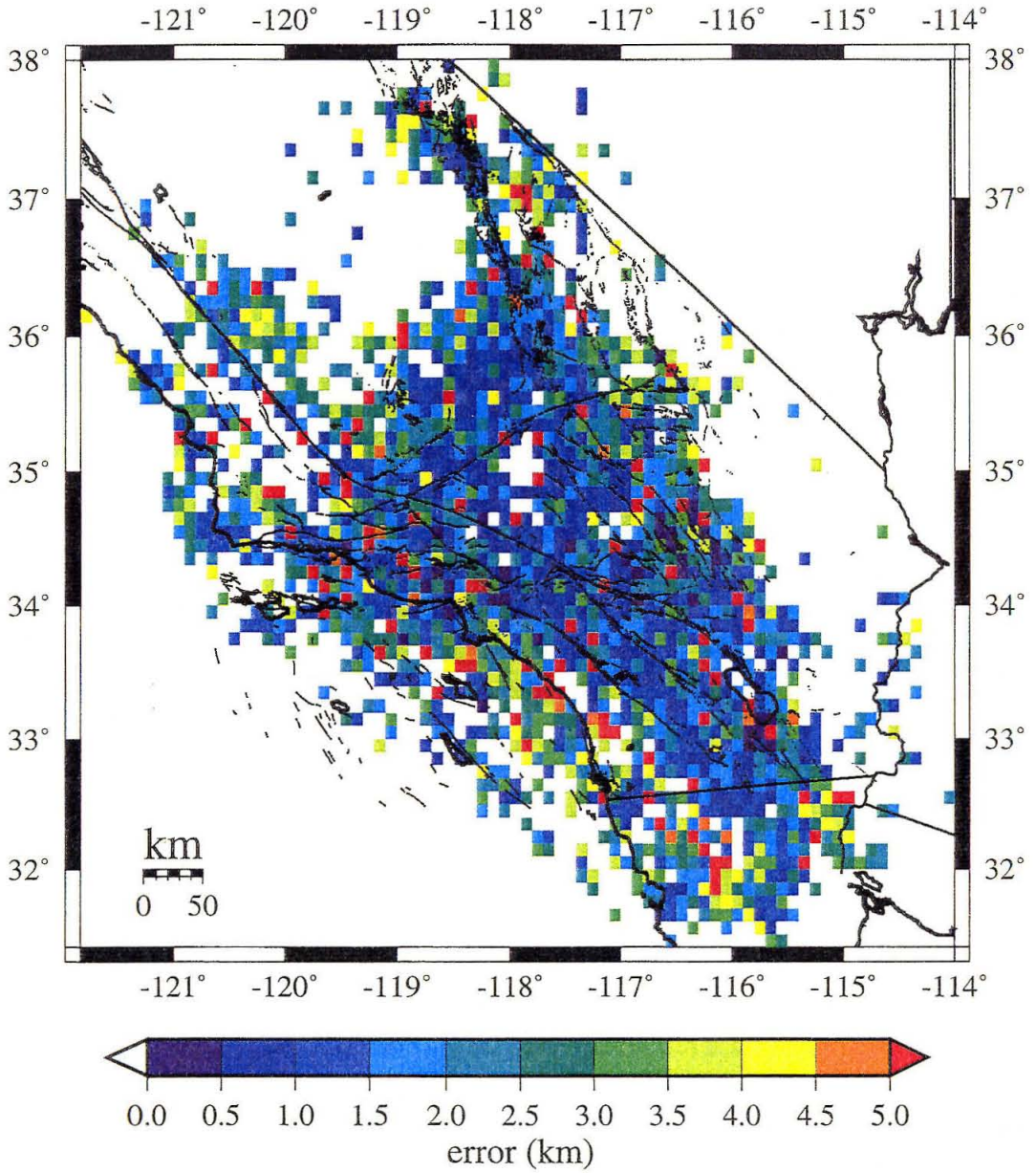

Figure 2.11 Error in the estimate of seismogenic thickness. This is actually the range in the estimate for each regional bin. It is the difference between the percent depths calculated for the deep and shallow moment release distribution extremes. On average, the range is 2.3 km, or +1.2/-1.1 km.

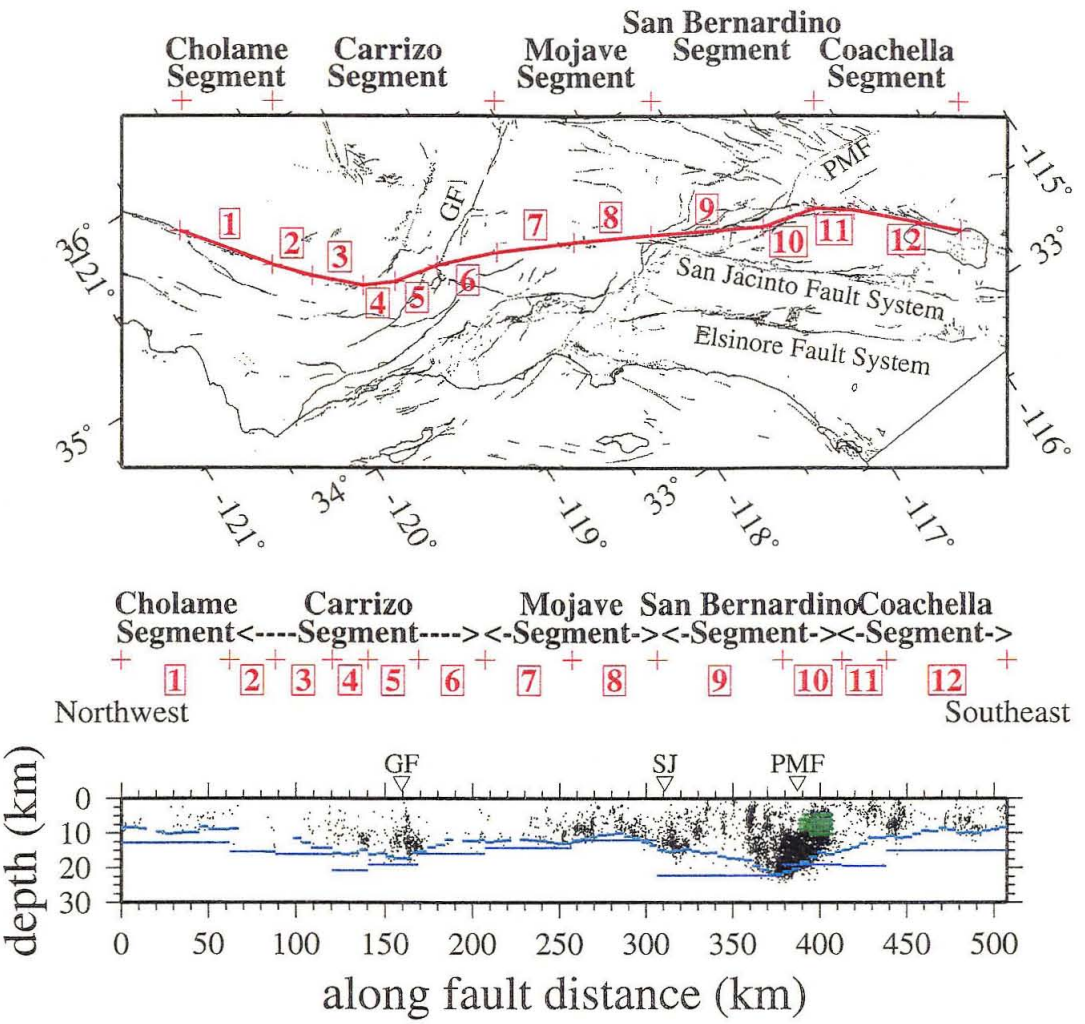

Figure 2.12 Central-Southern San Andreas fault system. (A) Oblique map view showing the CDMG/USGS segments fault in red. Segments are divided into straight line sub-segments and numbered (in red) from north to south. GF, Garlock fault. PMF, Pinto Mountain fault. (B) Cross section along strike with projected earthquakes (black dots) and sub-faults (green dots) within 5 km of the fault, smoothed seismogenic thickness estimates for 5 km along strike bins (cyan lines), and seismogenic thickness estimates for whole sub-segments (medium blues lines). Intersection/projection of faults with the San Andreas fault shown by inverted triangles: GF, Garlock fault; SJF, San Jacinto fault system; PMF, Pinto Mountain fault. Vertical exaggeration 2X.

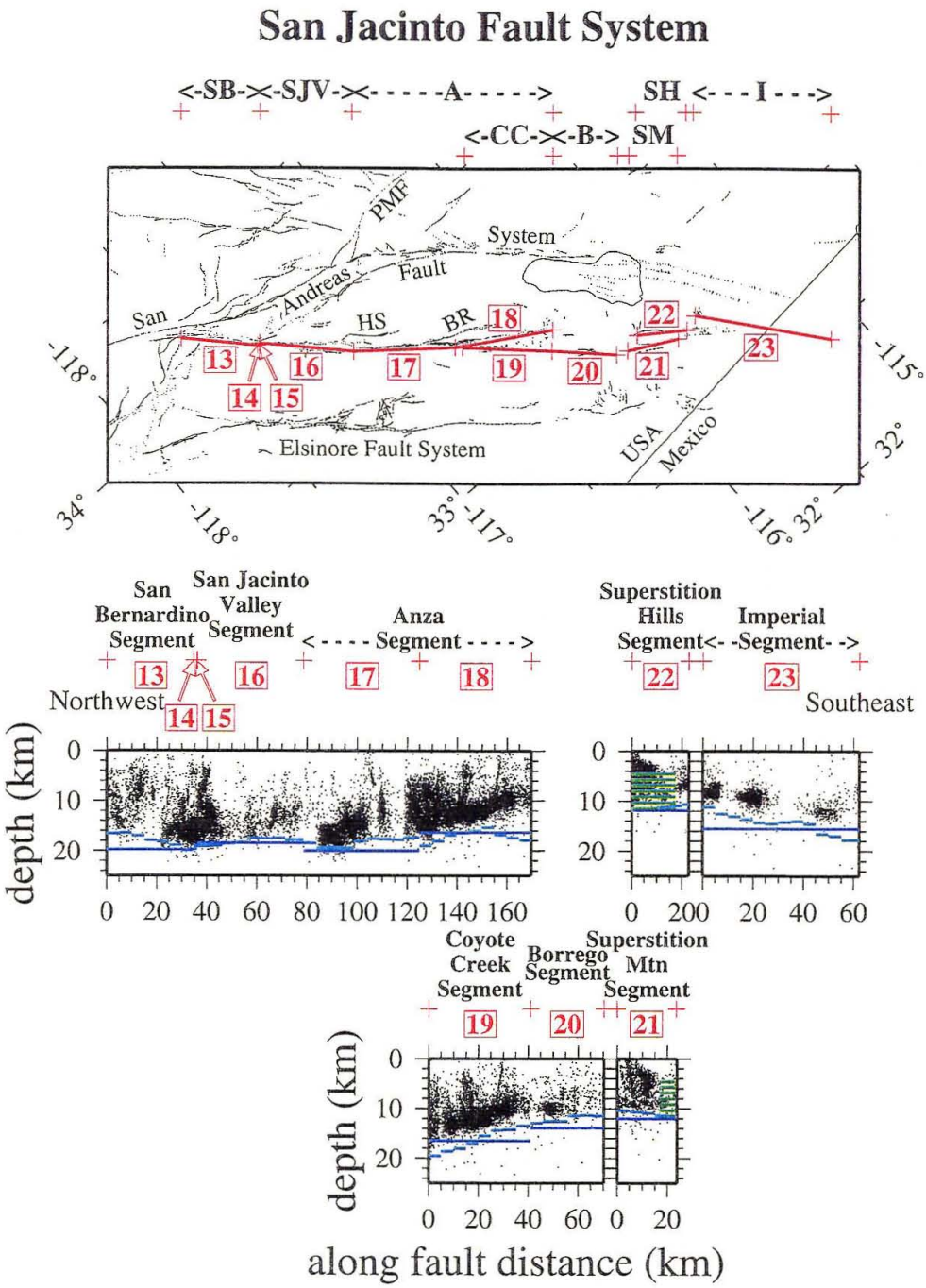

Figure 2.13 San Jacinto fault system. (A) CDMG/USGS segments in red. SB, San Bernardino; SJV, San Jacinto Valley; A, Anza; CC, Coyote Creek; B, Borrego; SM, Superstition Mountain; SH, Superstition Hills; I, Imperial. PMF, Pinto Mountain fault. HS, Hot Springs fault. BR, Buck Ridge fault. (B) Cross section along strike with projected earthquakes (black dots) and sub-faults (green dots) within 5 km of the fault, smoothed seismogenic thickness estimates for 5 km along strike bins (cyan lines), and seismogenic thickness estimates for whole sub-segments (medium blues lines). Vertical exaggeration 2X.

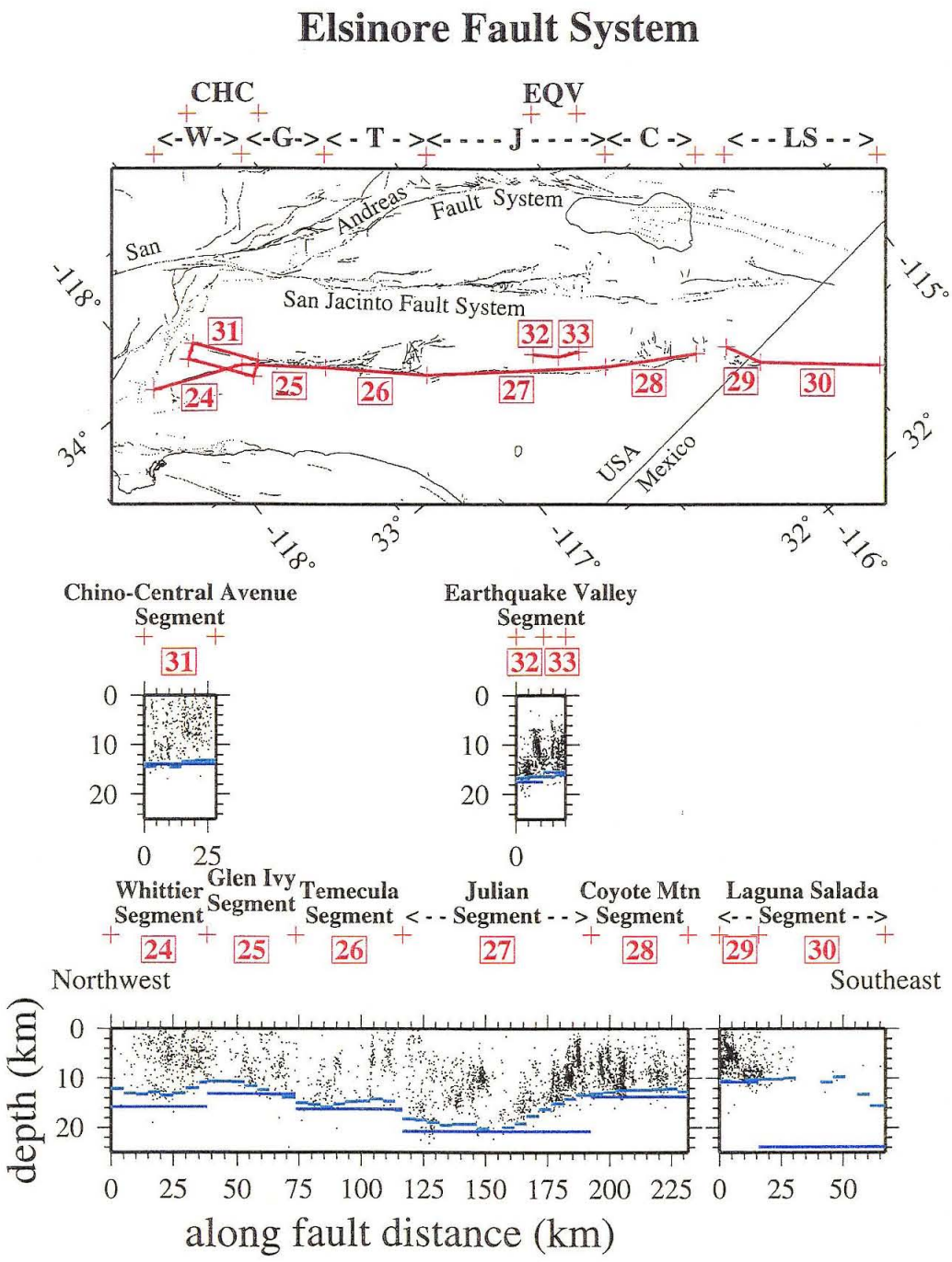

Figure 2.14 Elsinore fault system. (A) CDMG/USGS segments in red. Segment names: W, Whittier; G, Glen Ivy; T, Temecula; J, Julian; C, Coyote Mountain; LS, Laguna Salada; CHC, Chino-Central Avenue; EQV, Earthquake Valley. (B) Cross section along strike with projected earthquakes (black dots) and sub-faults (green dots) located within 5 km of the fault, smoothed seismogenic thickness estimates for 5 km along strike bins (cyan lines), and seismogenic thickness estimates for whole sub-segments (medium blues lines). Vertical exaggeration 2X.

Table 2.1 Finite Source Models

Earthquake	Model	Date	Mech.	Mo (N-m)	Mw	Reference
North Palm Springs	NPS	1986.7.8	OB	1.77E+18	6.13	Hartzell, 1989
Whittier Narrows	WN	1987.10.1	TH	9.45E+17	5.95	Hartzell and Iida, 1990
Elmore Ranch	ER	1987.11.24	SS	2.31E+18	6.21	Larsen et al., 1992
Superstition Hills	SH-W	1987.11.24	SS	4.81E+18	6.42	Wald et al., 1990
	SH-L			9.76E+18	6.63	Larsen et al., 1992
Upland	UP	1990.2.28	TH	2.51E+17	5.57	Dreger and Helmberger, 1991
Sierra Madre	SM	1991.6.28	TH	2.84E+17	5.60	Wald, 1992
Joshua Tree	JT-B	1992.4.23	SS	1.69E+18	6.12	Bennett et al., 1995
	JT-HD			1.46E+18	6.08	Hough and Dreger, 1995
Landers	L	1992.6.28	SS	7.74E+19	7.23	Wald and Heaton, 1994
Big Bear	BB	1992.6.28	SS	5.53E+18	6.46	Jones and Hough, 1995
Northridge	N-W	1994.1.17	TH	1.39E+19	6.72	Wald, Heaton and Hudnut, 1996
	N-DR			1.19E+19	6.68	Dreger, 1994
	N-HU			1.05E+19	6.65	Hudnut et al., 1996
	N-HV			1.63E+19	6.77	Hudnut et al., 1996
	N-S			1.52E+19	6.75	Shen et al., 1996
Northridge Aftershock	AN	1994.1.17	TH	1.01E+18	5.97	Dreger, 1997
Hector Mines	HM-J	1999.10.16	SS	6.19E+19	7.16	Ji, Wald and Helmberger, 2000
	HM-K			6.72E+19	7.18	Kaverina, Dreger, and Price, 2000

Table 2.2 Finite Source Model Rupture Dimensions

Slip Model	columns	rows	length	width	top	bottom	dip	strike	view
			(km)	(km)	(km)	(km)	(deg)	(deg)	(deg)
NPS	11	8	22.00	15.20	4.00	14.93	46	287	17
WN	10	10	10.00	10.00	12.00	17.00	30	280	10
ER	10	5	25.00	10.00	0.00	10.00	90	40	310
SH-W	20	10	20.00	11.50	0.50	12.00	90	127	217
SH-L	10	5	25.00	10.00	0.00	10.00	90	310	40
UP: main	2	2	3.50	3.50	6.00	9.36	74	215	305
UP: asp.	1	1	1.00	1.00	8.00	9.00	90	215	305
SM	7	10	4.90	6.00	9.40	14.00	50	242	332
	(10)		(7.00)						
JT-B	29	20	29.00	20.00	0.00	20.00	90	172	262
	(35)		(35.00)						
JT-HD	25	13	25.00	13.00	4.00	17.00	90	340	70
	(30)	(20)	(30.00)	(20.00)	(0.00)	(20.00)			
L: jv	10	6	30.00	15.00	0.00	15.00	90	355	265
L: hv	9	6	27.00	15.00	0.00	15.00	90	334	244
L: ce	12	6	36.00	15.00	0.00	15.00	90	320	230
BB: NW	16	12	16.00	12.00	2.00	14.00	90	320	230
BB: NE	16	12	16.00	12.00	2.00	14.00	90	230	140
N-W	14	14	18.00	24.00	5.00	20.43	40	122	212
N-DR	29	31	29.00	31.00	5.23	25.57	41	109.6	199.6
		(40)		(40.00)	(1.95)	(28.19)			
N-HU	1	1	10.51	13.28	5.72	14.43	40.96	109.6	199.6
N-HV	10	13	20.00	26.00	1.00	18.06	41	109.6	199.6
N-S: 1a	14	5	30.00	10.70	0.00	9.07	58	122	212
N-S: 1b	14	9	30.00	19.30	9.07	20.95	38	122	212
N-S: 2	6	5	12.90	10.70	0.00	8.51	52.7	119.3	29.3
AN	25	17	25.00	17.00	5.45	16.60	41	109.6	199.6
	(45)	(25)	(45)	(25.00)	(0.20)	(16.60)			
HM-J: llm	11	6	33.00	16.20	0.28	16.41	85	346	76
HM-J: llw	7	6	21.00	15.40	0.26	15.14	75	322	52
HM-J: b	10	6	30.00	16.20	0.27	16.41	85	325	55
HM-K: ll	15	12	30.00	24.00	0.15	23.54	77	325	55
HM-K: b	23	12	46.00	24.00	0.15	23.54	77	345	75
HM-K: sb	15	12	30.00	24.00	0.15	23.54	77	325	55

Table 2.3 Finite Source Model Trimmed Rupture Dimensions

								length	width	top	bottom	Moment	Percent
	Slip Model	L	R	T	B	Columns	Rows	(km)	(km)	(km)	(km)	(N-m)	of Original
*	NPS		1		1	10	7	20.00	13.30	4.00	13.57	1.68E+18	94.6%
*	WN					10	10	10.00	10.00	12.00	17.00	9.45E+17	100.0%
*	ER		2	1		8	4	20.00	8.00	2.00	10.00	2.25E+18	97.5%
*	SH-W		1	3		19	7	19.00	8.05	3.95	12.00	4.41E+18	91.7%
	SH-L					10	5	25.00	10.00	0.00	10.00	9.76E+18	100.0%
*	UP											2.51E+17	100.0%
	UP: main					2	2	3.50	3.50	6.00	9.36	1.76E+17	100.0%
	UP: asp.					1	1	1.00	1.00	8.00	9.00	7.49E+16	100.0%
*	SM	1		2	2	6	6	4.20	3.60	10.47	13.08	2.68E+17	94.4%
		(4)											
	JT-B	4	12	3	2	13	15	13.00	15.00	0.00	18.00	1.52E+18	89.8%
		(7)	(15)										
*	JT-HD	15	3	1	2	7	10	7.00	10.00	5.00	15.00	1.34E+18	92.1%
			(8)	(5)	(5)								
*	L											7.68E+19	99.3%
	L: jv		2			8	6	24.00	15.00	0.00	15.00	1.93E+19	97.9%
	L: hv					9	6	27.00	15.00	0.00	15.00	3.72E+19	100.0%
	L: ce	1				11	6	33.00	15.00	0.00	15.00	2.04E+19	99.2%
*	BB											5.53E+18	100.0%
	BB: NW					16	12	16.00	12.00	2.00	14.00	2.65E+18	100.0%
	BB: NE					16	12	16.00	12.00	2.00	14.00	2.88E+18	100.0%
*	N-W			1		14	13	18.00	22.29	6.10	20.43	1.37E+19	98.3%
	N-DR	8	7	1	8	14	22	14.00	22.00	5.89	20.32	1.05E+19	88.3%
				(6)	(12)								
	N-HU					1	1	10.51	13.28	5.72	14.43	1.05E+19	100.0%
	N-HV					10	13	20.00	26.00	1.00	18.06	1.63E+19	100.0%
	N-S											1.49E+19	96.8%
	N-S: 1a	1				13	5	27.86	10.70	0.00	9.07	3.27E+18	95.3%
	N-S: 1b	1			1	13	8	27.86	17.16	9.07	19.63	9.53E+18	96.7%
	N-S: 2					6	5	12.90	10.70	0.00	8.51	1.90E+18	100.0%
*	AN	7	4	1	4	14	12	14.00	12.00	6.10	13.98	9.48E+17	93.4%
		(17)	(14)	(9)									
*	HM-J											5.93E+19	95.9%
	HM-J: IIm		1		1	10	5	30.00	13.50	0.28	13.72	2.61E+19	97.5%
	HM-J: IIw	1			1	6	5	18.00	12.83	0.26	12.66	2.08E+19	92.9%
	HM-J: b	1			2	9	4	27.00	10.80	0.27	11.28	1.25E+19	97.6%
	HM-K											5.47E+19	81.5%
	HM-K: II		6		4	9	8	18.00	16.00	0.15	15.74	2.48E+19	86.3%
	HM-K: b				4	23	8	46.00	16.00	0.15	15.74	2.02E+19	78.8%
	HM-K: sb				4	15	8	30.00	16.00	0.15	15.74	9.67E+18	75.8%

Table 2.4 Seismogenic Thickness of Strike-Slip Fault Segments

Sub-Segment Number	CDMG/USGS RB (km)	WSS H (km)	mean H (km)	min H (km)	max H (km)	Segment Description
San Andreas						
1	12	12.8	9.1	8.2	10.2	Cholame
2	12	15.4	12.1	8.7	15.4	Carrizo Plain
3		16.2	13.2	11.6	14.3	
4		20.7	15.6	14.8	16.1	
5		19.0	16.4	15.6	17.2	
6		16.0	13.0	11.9	15.2	
7	12	14.2	12.4	11.8	12.9	Mojave
8		12.1	11.5	10.1	13.5	
9	18	22.3	17.0	14.7	21.8	San Bernadino
10		19.1	17.7	15.3	21.1	
11	12	19.4	12.9	11.2	14.9	Coachella Valley
12		15.0	9.7	8.3	11.0	
San Jacinto						
13	15	19.8	17.8	16.4	19.9	San Bernadino
14		19.0	19.7			
15	18	20.7	19.6			San Jacinto Valley
16		18.4	18.2	17.5	19.1	
17	18	20.0	18.3	17.3	19.4	Anza
18		16.3	17.1	15.3	19.0	
19	15	16.4	16.3	13.5	19.4	Coyote Creek
20	12	13.9	12.1	11.3	12.9	Borrego
21	12	12.0	11.0	10.3	11.7	Superstition Mountain
22	12	11.9	11.4	10.7	11.9	Superstition Hills
23	12	15.6	14.5	11.2	17.8	Imperial
Elsinore						
24	15	15.8	12.6	9.3	15.9	Whittier
25	15	13.2	11.9	8.7	14.1	Glen Ivy
26	15	16.3	15.1	13.5	16.7	Temecula
27	15	20.8	18.0	13.0	22.5	Julian
28	15	13.7	12.5	10.2	13.8	Coyote Mountain
29	15	10.7	10.5	10.3	10.9	Laguna Salada
30		23.8	11.4	7.4	23.8	
31	15	13.7	13.7	10.3	16.4	Chino-Central Avenue
32	15	17.3	16.4	14.2	17.4	Earthquake Valley
33		15.4	16.1	15.4	18.0	

2.12. *Appendix A*

We defined the "mainshock region" to be the area outlined by the 24 hour aftershock zone. However, there is no precise definition of the aftershock zone of an earthquake. Aftershocks are assumed to be the result of changes in stress, strain, pore pressure, or other effects in the surrounding crust due to the mainshock rupture. As the 1992 Landers earthquake clearly demonstrated, large earthquakes can increase the seismicity rate in areas beyond the one fault length rule of thumb for aftershock zone description. Here we show the effect of two different interpretations of the 24 hour aftershock zone definition.

We define the 24 hour aftershock zone as "loose" or "tight." This is a simple description of reasonableness when visually identifying the region of aftershocks. The "loose" aftershock region includes scattered aftershocks as far away as a fault length and the map projection of all the finite source models for that mainshock. Often, the majority of the first 24 hours of aftershocks fall into a compact region surrounding the fault plane, where a "tight" region can be identified, which excludes some scattered earthquakes farther from the fault. When based solely upon the aftershock distribution, this region can be smaller than the map projection of the finite source models. If this occurs, the "tight" region is extended to just include the finite source model, where necessary. For earthquakes with multiple models, this may result in the definition of several "tight" aftershock zones, because the map projection of finite source models can vary from one model to the next.

On average, there is not much difference between loose and tight aftershock definitions. The tight definition reduces the number of earthquakes in the region dataset

because the area of the regions is smaller. In the case of the smaller earthquakes (Whittier Narrows and Sierra Madre), the reduction is significant such that the datasets contain less than ten pre-mainshock earthquakes, and results in the under-prediction of maximum depth of mainshock rupture. We believe the under-prediction results from too short a time period covered by earthquake database for regions of low seismicity rate. Background seismicity should fill out the rupture space if given enough time to do so. Using a larger region can provide more pre-mainshock earthquakes (as the "loose" definition does for Whittier Narrows), and potentially a more accurate estimate of the seismogenic thickness. The Whittier Narrows and Sierra Madre earthquakes demonstrate the need for caution when considering a region that has a low rate of seismicity, and are excluded from our estimation of the appropriate percent value for the prediction of seismogenic thickness in southern California.

The tight definition can also reduce the difference in the error extremes by removing some M4-5 earthquakes with large uncertainties from the edges of the regional seismicity zone for some comparisons (e.g., Elmore Ranch). For the tight region definition, the combination of fewer earthquakes closer to the mainshock rupture plane and less earthquake with large uncertainty results in a higher average percent with a significantly lower standard deviation of the mean. Using only earthquakes close to the mainshock (which are expected to be more representative of the crust surrounding the mainshock) results in a marginally better prediction. However, as most of the reduction in the standard deviation of the mean comes from reducing the number of troublesome earthquakes (M4-5 earthquakes with large uncertainties), we do not feel that the definition of the 24 hour

aftershock zone significantly affects the results, as long as the region is reasonably defined around the aftershocks within one fault length.

2.13. Appendix B

In this project, we estimate the seismogenic thickness of an area by looking for the depth above which a specified percentage of the total moment release of the seismicity of the area occurs (the *percent depth*). This is a complex calculation because you must take into account the uneven depth distribution of the earthquakes, as well as the range in amount of seismic moment release and the size of the rupture plane. Because of this, the moment release of the earthquakes must be sorted into depth bins, rather than simply depth-ordered and counted, as in the hypocenter distribution calculation. The size of these depth bins is a trade-off between the precision of the moment release contained in each bin and the number of bins required to contain the entire depth column of the region. Make the depth bin too large, and each step in cumulative percent of moment of the region is large. If the depth bin is too small, the cumulative percent of total moment curve is too jagged and contains many empty bins. This of course, is dependent on the number, and to some degree, the magnitudes, of the earthquakes of the region in question. The fewer the number of earthquakes in the region, the larger percent of total moment release contained in each individual earthquake. If a region contains an earthquake with magnitude that is a significant proportion of the total, large steps in both percent and cumulative percent of total moment occur in the depth bins that the earthquake's rupture plane overlaps. A few different depth bin sizes were tried, and qualitatively evaluated, resulting in a final choice of depth bin size of 0.1 km, with the assumption that the resulting percent depths would be round to the nearest half or whole kilometer.

The choice of the percent of total moment to use when estimating seismogenic thickness came out of a comparison study between large southern California earthquakes,

and the background seismicity of the mainshock region before the mainshock occurred. The cumulative percent of the background seismicity above the bottom of the mainshock rupture plane (from published finite source models) for twelve models of six mainshocks was averaged to produce 99.93% ± 0.07%. Because of the consistency of the cumulative percent values for different earthquakes and finite source models, it was felt that the number could be used to two decimal places in the calculation, and quoted to one decimal place in the paper. The total moment of the background seismicity was at least 10^{15} Nm (for the percents actually used to compute the average), so that 0.1% of the total moment resulted in an equivalent magnitude (if the moment was produced by a single earthquake) of at least *M*2 (rupture plane ≥ 0.1 km^2). The "region of the mainshock" in all cases was larger than the 0.1°x0.1° bins later considered, so perhaps a depth bin of 0.1 km is too small for the succeeding analysis.

The calculation of percent depth works by dividing the moment release of the seismicity into the depth bins, and finding which depth bin has a cumulative percent closest to 99.9%. This results in actual cumulative percents between 99.8% and 100%. Intial processing produced actual percents of 100.00% for nearly 72% of the regional bins. This defeats the purpose of looking for the depth down to which the *vast majority* of the seismic moment release of a defined region occurs (the qualitative description of *percent depth*). Since only 4% of the bins have actual percents of 100% because all moment release is located in one depth bin, we can investigate how using the next shallowest depth bin with moment release affects the predicted percent depth and the actual cumulative percent found for the 68% of regional bins with actual cumulative percent of 100% and shallower moment release.

If regional depth bins with actual percents of 100% are replaced by that of the next shallower bin with moment release, how does that change things? Replacing these percent depths with the next shallower depth bin with moment release results in 72.5% of regional bins with actual percents > 90%, and 44.6% with > 99%. Those actual percents may be a little disappointing until you consider that 54.4% regional bins have less than ten earthquakes in them. The mean actual percent is 81.1 ± 23.1%. For the 45.6% of regional bins with ten or more earthquakes, the mean actual percent is 99.0 ± 2.7%. Only 2% of regional bins have actual percents < 90% and all of these regional bins contain ≤ 25 earthquakes. The mean actual cumulative percent increases, while the standard deviation decreases as the number of earthquakes per regional bin increases, such that for regional bins with ≥ 100 earthquakes the mean actual cumulative percent is 99.9 ± 0.4%. Since we already do not view the regional bins with less than ten earthquakes as having reliable estimates of seismogenic thickness, their low actual cumulative percents need not cast doubt on the rest of the seismogenic thickness predictions.

The picture looks even better if the change in percent depth is considered. Nearly four-fifths of the modified regional bins result in a change of 0.1 km (only one depth bin) in percent depth. This ratio of regional bins holds true for those bins with less than ten earthquakes, even though their actual cumulative percentages may have changed significantly. When considering the full regional bin data set, the average percent depth for southern California decreases 0.5 km.

In conclusion, using the next shallowest depth bin containing moment release, when the actual cumulative percent (closest to 99.9%) is 100%, improves the reasonable-

ness of the procedure by insuring that the *vast majority* but not all of the moment release is considered, without greatly modifying the results for most of the regional bins.

CHAPTER 3

Crustal Structure of the Borderland-Continent Transition Zone of Southern California Adjacent to Los Angeles

3.1 Abstract

We use data from the onshore-offshore component of LARSE (Los Angeles Region Seismic Experiment) to model the broad scale features of the mid-crust to upper mantle beneath a north-south transect that spans the continental borderland in the Los Angeles, California region. The composite velocity model constrains the crustal thickness and location and width of the continent-Borderland transition zone. Layer velocities are similar to the average southern California crust model, except for the higher upper mantle velocity beneath the Borderland. All layers within the Borderland crust are thinner than those of the onshore continental crust, but the lower crust is significantly thinner in the Borderland than onshore. The data require the Moho to deepen significantly to the north, dramatically increasing the crustal thickness over a relatively short distance of 20-25 km. The transition zone is constrained to initiate within a 30 km wide zone, between the off-shore slope and the southwest Los Angeles Basin. If the crustal thickness is assumed to be 22 km for the Borderland, then the transition zone is constrained to initiate within a 6 km wide region beneath the southwest Los Angeles Basin, and have a width of 20-25 km.

The strong, coherent, and continuous Pn phase indicates the Moho is coherent and laterally continuous beneath the Inner Borderland and transition zone. The Inner California Borderland seems to be modified and thickened oceanic crust, with the oceanic upper mantle intact beneath it.

3.2 Introduction

The western margin of the North America plate is an area of active deformation that is in part related to its past subduction history. Although subduction has ceased off the coast of most of California, the subduction legacy on the continent remains in the crustal structure and rocks of the great batholiths, sedimentary basins, and metamorphic complexes. Recent seismic experiments (summarized by Fuis, 1998) along the western margin of North America reveal that historical remnants of subduction (usually underplated fragments of oceanic plates and/or magmatic underplating) can exist and is in fact quite common in the mid to lower crust without obvious surficial expression on the continent. In southern California, subduction of the very young and fragmented Farallon plate terminated approximately 28 Ma as the Pacific-Farallon ridge intersected the Farallon-North America trench [*Atwater*, 1989]. The fate of the slab or slab fragments in this region is unknown.

The Los Angeles Region Seismic Experiment (LARSE) is a multi-phase, multi-component study of the crustal structure of southern California carried out by the Southern California Earthquake Center and the United States Geological Survey [*Fuis, et al.*, 1996]. LARSE includes a passive seismic survey [*Kohler et al.*, 1996], deep crustal reflection and refraction surveys from onshore and offshore sources with onshore and ocean-bottom seismometers, and an offshore multi-channel seismic survey [*Brocher et al.*, 1995; *Okaya et*

al., 1996; *ten Brink et al.*, 1996]. In this paper, data from the onshore-offshore component of LARSE are analyzed.

The onshore-offshore component of LARSE is a wide-angle reflection/refraction experiment designed to investigate the mid to lower crustal structure in the near shore California Continental Borderland and the adjacent continental region. The crustal structure and features of the interface between the oceanic crust and the continental crust in the Borderland region are not well known, but have important implications for both the tectonic history and current tectonics of the Borderland and the greater Los Angeles region. This analysis also provides a link between on-land and marine models of crustal structure in southern California.

The onshore-offshore portion of LARSE (Figure 3.1) crossed four tectonic regions: the (offshore) Inner California Borderland, the Los Angeles basin, the central Transverse Ranges, and the Mojave Desert. Because of the wide-angle nature of the experiment, the area of significance in interpretation of the data is the offshore Borderland, onshore Los Angeles Basin, and the Transverse Ranges.

The California Borderland structural province is characterized by northwest trending ridges separated by broad, flat basins [*Shepard and Emery*, 1941; *Emery*, 1954]. Extensional basins formed during Miocene to Pliocene time [*Bohannon and Geist*, 1998], and were accentuated by a structural inversion to northeast-southwest compression since early Pliocene [*Crouch and Suppe*, 1993]. Most basins contain 2-5 km of sediment, which is a significant portion of the 20-27 km thickness of the Borderland crust [*Couch and Riddihough*, 1989, *Mooney and Weaver*, 1989; *Bohannon and Geist*, 1998]. Recent studies in the region of the LARSE profiles find a crustal thickness of 19-23 km in the area between

Santa Catalina Island and the coastline to the north and northeast [*Richards-Dinger and Shearer*, 1997; *Huksson*, 2000; *Zhu and Kanamori*, 2000; *ten Brink et al.*, 2000]. The Borderland consists of four main lithostratigraphic belts that divide the structural province into the Inner California Borderland (Catalina Schist belt), the Outer California Borderland (Patton accretionary belt and Nicholas forearc belt), and the western Transverse Ranges block (western Transverse Ranges belt) [*Crouch and Suppe*, 1993; *Bohannon and Geist*, 1998]. High P-wave velocities of 6.7 to 7.2 km/s in the middle to lower crust imply an oceanic origin for the crust in this region [*Mooney and Weaver*, 1989].

Located at the intersection of the Peninsular Ranges, the Transverse Ranges, and the California Borderland, the Los Angeles basin is a small but deep basin with thick, mainly Neogene sedimentary fill [*Yerkes et al.*, 1965; *Wright*, 1991]. The 8 km thick basin is underlain by high velocity material [*Hauksson and Haase*, 1997; *Hauksson*, 2000] that may be related to the formation of the ancestral basin in the middle Miocene from block rotations [*Luyendyk et al.*, 1980] or rifting [*Crouch and Suppe*, 1993]. Crustal thickness transitions rapidly beneath the Los Angeles basin from the 22 km of the Inner Borderland to 30 km beneath the Transverse Ranges [*Zhu and Kanamori*, 2000].

The late Cenozoic, east-west trending Transverse Ranges trend across the coast parallel orientation of tectonic features along the western margin of North America. The Transverse Ranges are composed of a series of parallel to sub-parallel ranges and intervening valleys, including the San Gabriel, Santa Monica, and Santa Susanna Mountains, and the intervening San Fernando and San Gabriel valleys in the central portion of the ranges. Uplift of the Transverse Ranges has been attributed to the left stepping bend in the right lateral San Andreas fault and clockwise block rotation during the Miocene [*Ehlig*,

1981]. Crustal thickness beneath the central Transverse Ranges is estimated to be approximately 29 km from teleseismic receiver function modeling [*Zhu and Kanamori*, 2000], Pn travel time modeling [*Hearn and Clayton*, 1986; *Sung and Jackson*, 1992], and from stacking short period PmP phases [*Richards-Dinger and Shearer*, 1997]. *Kohler and Davis* [1997] inferred a 40 km thick crust beneath the San Gabriel Mountains from teleseismic travel time residuals. The San Gabriel Mountains form a high velocity ridge down to at least 20 km depth with velocities as high as 5-6.3 km/s at 1 km depth [*Hauksson and Haase*, 1997; *Hauksson*, 2000].

At the far northern end of the profiles, the Mojave Desert is a broad elevated region of low mountains of Mesozoic igneous rocks and basins with Cenozoic sediments. Elevations of much of the region lie between 600 and 1200 m. The province is approximately bounded by the San Andreas fault to the south and the Garlock fault to the north, with indistinct eastern and southeastern boundaries. Crustal thickness is estimated to be 29-30 km with a flat Moho [*Richards-Dinger and Shearer*, 1997; *Zhu and Kanamori*, 2000].

3.3 Experiment Description

The onshore-offshore portion of LARSE consists of 22,128 air gun shots and 172 on-land vertical seismometers along three profiles in the greater Los Angeles area (Figure 3.1). Energy from the 139 liter air gun array, towed by the R/V Ewing, was recorded over 230 km away in the Mojave Desert. Air gun sources were spaced 50 m apart on average, and the land receivers were nominally spaced 2 km apart. This paper analyzes the southwest-northeast oriented profile shot during the experiment (line 1).

Line 1 extends from San Clemente Island to the Mojave Desert northwest of Barstow. We analyzed ship track L01B (Figure 3.1), which consists of 1307 shots with source-receiver offsets between 30 and 241 km. Of 82 possible receivers, 38 provided adequate quality data for the analysis. Data quality was good for receivers located in the San Gabriel Mountains and on San Clemente and Santa Catalina Islands, moderate to poor in the Mojave Desert, and generally poor along the coast and in the Los Angeles basin. Two stations located in the Puente Hills provide moderate quality data for the general Los Angeles basin region. Poor quality and non-functioning stations produced several data gaps in the Los Angeles basin and San Gabriel Valleys. Basins tend to trap cultural noise and deflect external seismic energy incident from below, producing recordings with low signal to noise ratios. Head wave phases traveling to the San Gabriel Mountain stations travel beneath the basin before turning up to the surface, and are thus not affected.

Figure 3.2 shows the geometry of the experiment in cross section. There is a gap between the air gun sources and the receivers on land; however, the rays sample the structure of the ocean-continent transition at mid-crustal to upper mantle depths. Additional gaps are due to poor quality or non-existent data, such as for the Los Angeles basin. These gaps affect mostly the interpretation of the upper crust, which is not the focus of this paper.

3.4 Data Processing

The onshore-offshore experiment is unusual in that it is both densely sampled (source spacing) and sparsely sampled (receiver spacing) and contains significant gaps in coverage. We have developed an analysis method based on Radon transforms that allows us to determine phase velocities from the well sampled part of the data, and use the sparse

component of the data to constrain interface dip. This type of analysis lends itself most conveniently to models with long-wavelength lateral variations.

The varied environments of the receivers (coast, sedimentary basins, mountains, and desert), and significant cultural noise along large sections of the profile, produced widely varying noise contents in the data from the various sources. This required filters to be designed for each receiver. In general, a bandpass between 5 and 21 Hz was used. For approximately one-half of the receivers, the upper frequency limit was reduced to 12 Hz to diminish cultural noise. An additional notch filter (9-13 Hz) was applied to four of the receivers. Spiking deconvolution was used to reduce some of the ringing that is prominent in the raw data.

3.4.1 Removing the Effects of Near-Source Structure

The only upper crustal regions that affect our data are directly beneath the source region at sea (the down paths from the sources), and the "single" up path of the head waves from the mid to lower crustal interfaces to the receiver (Figure 3.2). There is a unique up path for every receiver on land, but the down paths from each source at sea are identical for every receiver. Consequently, these shallow regions beneath the sources only manifest themselves as static corrections to our data set that are largely offset independent. We have chosen to remove the effects of these regions by empirically estimating a static correction for each source and for each receiver point in the survey.

An alternative would be to calculate the static corrections using velocity models determined from explosion data (in the receiver region) and OBS and MCS data (in the source region). These models, however, were not derived for the purpose of determining the static travel time from the mid and lower crust, and hence tend to leave residual contri-

butions. For example, the MCS data does an excellent job of accurately imaging the seafloor topography and shallow basin structure, but it provides very little information on the seismic velocities of the sediments. Hence, the calculation of a static correction from the MCS image tends to have residual basin structure in it.

The procedure we have adopted is to account for as much structure as possible with the static corrections. We will first account for the upper crustal effects from beneath our sources at sea with a static source correction that can be applied to all receiver gathers. The variations that remain between the receiver gathers will be used to determine the structure of the ocean-land transition zone. This approach will tend to produce the simplest structure that is consistent with the data. The resulting model will also be consistent with the OBS and on land explosion data, since they provide very little constraint on the near vertical travel time from the mid and lower crust.

The filtered data clearly show large lateral travel time variations across individual receiver gathers that appear to be common to all receiver gathers (regardless of offset) and the two major phases, Pn and Pg (Figure 3.3 (a)-(c)). These time variations are due to the near source effects of the seafloor topography and micro-basin structure. The seafloor relief of up to 1 km (Figure 3.3 (d)) accounts for 0.67 seconds of this variation, but micro-basin structure in the offshore is also a major effect, as is clearly shown in the constant offset section for a parallel ship track in the LARSE multi-channel seismic data report (figure 7 of *Brocher et al.*, 1995). The seafloor topography and the offshore micro-basin structure appear to contribute equally to the lateral time variations.

To correct the data for the near source effects, we use a first arrival refraction (head wave) as the pilot for the correction. The onset of the head wave is picked and each trace

is linearly shifted along the time axis to align the arrival across the section. We pick the arrival times of the head wave by cross-correlating with a representative wavelet chosen from the gather. Obvious cycle skips are edited by hand. Approximately 12% of the traces were eliminated because of bad waveforms, apparent cycle skips, and noise. The mean of the picks is removed, so that a constant time shift is not added to the data. This correction is then applied to every receiver gather along the profile. Although the correction is based upon a single phase (Pn), it works well for all head wave arrivals in the receiver gather because the difference in travel path between the middle to lower crustal head waves is less than 5° in the seawater. Pn was chosen because it is the strongest arrival over much of the source-receiver offsets for this profile and the first arrival at most of the offsets. Reflected phases can be treated in the same manner because their move-out is linear for the range of offsets in this study. The error in processing the PmP phase (which is not linear at these offsets) in this manner is estimated from ray tracing tests to be on the order of –0.10 to + 0.10 s. These errors will result in slight smearing of the Radon transform, which is discussed next in the processing.

Long-wavelength variations can present a problem for static corrections. For example, a systematic dip in the sea floor towards the offshore will make the arrivals appear apparently slower than they really are. In this study, we separately estimate the apparent dip of the sea floor and remove its effect in the calculation of layer velocities. With a dip of 0.5 degrees and upper crustal velocities of 2.0-5.0 km/s, we estimate the apparent slownesses to be increased 0.0014 to 0.0044 s/km. This results in apparent velocity modifications of 0.1-0.3 km/s slower for true velocities between 6.0 and 8.3 km/s.

To estimate phase apparent velocities and intercept time, we apply a Radon transform to the corrected receiver gather [*Yilmaz*, 1987]:

$$S(p, \tau) = \int PX, \tau + pX)dX \qquad \text{(EQ 3.1)}$$

where p is the ray parameter, X is the offset, $\tau = t\text{-}pX$ is the time intercept, and t is the travel time. The Radon transform separates arrivals based on their respective horizontal slownesses and time intercepts. It averages over imperfections in the near source correction on individual traces, and gives the average horizontal slowness and time intercept of the phase, so consequently has the effect of laterally smoothing the velocity structure. This is appropriate since most of the rays in this data set are primarily horizontal (head waves) and hence already average over lateral variations. We apply an envelope function to the transformed data, to help in picking the various phases.

3.4.2 The Picking Process

The main interpretive step in this analysis is in picking the phases in the Radon transform. We demonstrate this with a synthetic example. The synthetic travel times from an average southern California crust model [*Wald et al.*, 1995] have been convolved with a representative waveform to simulate the multiple reverberations found in the actual data (Figure 3.4 (a)). The resulting envelope of the Radon transform is shown in Figure 3.4(b). A full range of source-receiver offsets would result in a series of stacked ellipses as shown by the dotted line in Figure 3.4(b), with the head waves located at the intersection of the ellipses (filled circles), wide-angle reflections along the outside curve, and pre-critical reflections on the inside curves. However, the range of offsets limits the data to head waves and wide-angle reflections, so we are left with a monotonic curve. Reverberations in the data lead to an elongation of the curve in the τ direction, so head wave points

become approximately elliptical with the long axis in the τ direction. The width of the amplitude peak in the τ direction is proportional to the length of the wave train of the arrival.

To simplify picking and increase accuracy, we find the maximum amplitude of each column (*i.e.*, for every value of horizontal slowness, p) and each row (*i.e.*, time intercept, τ). The corresponding curves for our synthetic example are shown in Figure 3.4(c) and Figure 3.4(d) with numbered lines indicating the location of the picks. We show the picks as crosses on the Radon transform envelope (Figure 3.4 (b)). The six peaks of varying amplitude in Figure 3.4(d) represent the average horizontal slownesses of the reflected and refracted phases that result from this model. The reflected phases (numbered P1, P3, P5) will have broader peaks along the p axis than the head waves (numbered P2, P4, P6) with the Radon transform. The shallower reflections (numbered P1 & P3) are approximately linear in the time section at the offsets in this model (similar offsets to that found in the LARSE data), so they produce narrow peaks along the p axis. The largest amplitude of every peak corresponds to the time of the maximum amplitude in the wave train of the arrival (a 0.38 s delay for this example), not the onset of the arrival. The relative time differences between the phases are maintained, but the static time shift implies a thicker upper crustal layer. We estimate the peak amplitude within the wave train reverberations to be delayed approximately 0.25 s for this data set and thus decrease the value of all τ picks by this amount during velocity modeling.

Radon transforms are computed for each receiver gather and picked individually. All major peaks in amplitude are initially assumed to represent refracted or possibly reflected phases, and their p values are picked from the column maximum curve. The cor-

responding time intercepts of those p picks are simply the τ values that have the same amplitude as the p pick. Figure 3.5(a)-(d) shows the time section, radon transform envelope, and the corresponding column and row maximum curves for a station located in the San Gabriel Mountains. The solid lines in Figure 3.5(c) and Figure 3.5(d) indicate the picked peaks for this station. Unlike the synthetic section in Figure 3.4, the radon transform envelope in Figure 3.5(b) has energy distributed away from a single curve due to coherent noise in the time section. This noise contributes to uncertainty in our picks. The peaks are picked by eye, and the uncertainty is estimated from 95% of maximum peak amplitude. This allows us to estimate the uncertainty in our p picks and therefore the uncertainty in the corresponding time intercepts.

The picks from all of the stations are combined to identify trends in the picks. We assume that picks with p values that show a trend across multiple stations represent refracted or reflected arrivals, and use the apparent slownesses and time intercepts to estimate velocity structure. Figure 3.6(a) shows all 251 initial p picks for all the stations, as a function of the nearest source-receiver offset. Some trends can be identified, but the picture is confused by picks that are only located on one station. We further filter the picks by only using picks with amplitudes greater than or equal to 70% of the maximum amplitude of the radon transform envelope or with amplitude greater than or equal to ten (Figure 3.6 (b)). This leaves us with 187 picks with average 95% peak uncertainties of 0.001 s/km for p, and 0.165 s for τ. Note that trends with consistent p values of ~0.1630 s/km, and ~0.1230 s/km, are now obvious. Less obvious trends at p values of ~0.1520 s/km, and ~0.1180 s/km are revealed.

The trends are then checked against the corrected travel time data. This is to verify that the picks are not due to large amplitude arrivals that appear only on a few traces. These unexplained phases are likely due to imperfect near-source corrections, but can produce "ghost" picks trends with significant amplitude in the radon transform. We identified a ghost pick trend of ~0.1196 s/km in the LARSE data (labeled by arrows in Figure 3.6(b)).

3.4.3 Velocity Model Construction

To model the mid and lower crust of the borderland and transition zone, we have chosen a simple layered model with linear interfaces. The interfaces are allowed to dip, and layer thickness may change along the length of the profile. This appears to be the simplest class of models consistent with the data. The complexities of the upper crust are mapped into the upper layer of the model, near-source static corrections, and receiver station delays.

For horizontal layers of constant velocity, ray parameter, p, and time intercept, τ, would be invariant with distance. In the case of layers with constant dip and velocity, p would be distance invariant and represent the inverse of the apparent velocity of the lower layer, while τ would vary with distance in a linear fashion. The slightly more complicated case of a flat-ramp layer (horizontal layers beneath the sources changing to a constant dip beneath the receivers) results in distance invariant p representing the true horizontal slowness of the lower layer and τ that would vary with distance in a linear fashion.

Our experiment only has shots on the ocean side, giving us only one of the needed apparent velocities to calculate true layer velocity and dip if we assume a constant dip layer case. However, the design of the experiment with multiple shots and receivers

allows us to invoke reciprocity and effectively reverse the profile. This allows us to determine the apparent velocities in each direction. Phase velocities for receiver gathers are determined by the Radon transform method described above. However, since source gathers are not recorded across the entire array due to the noise problems described earlier, we use multiple receiver gathers to estimate the phase velocities and time intercepts in the landward direction.

Our p picks give us either the updip or downdip slowness depending on which direction the rays are traveling relative to the interface dip. The change in τ as a function of offset, $d\tau/dx$, is equal to the difference in updip and downdip slownesses for that particular interface:

$$\frac{d\tau}{dx} = p_d - p_u \qquad \text{(EQ 3.2)}$$

Using a small dip approximation, lower interface slowness becomes

$$p_i = \frac{1}{2}(p_d + p_u) = \frac{1}{2}\left(p_u + \left(\frac{d\tau}{dx} + p_u\right)\right) \qquad \text{(EQ 3.3)}$$

This approximation is valid for dips of less than 10°, and has percent errors in the range of a few percent (1-3% for reasonable structure, with 5% for pathological cases; Palmer, 1986). For a series of stacked dipping layers, the approximation is still valid, but may slightly overestimate the true layer velocity [Palmer, 1986].

3.5 Results

3.5.1 Picks and Station Delays

The three p pick trends identified in Figure 3.6(b) are shown separated from the other picks in Figure 3.7(a)-(c) with their corresponding τ picks shown in Figure 3.8(a)-(c). A least squares linear fit is applied to the τ picks for each phase. Any variation in the τ picks away from a linear trend are modeled as station delays that are assumed to origi-

nate near the receivers. The best fit line is calculated for stations in the San Gabriel Mountains and Mojave Desert (nearest source-receiver offsets > 80 km). We do not use the coastal and basin stations in the fit because the varying thickness of very slow sediments of the Los Angeles Basin in the upper crust produces delays that cannot be approximated by a simple static shift and would require a more detailed knowledge of the basin structure to use.

The station delay for each receiver is the average of the deviations for all the phases picked at that receiver. The station delays are removed from the picks and least square fits are applied again to each phase. The small remaining residuals are assumed to be due to minor differences in the ray paths for the various phases in the upper crust and errors in picking.

Station delays are calculated by averaging the deviations from the straight line fits for all phases picked at a certain station. Figure 3.9 shows the average stations delays and the estimated elevation statics for line 1. The uncertainties for the Mojave Desert stations (nearest source-receiver offset > 120 km) are in general larger than those for stations in the San Gabriel Mountains. Coastal and basin stations (nearest source-receiver offset < 65 km) have the largest uncertainties or may have only one phase picked per station.

The largest station delays are found in the basin and coastal stations, with delays greater than 1.0 s. These delays decrease to the north indicating that the rays are traveling through a thinner sediment column. This is expected, as the northernmost two stations are located in the Puente Hills, north of the Los Angeles structural basin. Coastal stations would lie on the southwestern edge of the Los Angeles basin and would be expected to have smaller delays because the rays would be presumably traveling only part of their up

paths through the Los Angeles basin. Relative station delays for the San Gabriel Mountains are within ±0.25 s. Surprisingly, the delays show no correlation with receiver topography.

Figure 3.10 (a)-(c) shows the time intercepts after removing the average station delays, and the single line slope fits to the new τ values. The τ deviations for most picks are much smaller after removing the average station delays. Picks with uncertainties in the station delays greater than 0.4 s are not used to calculate the new straight line fits (plotted as +, Figure 3.10(a)-(c)). Large uncertainties indicate stations with bad picks, local complexities in the upper crust, or three-dimensional effects that cannot be modeled with our analysis. As we are interested in the overall broad-scale structure of the region, the loss of a few stations is not important.

3.5.2 Exploring the Model Space

Although we have constraints that limit the velocity model, a range of possible models will satisfy the data we have. We explore the end member structural models that define the range of possible models. Presumably, velocity models with structure intermediate to the end members will also satisfy the pick data to the same degree.

The p and τ picks provide three sets of constraints for every phase to be used in construction of the velocity model. The first constraint is the apparent horizontal slowness of the phase, represented by the average p, determined as described above. Second, we use the slope of the τ line, $d\tau/dx$, which indicates the changes in the interface depth between stations along a profile. If there is no change in depth of the interface between stations (*i.e.*, the interface is horizontal), $d\tau/dx$ is zero. A positive value of $d\tau/dx$ indicates the interface dips down toward the direction of increasing source-receiver offset, while a

negative value indicates the interface dips up. Our third constraint is the intercept of the τ fit line, which indicates the thickness of the crust above the interface.

We define two types of interfaces as structural end members: constant dip and flat-ramp interfaces. The constant dip interface model (Figure 3.11 (a)) is defined by two depth parameters (*d1*, *d2*) that control the dip and absolute depth of the interface, and the velocity (v) of the layer beneath the interface. Velocity is estimated using the small dip approximation of horizontal slowness for dipping layers in Equation 3.2. The flat-ramp interface model (Figure 3.11 (b)) is defined by three parameters (*d1*, *d2*, *k*) that control the depth of the flat, and the dip and location of the ramp. Because the interface is flat beneath the sources, the apparent horizontal slowness measured for the phase is actually the true slowness (or $1/v$) for the layer beneath the interface. Gaps in the receiver coverage allow a range of flat-ramp interface models, with kink locations between southern and northern limits. The southern kink interface model is limited by the assumption that the arrival from that interface is a straight line in the time domain (*i.e.*, same slope at all offsets). The northern kink is limited by the assumption of a single linear fit to the τ data for the phase in question. When it is reasonable (but not required) to fit two separate $d\tau/dx$ slopes to the τ pick data (*e.g.*, phase B, Figure 3.10(b)), the kink could be located farther north such that the τ picks show a kink (named: station kink end member).

When constructing our velocity model, we consider each interface individually, to determine the range of possible interface models that fit the data constraints. However, to reach deeper interfaces, the rays travel through all interfaces located above. We must consider all possible configurations for the shallower interfaces when modeling deeper interfaces, creating a model tree. Our model tree is topped by the three interface

configurations for modeling phase A (constant dip, and southern and northern kink flat-ramp). Combining the four possible configurations for phase B (constant dip, and southern, northern, and station kink flat-ramp) with the three interface end members for phase A results in twelve interface end members for interface B. Considering three configurations for phase C (constant dip, and southern and northern kink flat-ramp) in combination with the 12 interface end members for phase B results in 36 possible interfaces for phase C, at the base of our model tree.

To construct a velocity model of the crust, we must start at the top of the crust and work our way down to the upper mantle. The wide-angle nature of the experiment precludes information on the upper crust, so we assume a velocity of 5.0 km/s. Near surface velocity anomalies by the receivers will be mapped into the station delays. The apparent velocities of phases A, B, and C suggest they represent velocities of the mid-crust, lower crust, and upper mantle, respectively. We will henceforth refer to the interfaces separating the upper crust, mid-crust, lower crust, and upper mantle as interfaces A, B, and C.

Using the forward ray tracing program XTRAMP [*Zelt and Smith*, 1992], we find the combination of parameters *d1*, *d2*, and *v* or *k*, that produce the lowest interface model error for the interface in question. We define interface model error as

$$E = \sqrt{\left(\frac{1}{(N-1)}\right)\sum_{i=1}^{N}(\tau_i - T_i)^2} \qquad \text{(EQ 3.4)}$$

where τ_i is the time intercept pick of the *ith* station, T_i is the calculated time intercept to the i^{th} station from ray tracing, and N is the number of stations with τ picks for the phase in question. Thus, this error looks at the misfit of only the model interface in question, regardless of how many other interfaces the rays must traverse to reach this interface. We

constrain our search by only considering interface models that produce the apparent p, and $d\tau/dx$ (within the uncertainties), measured for the phase being considered.

Table 3.1 lists the model errors for all 51 A, B, and C interface models for comparison. The three constant dip interface models for interface B (Table 3.1: #14, #24, #34) pinch out at or just beyond the left side of the model. Although these models are valid within the constraints of our data, we favor the flat-ramp models more because we believe the mid-crust to be continuous in the Borderland. Interface C models are full crustal velocity models, and outline the range of structures that satisfy our data. Interface C is treated slightly differently from A and B, because the northern kink locations are not constrained by the assumption of a single linear trend. Instead, model errors slowly increase as the kink location is moved farther north. We choose to constrain the northern kink location to have model errors less than or equal to the estimated average uncertainty in picking the τ peaks ($\sigma = 0.165$ s). The southern kink location is again limited by the assumption of straight arrival in the time domain, but also satisfy the assumption of interface model error ≤ 0.165 s. The 12 interface C constant dip end members (Table 3.1: #109-112, #209-212, #309-312) have interface model errors 1-2 s greater than the flat-ramp end members. These models did not work because interface C pinched out at interface B before the interface was shallow enough to match the intercept of the τ fit curve.

3.5.3 Composite Velocity Model

The composite velocity structure of Figure 3.12 shows the crustal structure across the transition zone between the thin crust of the Inner California Borderland and the thicker crust onshore. Although some interface B end members intersect with interface C end members beneath the Borderland in this figure, the respective interface structure for

individual velocity models do not. The cross-over simply indicates the thin lower crust in the Borderland and the range of possible Moho depths offshore. The shaded region surrounding the interface C end members outlines the region of crust where the Moho is located. Not every interface within this region will satisfy the constraints because the data results from a combination of parameters. For example, an interface following the shallow edge of the shaded region will not satisfy the constraints because the depth of the flat portion of the interface (*d1*) deepens as the location of the kink (*k*) moves northward. Layer velocities are similar to the average southern California crust velocity model [*Wald et al.*, 1995], but the upper mantle velocity is much faster.

The upper crust (above interface A) thickens gradually northward, reaching a thickness of 10-14 km beneath the Mojave Desert. In the Borderland, the top of the mid-crust occurs at 6-7 km depth, similar to the result of *ten Brink et al.* [2000], although the authors assumed the upper crust to be a steep velocity gradient. Our estimate of depth to the top of the mid-crustal layer beneath the Mojave Desert is slightly shallower than the average 15 km of *Hauksson* [2000], and suggests that our assumption of 5 km/s may be too slow to represent the continental rocks in the upper crust of the Mojave Desert.

Located between interfaces A and B, the mid-crust thickens from 8-10 km beneath the Borderland to as much as 18 km beneath the San Gabriel Mountains. The onset of mid-crustal thickening is more abrupt, as the interface between the mid and lower crust (interface B) transitions from horizontal to moderate dips of 7-11°. This transition occurs somewhere between the coastline and the San Gabriel Valley. *Hauksson* [2000] shows a similar increase in depth to the top of the lower crust, transitioning from nearly horizontal beneath the Los Angeles Basin, to greater than 25 km at the Sierra Madre Fault.

The lower crust beneath the Borderland is much thinner than the average southern California crust (16 km). The thickness of the lower crust ranges from 1-8 km, averaging 2.5 km for southern kink end members, and 6.2 km for northern kink end members. Our data constrains the Moho (interface C) to deepen abruptly, dramatically increasing the thickness of the lower crust as the Moho dips steeply northward (~30°). The transition from horizontal to steeply dipping occurs between the shallow offshore slope and the Los Angeles Basin. This range of possible locations is 30 km wide.

3.6 Discussion

3.6.1 Station Delays

Station delays for the San Gabriel Mountains show no correlation with receiver topography. While negative station delays and high upper crustal velocities have been previously noted for the San Gabriel Mountains [e.g., *Malin et al.*, 1981; *Hauksson and Haase*, 1997; *Pellerin and Christensen*, 1998], station delays have not been analyzed for relative differences along a profile perpendicular to the strike of the range. With a velocity of 5.0 km/s, one would expect the difference in station delay between the Sierra Madre fault (station #30, no pick data) and the highest station (# 43) to be at least 0.42 seconds just due to topography alone. This suggests that high velocity material is located in the upper crust beneath the mountains, such that the effect of additional ray path length to receiver is negated. Not only must high velocity material exist in the upper crust, it must also have velocities that are proportional to elevation. Higher velocities in the higher core of the range are reasonable if the middle of the range was uplifted and eroded faster than the flanks. A recent earthquake tomography study by *Hauksson* [2000] supports this theory, where cross section (d) shows velocities of 5.5-6.0 km/s at the surface in the central,

topographically high part of the San Gabriel Mountains, decreasing to 4.5-5.5 km/s at lower elevations on either side.

The receiver located near the coast has station delays comparable to those located in the Los Angeles Basin proper. This suggests that slow material of comparable amount to the Los Angeles basin may exist in the upper crust offshore of the Seal Beach coast. *Hauksson* [2000] shows slow velocities in the upper 4 km of the crust extending the Los Angeles Basin up to 7 km offshore (cross section d).

3.6.2 Location and Width of the Transition Zone

Our analysis shows that we can narrow the range of possible locations by making an assumption about the thickness of the crust in the Inner Borderland. We find that the location of the kink, *k*, in the flat-ramp models is linearly related to the depth of the flat, *d1*. The further south the kink is located, the shallower the flat portion of the interface. Thus, a thinner Borderland crust implies a transition zone further south, while a thicker Borderland crust moves the zone northward.

If we assume that the Moho depth is approximately 22 km in the Inner Borderland as modeled by other recent studies [*Zhu and Kanamori*, 2000; *Hauksson*, 2000], the northern kink end member models represent the location of the initiation of Moho dip. The northern kink end members place the dip initiation at 92-98 km (average 95 km), and hence beneath the southwestern Los Angeles Basin. The ray coverage from our data set allows us to trace this interface to 32-33 km depth (north kink models only) beneath the southern edge of the Puente Hills. This means that the transition zone from thin Inner Borderland crust (~22 km) to average southern California crust (~32 km) occurs over a horizontal distance of approximately 20 km.

Hauksson [2000] used the distribution of P-wave velocity in the lower crust to constrain the width of the transition zone to be 30-80 km wide in a region containing the Los Angeles Basin. Our results provide a more precise location and width of the transition zone. The width of our transition zone is similar to that of other locations along the central California coast, where the crust thickens over a distance of 20-30 km (between the Hosgri fault and the coastline), and not the 60-80 km previously believed [*Fuis*, 1998].

3.6.3 Velocity Model

Although our study shows that a range of models satisfy the data constraints, we present our "favored model" in Figure 3.13. We have chosen the flat-ramp configuration for all three interfaces because we believe this is the best representation of the transition of the crust from Borderland to continent. This model is a composite of two end member velocity models (#204 and #308) that contain a range in the location of the thickening of the upper and middle crust, due to the southern and northern limits of kink (k) locations for interfaces A and B. Regardless of kink locations in the crustal interfaces, the location of the kink in the Moho (interface C) occurs within a 4 km range, and is located beneath the southwestern Los Angeles basin.

The Borderland is believed to have an oceanic origin [*Mooney and Weaver*, 1989], but has a thicker crust than normal oceanic crust. Most of the additional thickness is contained within the upper and middle crust. The lower crust has a velocity (6.8 km/s) consistent with layer 3 of normal oceanic crustal structure (vp = 6.73±0.19 km/s, Christensen and Salisbury, 1975), but the thickness may or may not be consistent, depending on the location of the kink in phase B (thickness = 4.97±1.25 km, *Christensen and Salisbury*, 1975). *Ten Brink et al.* [2000] find no evidence for velocities greater than 6.5 km/s in the

Borderland beneath line 1, except for a limited high velocity ridge. This may result from the limited offsets (< 60 km) of the OBS data used in their study.

Although our modeled upper mantle velocity is faster than average southern California upper mantle (7.8 km/s, Wald et al., 1995), most of the upper mantle in our velocity model is beneath the Inner Borderland, a region whose deeper structure is not well known because of the lack of studies with adequate coverage at depth. Earthquake source tomographic studies are limited by sparse ray coverage in the offshore, especially at depth [*Hearn and Clayton*, 1986; *Sung and Jackson*, 1992; *Hauksson and Haase*, 1997; *Hauksson*, 2000]. The previous crustal seismic refraction study conducted in the Inner California Borderland prior to LARSE was published by Shor and Raitt in 1958. That study found a velocity of 8.2 km/s at a depth of 24 km beneath the Catalina Basin (Figure 3.1). *Christensen and Salisbury* [1975] find upper mantle velocities of 8.15 ± 0.31 km/s beneath normal oceanic crust older than 15 m.y. Inland of the crustal transition zone, upper mantle velocities should revert to the well established southern California average.

The Inner California Borderland seems to be modified and thickened oceanic crust, with the oceanic upper mantle intact beneath it. Pn is a strong, coherent, and continuous phase that is seen across the entire profile to source-receiver offsets of over 230 km. Therefore, the Moho (interface C) must be coherent and laterally continuous with only long wavelength variations, because short wavelength variations would diffract and attenuate the head wave phase energy. There is no reason to believe that the rest of the oceanic lithosphere beneath the upper mantle is absent. This suggests that a stalled fragment of subducted oceanic lithosphere remains beneath the Inner California Borderland.

During the late Oligocene, when the Pacific-Farallon spreading center was approaching the Farallon-North American trench, the subducting slab was very young and quite buoyant. The Farallon slab was breaking into fragments as it approached the trench. The young crust would have positive buoyancy relative to the underlying mantle, and if there were no slab pull to drag it beneath the continent, it could easily plate to the underside of the continent near the trench [*Bohannon and Parsons*, 1995]. While young slabs reheat at sublithospheric levels, young crust at shallow levels cools and strengthens rather than sinking [*Bohannon and Parsons*, 1995]. If a break occurred in the subducted slab inland from the trench, the fragments would remain underpinned to the continent and any slab gap would form inland from the trench, or occur at a deep enough level that it has little effect on the continental lithosphere above the slab gap [*Bohannon and Parsons*, 1995].

This fragment may be the southern portion of the partially subducted Monterey micro-plate imaged to the north, or a fragment of the north dipping Arguello micro-plate possibly seen south of the Morro fracture zone [*Nicholson et al.*, 1992; *Nicholson et al.*, 1994]. *Atwater and Stock* [1998] state that the Monterey micro-plate could extend further beneath southern California because their modeling only showed the minimum area of the fragment. The close proximity to the Transverse Ranges and the northward dip makes this material a prime candidate for the postulated oceanic lithosphere that is descending into the mantle beneath the Transverse Ranges [*Bird and Rosenstock*, 1984; *Humphreys*, 1995; *Atwater and Stock*, 1998].

Rifting and extension has been proposed for the Inner Borderland in the wake of the rotation of the Western Transverse Ranges [*Crouch and Suppe*, 1993; *Nicholson et al.*, 1994]. This is necessary to exhume the high grade, blueschist facies Catalina Schist from

a metamorphism depth of 10-15 km [*Crouch and Suppe*, 1993]. The schist exhumation seems problematic in light of the continuous and coherent nature of the Moho in the Inner Borderland and the proposed remnant slab fragment. However, the Santa Maria Basin is proposed to have undergone similar rifting and extension to the Inner Borderland [*Crouch and Suppe*, 1993], yet is underlain by the partially subducted Monterey micro-plate [*Nicholson et al.*, 1992]. Both the Inner Borderland and the Santa Maria basin underwent extension and modification in the upper to mid-crust without removal of the oceanic slab fragment beneath them.

3.7 Conclusions

The results we have presented provide new information on the mid to lower crustal and upper mantle structure in the transition zone from the Inner California Borderland to the on land adjacent continental region. We have created a composite velocity model that constrains the crustal thickness and location and width of the transition zone. Layer velocities are similar to the average southern California crust model, except for the higher upper mantle velocity beneath the Borderland. All layers within the Borderland crust are thinner than those of the onshore continental crust, with the lower crust being significantly thinner (< ½ the average thickness) in the Borderland. The time intercepts of Pn require the Moho to deepen significantly to the north. Our velocity model analysis requires the crustal thickness to increase dramatically over a relatively short distance (~20-25 km). The location of the transition zone is constrained to be between the offshore slope (~15 km offshore) and the Los Angeles Basin (~15 km onshore). Assuming a crustal thickness of 22 km for the Borderland further constrains the location of the transition zone to be in a 6 km wide region beneath the southwest Los Angeles Basin. The strong, coherent, and continu-

ous Pn phase indicates the Moho is coherent and laterally continuous with only long wavelength variations. The Inner California Borderland seems to be modified and thickened oceanic crust, with the oceanic upper mantle intact beneath it.

3.8. References

Atwater, T., Plate tectonic history of the northeast Pacific and western North America, in *The Geology of North America*, vol. N, *The eastern Pacific Ocean and Hawaii*, edited by E.L. Winterer and D.M. Hussong, pp. 21-72, Geol. Soc. of Am., Boulder, Colo., 1989.

Atwater, T., and J. Stock, Pacific-North America plate tectonics of the Neogene south-western United States - An update, *Int. Geol. Rev., 40*, 375-402, 1998.

Bird, P., and R.W. Rosenstock, Kinematics of present crust and mantle flow in southern California, *Geol. Soc. Am. Bull., 95*, 946-957, 1984.

Bohannon, R.G., and E. Geist, Upper crustal structure and Neogene tectonic development of the California continental borderland, *Geol. Soc. Am. Bull., 110*, 779-800, 1998.

Bohannon, R.G., and T. Parsons, Tectonic implications of post-30 Ma Pacific and North American relative plate motions, *Geol. Soc. Am. Bull., 107*, 937-959, 1995.

Brocher, T.M., R.W. Clayton, K. Klitgord, R. Bohannon, R. Sliter, J. McRaney, J. Gardner, and J. Keene, Multichannel seismic-reflection profiling on the R/V Ewing during the Los Angeles Region Seismic Experiment (LARSE), California, *U.S. Geol. Surv., Open File Rep. 95-228*, 1995.

Christensen, N.I., and M.H. Salisbury, Stucture and constitution of the lower oceanic crust, *Reviews of Geophysics and Space Physics, 13*, 57-83, 1975.

Couch, R.W., and R.P. Riddihough, The crustal structure of the western continental margin of North America, in *Geophysical Framework of the Continental United States*, edited by L.C. Pakiser and W.D. Mooney, *Geological Society of America Memoir 172*, pp. 103-128, 1989.

Crouch, J.K., and J. Suppe, Late Cenozoic evolution of the Los Angeles basin and inner California borderland: A model for core complex-like crustal extension, *Geol. Soc. Am. Bull., 105*, 1414-1434, 1993.

Ehlig, P.L., Origin and tectonic history of the basement terrane of the San Gabriel Mountains, central Transverse Ranges, in *The Geotectonic Development of California*, edited by W.G. Ernst, Rubey Volume 1, pp. 253-283, 1981.

Emery, K.O, General geology of the offshore area, southern California, *California Division of Mines and Geology Bulletin, 170*, 107-111, 1954.

Fuis, G.S., Western margin of North America - A synthesis of recent seismic transects, *Tectonophysics, 288*, 265- , 1998.

Fuis, G.S., D.A. Okaya, R.W. Clayton, W.J. Lutter, T. Ryberg, T.M. Brocher, T.L. Henyey, M.L. Benthien, P.M. Davis, J. Mori, R.D. Catchings, U.S. ten Brink, M.D. Kohler, K.D. Klitgord, and R.E. Bohannon, Images of crust beneath southern California will aid study of earthquakes and their effects, *EOS Transactions, 77*, pp. 173, 176, 1996.

Hauksson, E., Crustal structure and seismicity distribution adjacent to the Pacific and North American plate boundary in southern California, *J. Geophys. Res., 105*, 13875-13903, 2000.

Hauksson, E., and J.S. Haase, Three-dimensional Vp and Vp/Vs velocity models of the Los Angeles basin and central Transverse Ranges, California, *J. Geophys. Res., 102*, 5423-5453, 1997.

Hearn, T.M., and R.W. Clayton, Lateral velocity variations in southern California. II. Results for the lower crust from Pn waves, *Bull. Seism. Soc. Am., 76*, 495-509, 1986b.

Humphreys, E.D., Post-Laramide removal of the Farallon slab, western United States, *Geology, 23*, 987-990, 1995.

Kohler, M.D., P.M. Davis, H. Liu, M. Benthien, S. Gao, G. Fuis, R.W. Clayton, D. Okaya, and J. Mori, Data report for the 1993 Los Angeles Region Seismic Experiment (LARSE93), southern California: A passive study from Seal Beach northeast through the Mojave Desert, *USGS OFR 96-85*, 1996.

Kohler, M.D. and P.M. Davis, Crustal thickness variations in Southern California from Los Angeles Region Seismic Experiment (LARSE) passive phase teleseismic travel times, *Bull. Seism. Soc. Am., 87*, 1330-1344, 1997.

Luyendyk, B.P., M.J. Kamerling, and R. Terres, Geometric model for Neogene crustal rotations in southern California, *Geol. Soc. Am. Bull., 91*, 211-217, 1980.

Malin, P.E., M.H. Gillespie, P.C. Leary, and T.L. Henyey, Crustal structure near Palmdale, California, from borehole-determined ray parameters, *Bull. Seism. Soc. Am., 71*, 1783-1803, 1981.

Mooney, W.D., and C.S. Weaver, Regional crustal structure and tectonics of the Pacific Coastal States; California, Oregon, and Washington, in *Geophysical Framework of the Continental United States*, edited by L.C. Pakiser and W.D. Mooney, *Geol. So. Am. Memoir 172*, pp. 129-162, 1989.

Nicholson, C., C.C. Sorlien, and B.P. Luyendyk, Deep crustal structure and tectonics in the offshore southern Santa Maria Basin, California, *Geology, 20*, 239-242, 1992.

Nicholson, C., C.C. Sorlien, T. Atwater, J.C. Crowell, and B.P. Luyendyk, Microplate capture, rotation of the western Transverse Ranges, and initiation of the San Andreas transform as a low angle fault system, *Geology, 22*, 491-495, 1994.

Okaya, D., J. Bhowmik, G. Fuis, J. Murphy, M. Robertson, A. Chakaborty, M. Benthien, K. Hafner, and J. Norris, Report for airgun data aquired at onshore stations during

the Los Angeles Region Seismic Experiment (LARSE), Califonia, *USGS Open-File Report 96-297*, 1996.

Palmer, D., *Refraction Seismics: The lateral resolution of structure and seismic velocity*, Amsterdam: Geophysical Press, 269 p., 1986.

Pellerin, C.L.M., and N.I. Christensen, Interpretation of crustal seismic velocities in the San Gabriel-Mojave region, southern California, *Tectonophysics*, *286*, 253-271, 1998.

Richards-Dinger, K.B., and P.M. Shearer, Estimating crustal thickness in southern California by stacking Pmp arrivals, *J. Geophys. Res.*, *102*, 15,211-15,224, 1997.

Shepard, F.P., and K.O. Emery, Submarine topography off the southern California coast-Canyons and tectonic interpretation, *Geol. Soc. Am. Spec. Paper 31*, 171 p., 1941.

Shor Jr., G.G., and R.W. Raitt, Seismic studies in the southern California Continental Borderland: *Congresso Geologico Interncional, XXa Seccion*, 1956, Mexico, Seccion IV, Segundo Tomo, 243-259, 1958.

Sung, L., and D.D. Jackson, Crustal and uppermost mantle structure under southern California, *Bull. Seism. Soc. Am.*, *82*, 934-961, 1992.

ten Brink, U.S., R.M. Drury, G.K. Miller, T. Brocher, and D. Okaya, Los Angeles Region Seismic Experiment (LARSE), California off-shore seismic refraction data, *USGS Open-File Report 96-27*, 29 p., 1996.

ten Brink, U.S., J. Zhang, T.M. Brocher, D.A. Okaya, K.D. Klitgord, and G.S. Fuis, Geophysical evidence for the evolution of the California Inner Continental Borderland as a metamorphic core complex, *J. Geophys. Res.*, *105*, 5835-5857, 2000.

Wald, L.A., L.K. Hutton, and D.D. Given, The Southern California Network Bulletin: 1990-1993 summary, *Seis. Res. Lett.*, *66*, 9-19, 1995.

Wessel, P., and W.H.F. Smith, Free software helps map and display data, *EOS Trans. AGU, 72*, pp. 441, 445-446, 1991.

Wright, T.L., Structural geology and tectonic evolution of the Los Angeles basin, California, in *Active Margin Basins*, edited by K. T. Biddle, *Am. Ass. Petro. Geol. Memoir 52*, 35-134, 1991.

Yerkes, R.F., T.H. McCullough, J.E. Schoellhamer, and J.G. Vedder, Geology of the Los Angeles Basin, California - An introduction: *U.S. Geological Survey Professional Paper 420-A*, 57 p., 1965.

Yilmaz, O., *Seismic Data Processing*, Society of Exploration Geophysicists, Tulsa, 1987.

Zelt, C.A., and R.B. Smith, Seismic traveltime inversion for 2-D crustal velocity structure, *Geophysical Journal International, 108*, 16-34, 1992.

Zhu, L., and H. Kanamori, Moho depth variations in southern California from teleseismic receiver functions, *J. Geophys. Res., 105*, 2969-2980, 2000.

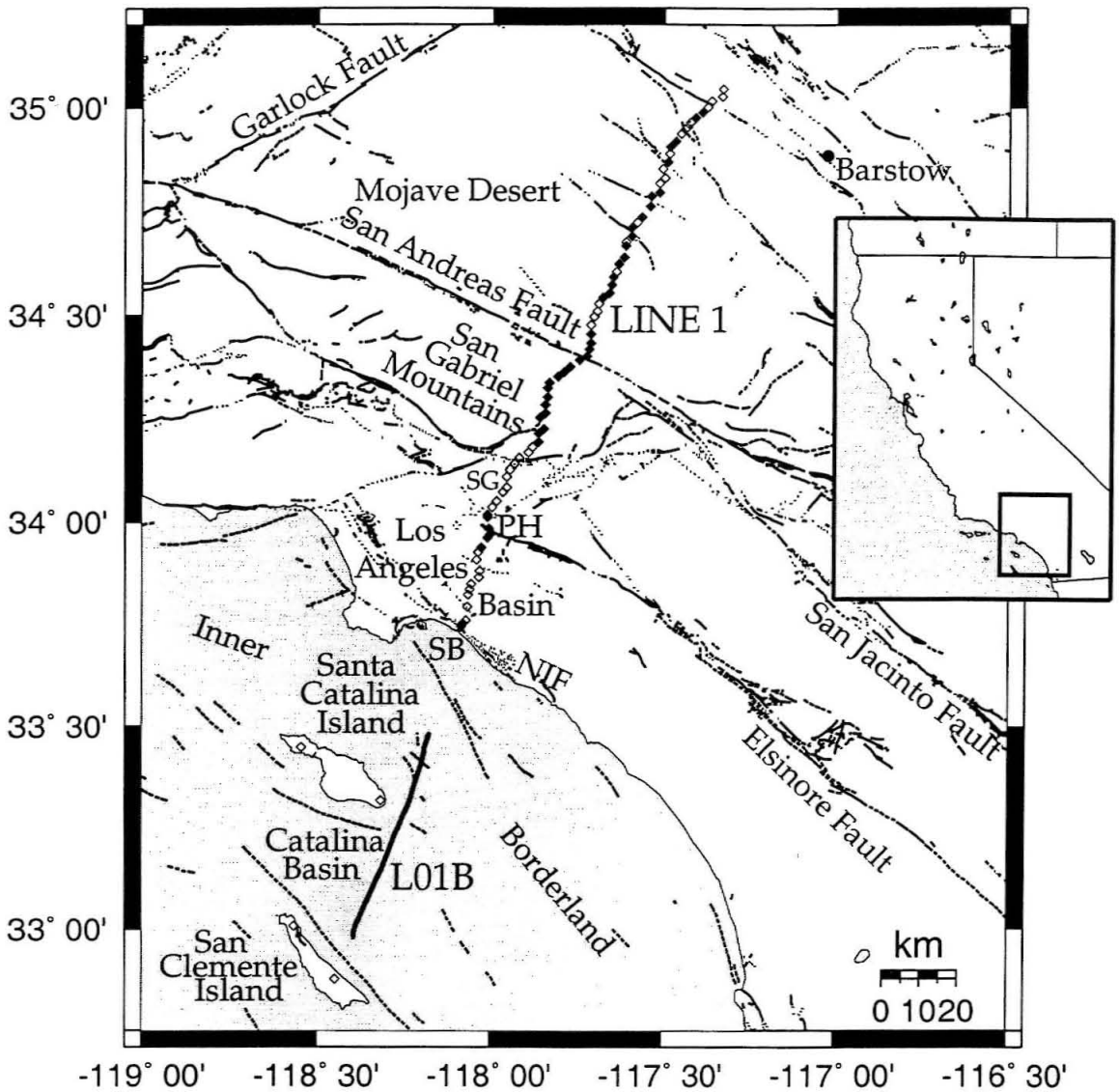

Figure 3.1 Location of LARSE experiment. Ship track L01B (airgun positions) are marked with thick lines. Receivers are marked with diamonds, with filled diamonds showing stations used in this analysis. Solid, dashed and dotted lines represent faults. NIF - Newport-Inglewood Fault; PH - Puente Hills; SB - Seal Beach; SG - San Gabriel Valley.

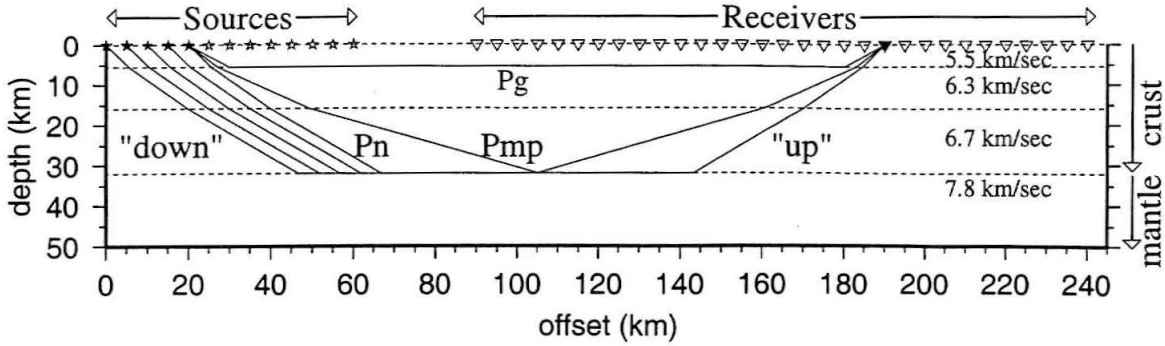

Figure 3.2 Source receiver geometry in cross section. There are gaps at the surface, but through-going rays at depth. The limited range covered and the gaps in coverage restrict the analysis to simple layered models. Velocities and depths shown are for the average southern California crust model [*Wald et al.*, 1995].

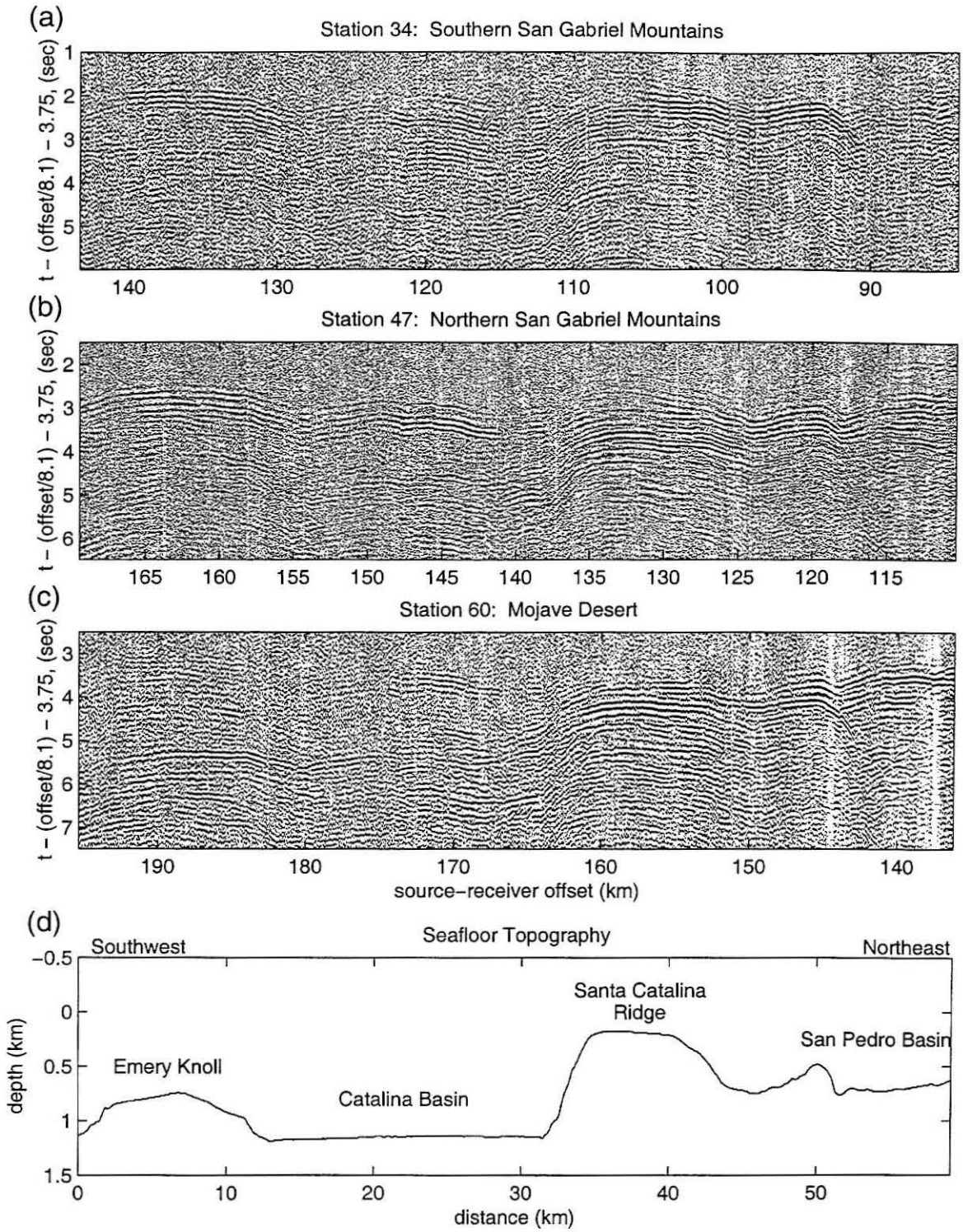

Figure 3.3 (a-c) Three receiver gathers at different offset ranges showing the same shape lateral time variations. (d) Seafloor topography beneath the ship track. Note there is greater than 1 km of relief in the seafloor.

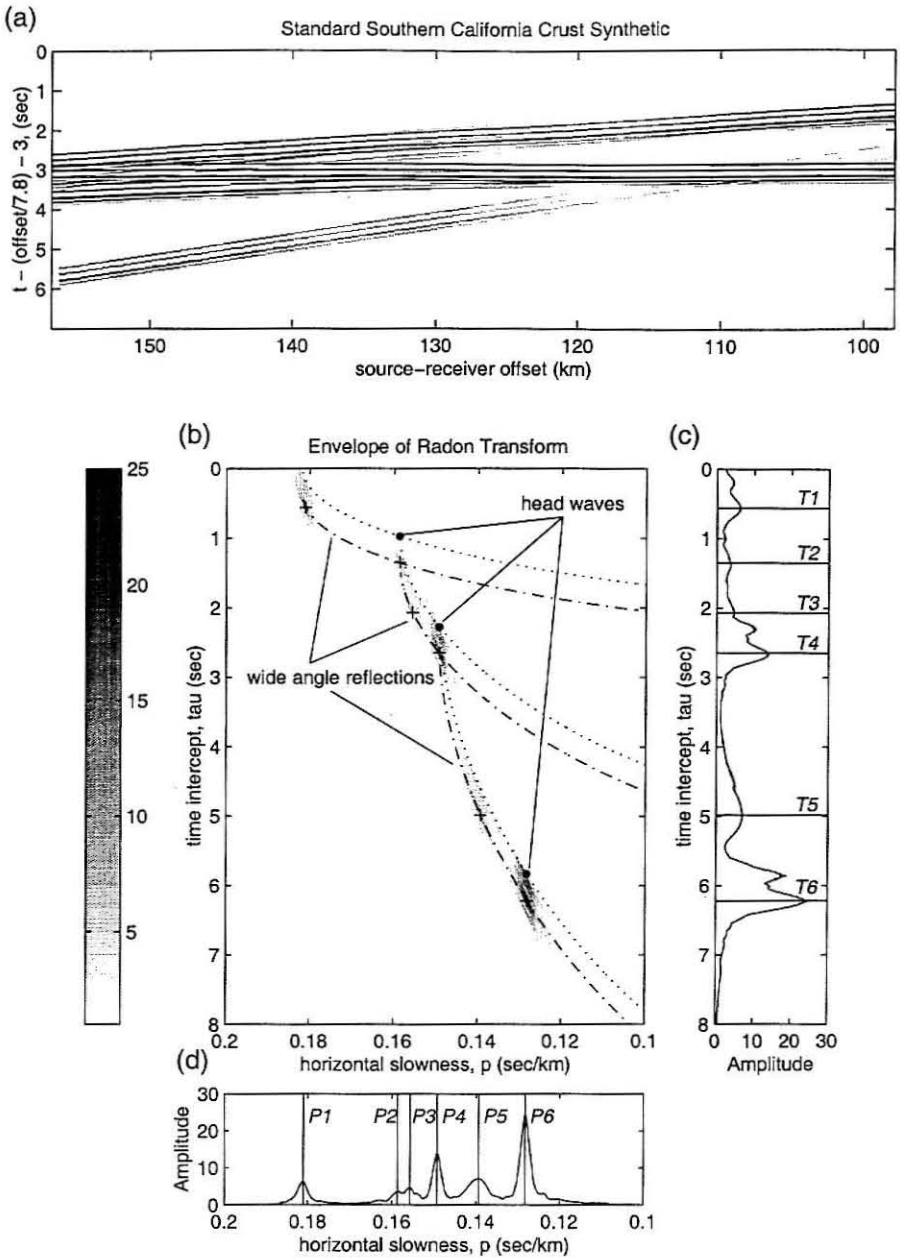

Figure 3.4 Synthetic example to demonstrate the picking process. (a) Reduced time section based upon the average southern California crust model [*Wald et al.*, 1995]. Convolved with representative waveform to simulate the multiple reverberations found in the LARSE data. (b) Envelope of the Radon transform. Dotted line represents theoretical stacked ellipses of the Radon transform of full offset impulsive arrival data. The dashed line shows the theoretical ellipses delayed by 0.38 s, representing the delay in the waveform from onset to maximum amplitude. (c) Maximum amplitude of each row (time intercept, τ, axis). Peak picks corresponding to the peak picks of 4d, labeled T1-T6. (d) Maximum amplitude of each column (horizontal slowness, p, axis). Peak picks labeled P1-P6, represent the apparent horizontal slowness of the three head wave and three reflection phases.

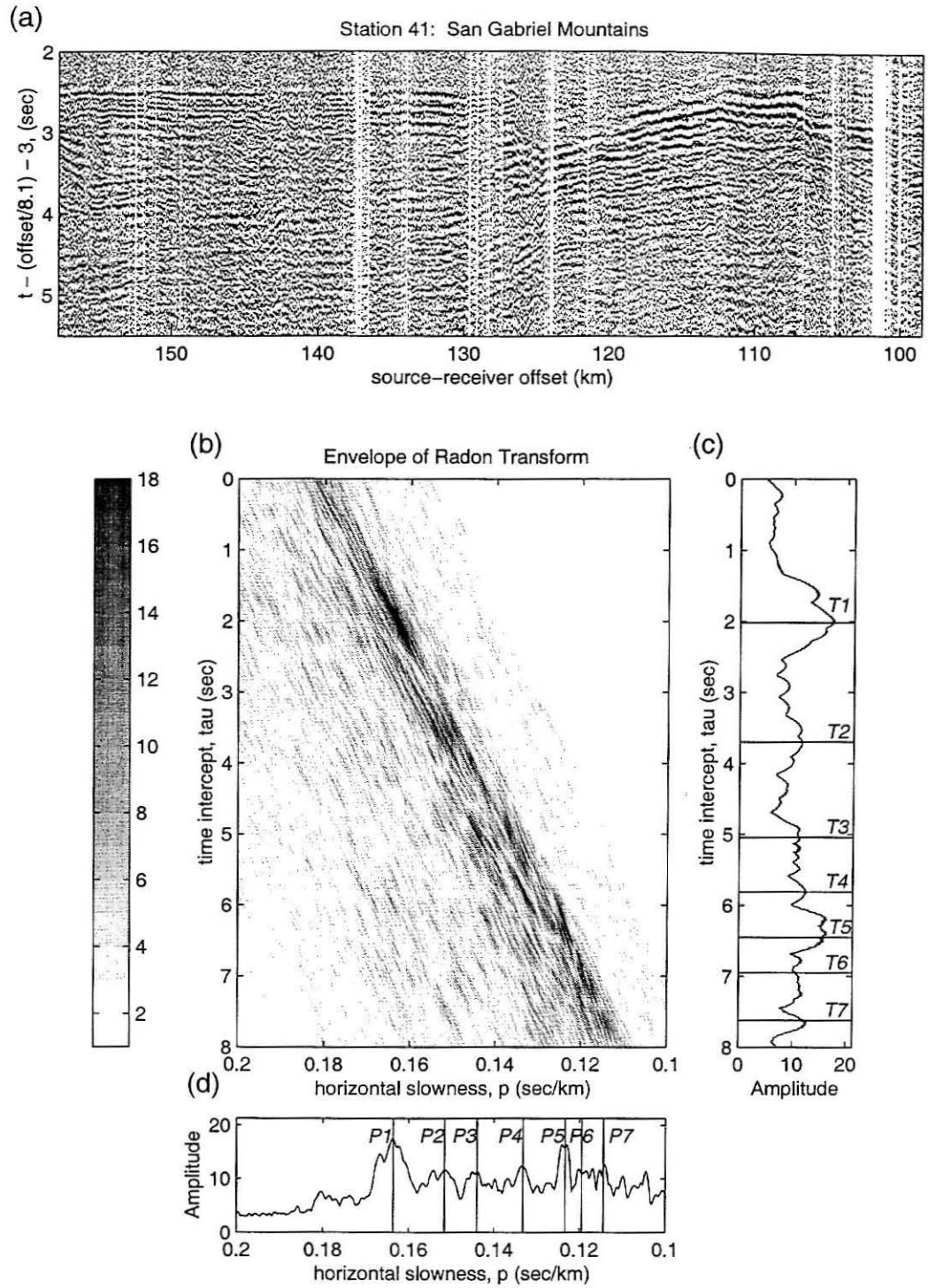

Figure 3.5 **Picking process demonstrated on Station 41 data. (a) Reduced time section for station 41, located in the San Gabriel Mountains. Data has been bandpass filtered, deconvolved, and corrected for near-source effects. (b) Envelope of the Radon transform of the data. (c) Maximum amplitude of each row (τ). The seven τ picks shown (T1-T7) correspond to the seven p picks of 5d (P1-P7 respectively). (d) Maximum amplitude of each column (p). Seven p picks correspond to τ picks in 5c.**

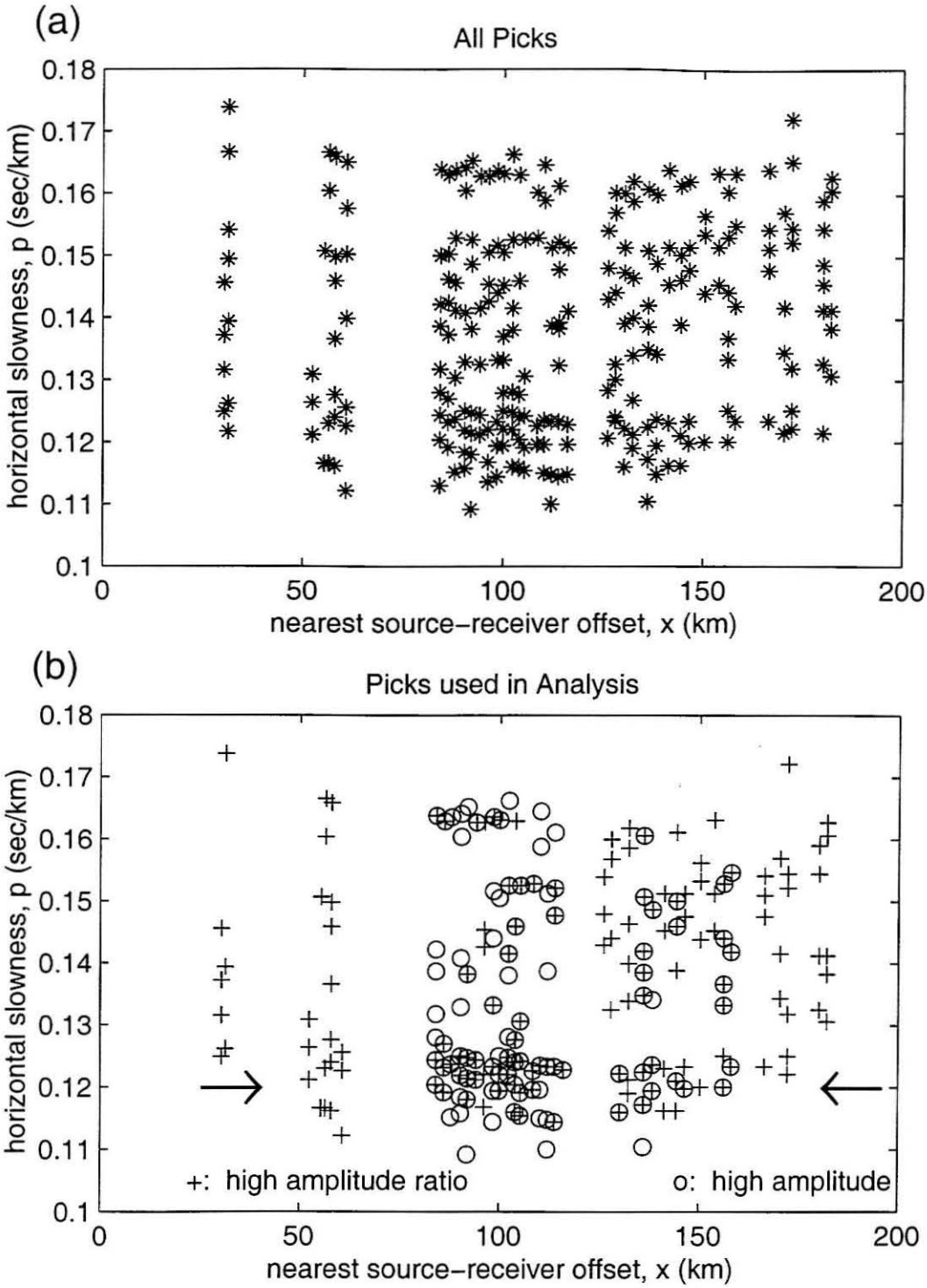

Figure 3.6 (a) 251 *p* picks from all stations, plotted against the nearest source-receiver offset of each station. (b) 187 "good" *p* picks. Picks with high ratio of peak amplitude to the maximum amplitude of the Radon transform envelope plotted as pluses. Picks with high amplitudes plotted as circles. Some peaks have both high pick amplitude and high amplitude ratio.

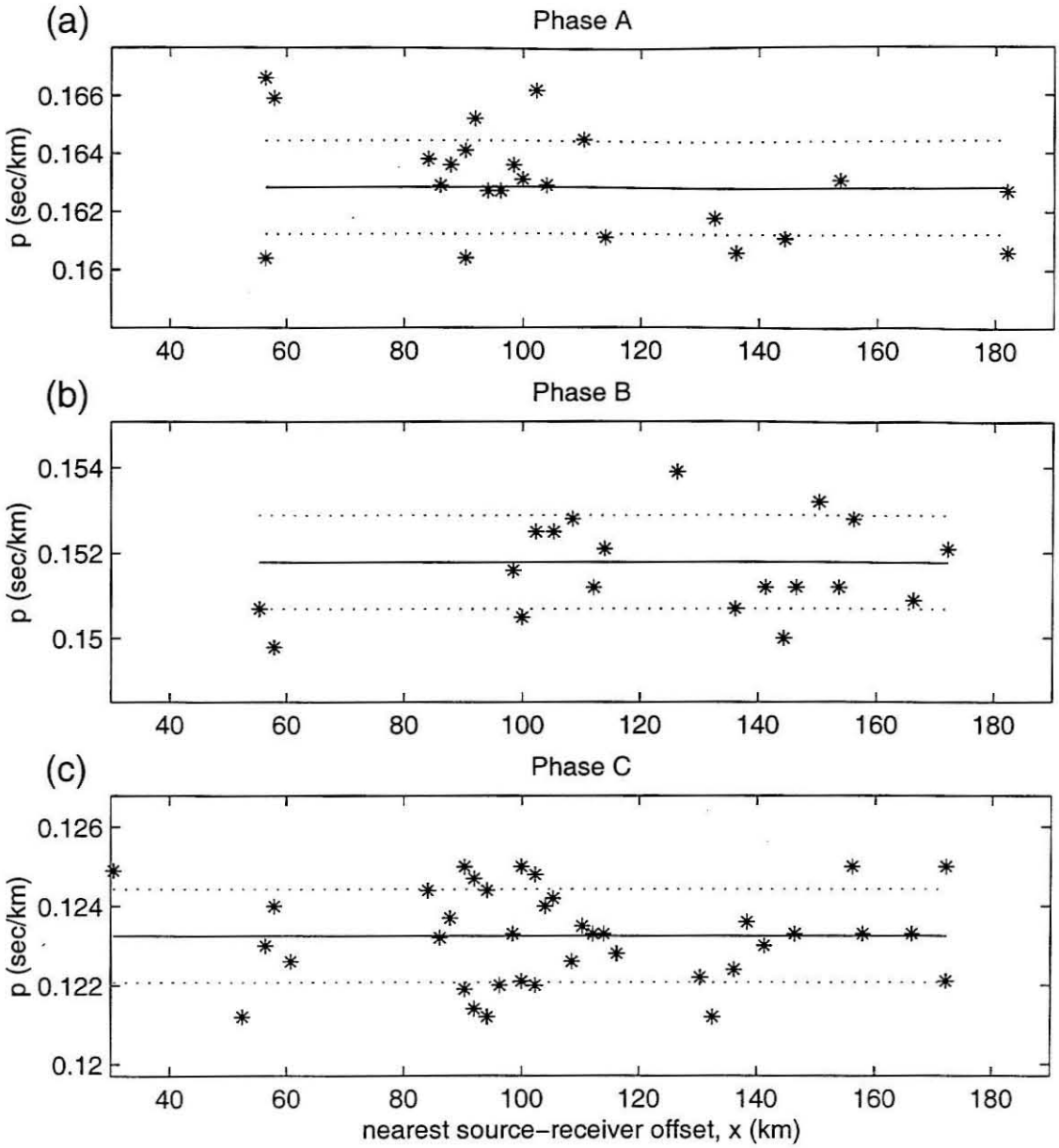

Figure 3.7 (a)-(c): **Horizontal slowness (p) picks for the three phases identified. Mean p of each phase marked by solid line with the uncertainty shown as dotted lines.**

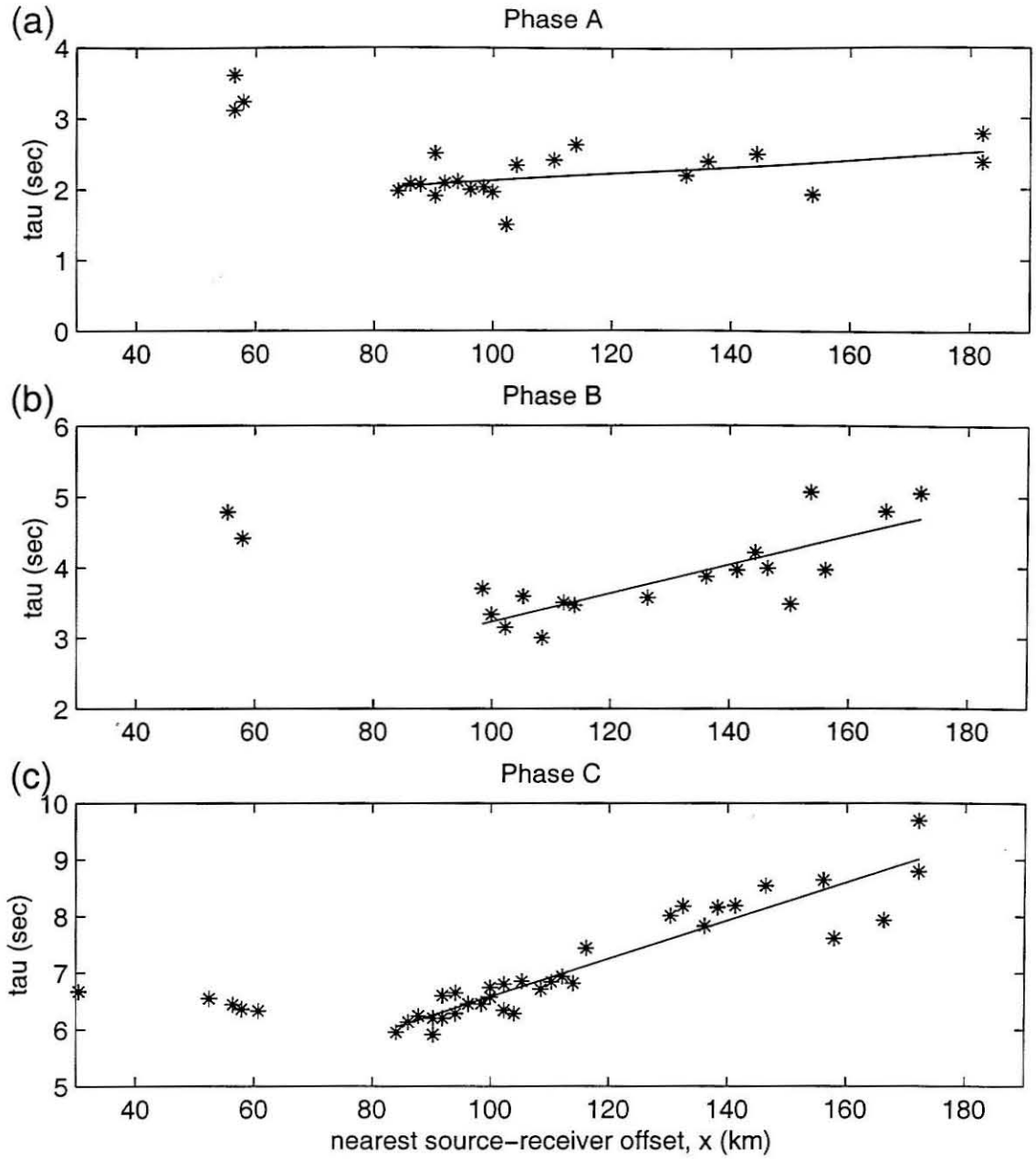

Figure 3.8 **(a)-(c): Time intercept (τ) picks for the three phases identified. Solid lines marks the best fit line for the San Gabriel Mountain and Mojave Desert stations (x > 80 km). Coastal and basin stations are not used because of the inconsistent delays between different phases.**

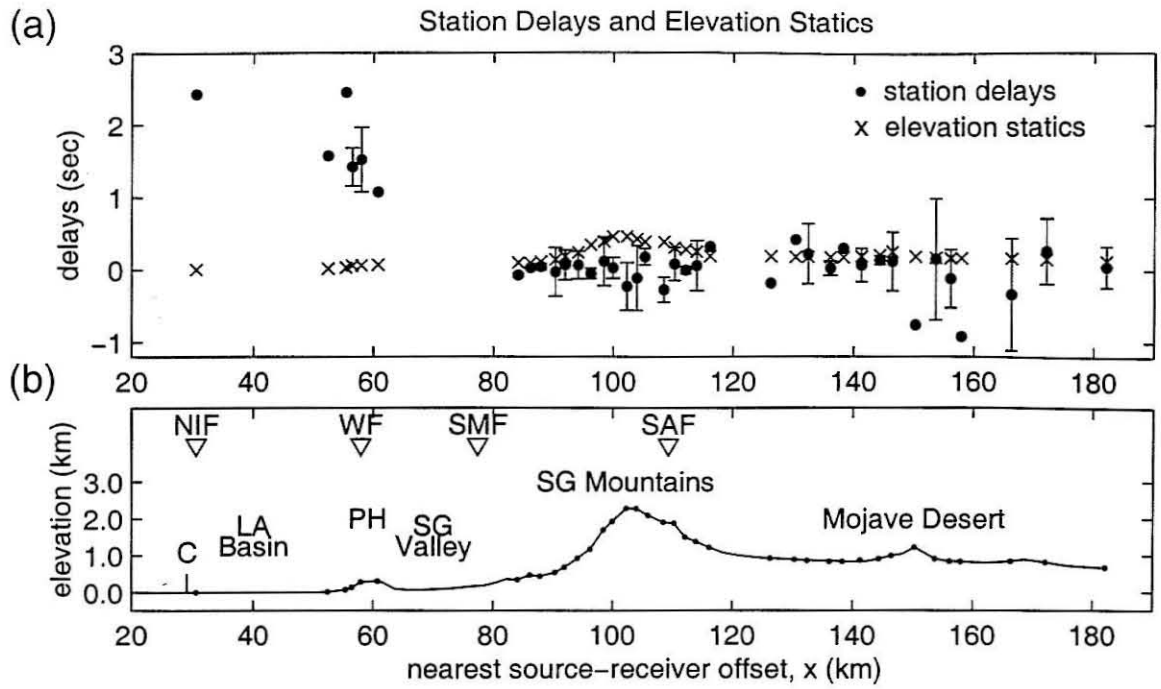

Figure 3.9 Station delays and elevation statics. (a) Filled circles represent average station delays, with error bars at stations with more than one phase picked. Estimated elevation statics are marked with an x. Note the lack of correlation of elevation statics and station delays for the San Gabriel Mountains (80 < x < 120 km), where some of the stations at the highest elevations have the largest negative delays. (b) Topography. Dots on surface represent receivers. C- coast; LA Basin – Los Angeles Basin; NIF – Newport-Inglewood Fault; PH – Puente Hills; SAF – San Andreas Fault; SG Mountains – San Gabriel Mountains; SG Valley – San Gabriel Valley; SMF – Sierra Madre Fault; WF – Whittier Fault.

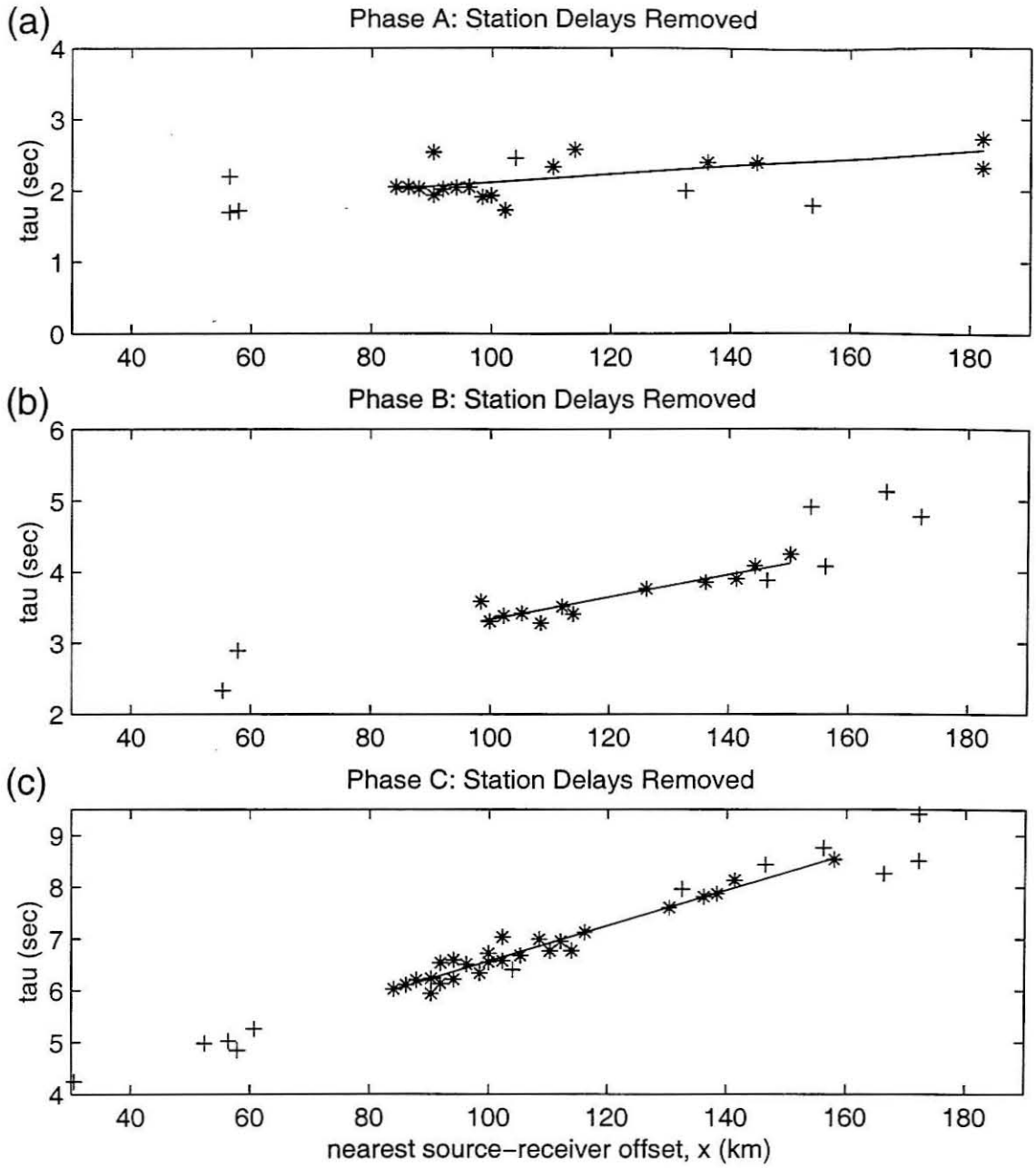

Figure 3.10 (a)-(c): Time intercepts after station delays removed for the three identified phases. Solid lines marks the best fit line for the San Gabriel Mountain and Mojave Desert stations (x > 80 km). Receivers with large uncertainties in average station delay (> 0.40 s) are not used in the fit and are marked by pluses.

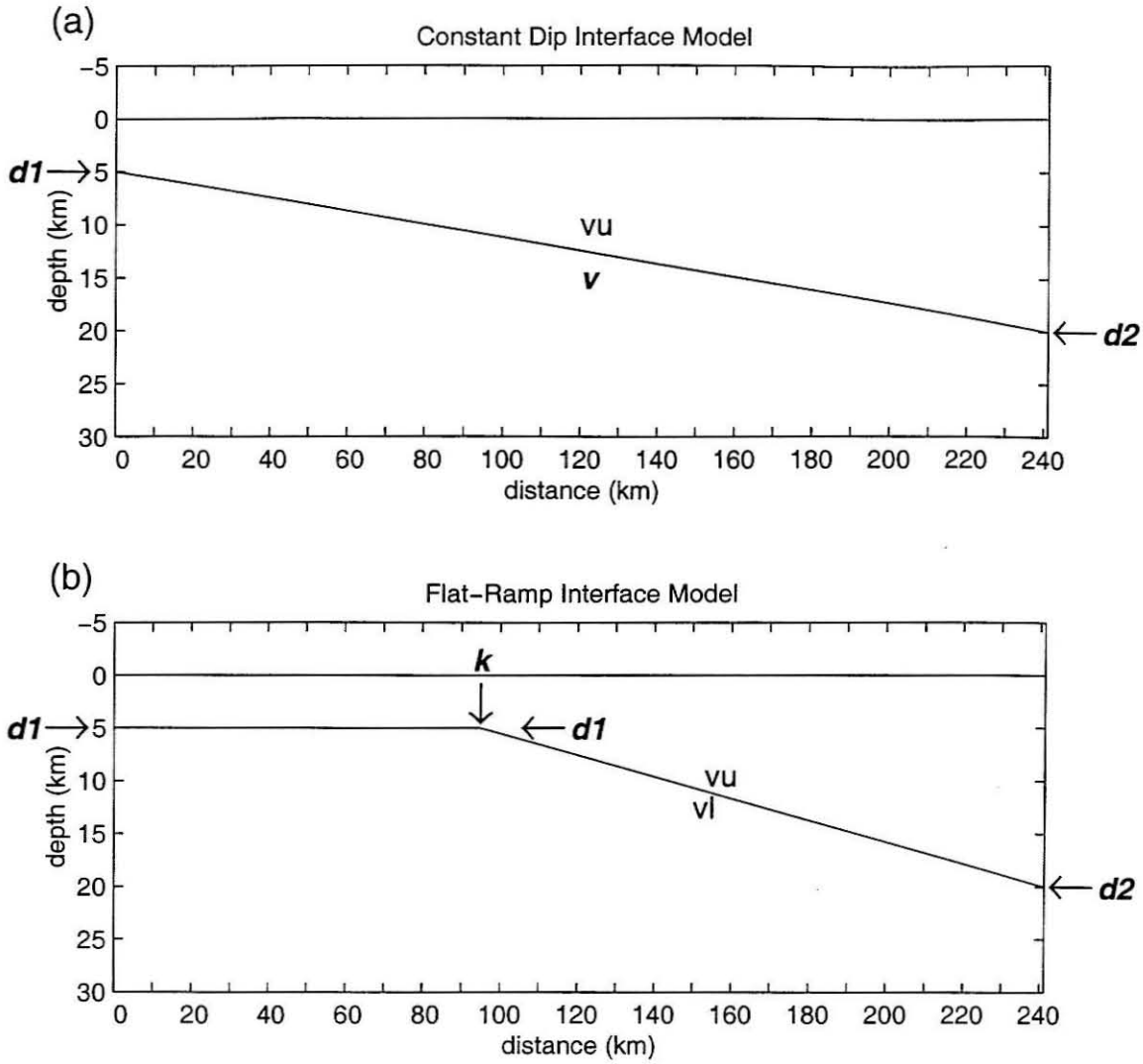

Figure 3.11 **Two types of interface models are defined as structural end members. (a) Constant dip interface model. Interface depth at left (south) side of model, *d1*. Depth at right (north) side of model, *d2*. Lower layer velocity, *v*. Upper layer velocity, vu is fixed in the modeling process. (b) Flat-ramp interface model. Depth of flat portion of interface and depth of interface at left (south) side of model, *d1*. Interface depth at right (north) side of model, *d2*. Location of kink, *k*, marks the transition from flat to dipping interface. Upper and lower layer velocities, vu and vl respectively, are fixed in the modeling process. Lower layer velocity is the inverse of the horizontal slowness of the phase, vl = 1/*p*.**

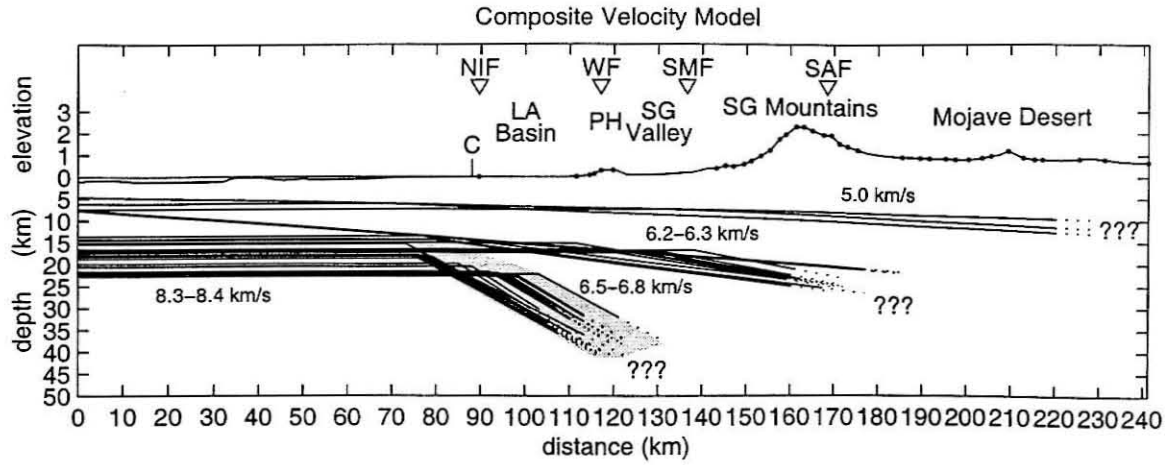

Figure 3.12 Composite velocity model. Composed of 39 end member interfaces with reasonable model errors. Surface topography exaggerated 5X. Seafloor topography not exaggerated. Dots represent receivers used in the velocity modeling for interface C. Interface A, B, and C end members are represented by medium gray, light gray, and black lines, respectively. Question marks indicate the extent of ray coverage for the three interfaces. Although some B and C interface lines intersect in this plot, the respective interface structure for individual velocity models do not. Shaded region outlines the region of crust where the Moho is located. Velocities listed for each layer represent the range of velocities found in the 39 velocity models with reasonable model errors. Dots on surface represent receivers. C- coast; LA Basin – Los Angeles Basin; NIF – Newport-Inglewood Fault; PH – Puente Hills; SAF – San Andreas Fault; SG Mountains – San Gabriel Mountains; SG Valley – San Gabriel Valley; SMF – Sierra Madre Fault; WF – Whittier Fault.

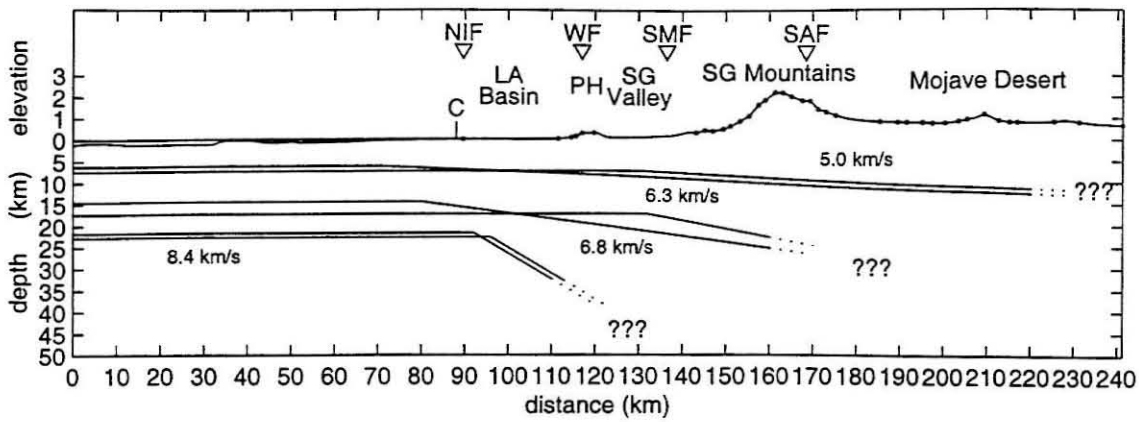

Figure 3.13 "Favored velocity model." Model is actually composite of two end member velocity models (#204 and #308) that contain the range in location of thickening of upper and middle crust. Moho (interface C) kink location occurs within a 4 km range, regardless of kink locations in crustal interfaces. Surface topography exaggerated 5X. Seafloor topography not exaggerated. Dots on surface represent receivers. C- coast; LA Basin – Los Angeles Basin; NIF – Newport-Inglewood Fault; PH – Puente Hills; SAF – San Andreas Fault; SG Mountains – San Gabriel Mountains; SG Valley – San Gabriel Valley; SMF – Sierra Madre Fault; WF – Whittier Fault.

Interface Model #	Type	*d1* (km)	*d2* (km)	*k* (km)	*v* (km/s)	Interface Model Error, E (s)	Interface A Model Used	Interface B Model Used
1	CD	4.6	9.8		6.2	0.238		
2	FR	7.4	12.2	131	6.3	0.238		
3	FR	6.2	13.3	70	6.3	0.238		
11	FR	13.6	33.7	80	6.7	0.150	1	
12	FR	15.1	36.9	111	6.7	0.151	1	
13	FR	16.8	36.4	138	6.7	0.147	1	
14	CD	7.6	26.3		6.5	0.152	1	
21	FR	14.5	35.8	80	6.8	0.149	2	
22	FR	16.6	36.8	116	6.8	0.149	2	
23	FR	17.2	37.5	128	6.8	0.146	2	
24	CD	7.7	26.3		6.6	0.152	2	
31	FR	14.3	34.9	80	6.8	0.146	3	
32	FR	17.0	36.5	123	6.8	0.150	3	
33	FR	17.3	37.5	132	6.8	0.145	3	
34	CD	7.5	26.1		6.6	0.152	3	
101	FR	15.3	101.9	73	8.3	0.159	1	14
102	FR	22.2	96.8	103	8.3	0.162	1	14
103	FR	18.2	115.6	78	8.3	0.157	1	11
104	FR	22.0	114.7	94	8.3	0.161	1	11
105	FR	18.2	106.9	75	8.3	0.158	1	12
106	FR	22.3	106.8	94	8.3	0.165	1	12
107	FR	19.9	117.5	85	8.3	0.162	1	13
108	FR	20.5	118.6	88	8.3	0.162	1	13
109	CD	13.6	74.5		7.3	1.682	1	11
110	CD	15.1	72.1		7.3	1.729	1	12
111	CD	16.8	75.3		7.4	2.164	1	13
112	CD	7.6	62.6		7.2	1.025	1	14
201	FR	17.1	109.6	76	8.3	0.159	2	24
202	FR	22.7	107.7	98	8.3	0.164	2	24
203	FR	18.7	109.4	79	8.4	0.163	2	21
204	FR	22.7	109.3	96	8.4	0.164	2	21
205	FR	18.2	107.3	76	8.4	0.158	2	22
206	FR	22.6	106.1	95	8.4	0.164	2	22
207	FR	18.0	109.0	75	8.4	0.163	2	23
208	FR	22.2	109.2	93	8.4	0.164	2	23
209	CD	14.8	76.1		7.4	1.982	2	21
210	CD	16.6	74.1		7.4	1.954	2	22
211	CD	16.6	74.5		7.4	1.980	2	23
212	CD	7.7	63.0		7.3	0.972	2	24
301	FR	17.1	106.8	76	8.3	0.159	3	34
302	FR	22.3	109.0	98	8.3	0.165	3	34
303	FR	18.2	109.4	79	8.4	0.163	3	31
304	FR	22.2	113.4	96	8.4	0.162	3	31
305	FR	17.9	109.5	76	8.4	0.161	3	32
306	FR	22.2	108.5	95	8.4	0.165	3	32
307	FR	18.0	113.4	77	8.4	0.161	3	33
308	FR	21.7	110.4	92	8.4	0.164	3	33
309	CD	14.8	75.4		7.4	2.005	3	31
310	CD	17.0	74.7		7.4	2.013	3	32
311	CD	17.3	75.7		7.4	2.098	3	33
312	CD	7.5	64.7		7.3	0.979	3	34

Table 3.1 Composite velocity model interfaces. Each interface must be considered individually to determine range of possible interface models that fit data constraint. All possible configurations for shallower interfaces must be considered when modeling deeper phases. Three possible configurations for interface A. Four possible configurations for interface B combined with three for interface A results in 12 interface B models. Thirty-six interface C models result from 12 interface B models and 3 interface C configurations. Interface model types: CD for constant dip and FR for flat-ramp. Interface depths at left (south) and right (north) sides of model region, *d1* and *d2*. *k* is location of kink in flat-ramp models (not a parameter for constant dip models). Lower layer velocity, *v*, is a variable parameter for constant dip interface models, but is fixed by the inverse of phase horizontal slowness (1/*p*) for flat-ramp interface models. Interface model error E, as defined in equation (3.4). A and B interface model columns, list the interface A and B model numbers used when modeling deeper interfaces.

CHAPTER 4

The Static Stress Change Triggering Model: Constraints From Two Southern California Aftershock Sequences

Hardebeck, J.L., J.J. Nazareth, and E. Hauksson, *Journal of Geophysical Research*, **103**, 24,427-24,437, 1998.

4.1 Abstract

Static stress change has been proposed as a mechanism of earthquake triggering. We quantitatively evaluate this model for the apparent triggering of aftershocks by the 1992 M_w 7.3 Landers and 1994 M_w 6.7 Northridge earthquakes. Specifically, we test whether the fraction of aftershocks consistent with static stress change triggering is greater than the fraction of random events which would appear consistent by chance. Although static stress changes appear useful in explaining the triggering of some aftershocks, the model's capability to explain aftershock occurrence varies significantly between sequences. The model works well for Landers aftershocks. Approximately 85% of events between 5 and 75 km distance from the mainshock fault plane are consistent with static stress change triggering, compared to ~50% of random events. The minimum distance is probably controlled by limitations of the modeling, while the maximum distance may be because static stress changes of < 0.01 MPa trigger too few events to be detected. The static stress change triggering model, however, cannot explain the first month of the Northridge aftershock sequence significantly better than it explains a set of random

events. The difference between the Landers and Northridge sequences may result from differences in fault strength, with static stress changes being a more significant fraction of the failure stress of weak Landers-area faults. Tectonic regime, regional stress levels, and fault strength may need to be incorporated into the static stress change triggering model before it can be used reliably for seismic hazard assessment.

4.2 Introduction

Static stress change triggering of earthquakes has been proposed as a model for evaluating short-term earthquake hazards. It is one of a number of models relating to the apparent triggering of earthquakes, "triggering" meaning that one earthquake causes another earthquake which would not have otherwise occurred at that time. The idea is that static stress change due to an earthquake can move another fault toward failure stress, advancing the time of the next earthquake on that fault. Previous work has used static stress theory to identify faults which may have been moved closer to or farther from failure. For example, the effects of the 1989 Loma Prieta and 1992 Landers earthquakes on the San Andreas fault and other major faults in California have been studied [e.g., *Reasenberg and Simpson*, 1992; *Harris and Simpson*, 1992; *Jaumé and Sykes*, 1992; *Stein et al.*, 1992; *King et al.*, 1994; *Stein et al.*, 1994]. Static stress triggering has also been used to explain sequences of earthquakes in a region: for instance, the Eastern California Shear Zone [e.g., *Stein et al.*, 1992; *King et al.*, 1994]; the Los Angeles area [e.g., *Stein et al.*, 1994]; southern California [e.g., *Deng and Sykes*, 1997]; and the San Francisco bay area [e.g., *Jaumé and Sykes*, 1996].

There have been only a few quantitative studies of how consistent the locations and orientations of apparently triggered events are with modeled static stress changes.

Harris et al. [1994] and *Simpson et al.* [1994] computed the percentage of aftershocks of the 1994 Northridge earthquake consistent with static stress change triggering. *Beroza and Zoback* [1993] and *Kilb et al.* [1997] studied whether static stress changes could explain the diverse mechanisms of the 1989 Loma Prieta aftershock sequence. *Harris et al.* [1995] investigated the static stress change triggering of $M \geq 5$ events in southern California by each other, but the data were limited to only 16 pairs.

In this paper, we test the static stress change triggering model using the aftershock sequences of the 1992 Landers and 1994 Northridge earthquakes. Each sequence includes tens of thousands of recorded events [e.g., *Hauksson et al.*, 1993, 1995], providing sufficient data quantity for a robust quantitative analysis.

Our primary goal is to determine how well modeled static stress changes explain the apparent triggering of aftershocks by a mainshock. Specifically, we test if the fraction of aftershocks consistent with triggering by mainshock-induced static stress changes is larger than the fraction of random events (with appropriate probability distributions) which would appear consistent by chance. If it is statistically significantly greater, static stress change is a viable model for explaining aftershock triggering; otherwise, it is not.

A secondary goal is to determine whether the usefulness of the static stress change triggering model is dependent on the size of the stress change, distance from the fault plane, event magnitude, or elapsed time since the mainshock. This may establish some guidelines as to when and where static stress change triggering is an appropriate model for use in seismic hazard assessment.

4.3 Data

We analyze data from the 1992 Landers and 1994 Northridge earthquake sequences (Figure 4.1). These two southern California sequences were recorded by the Southern California Seismic Network (SCSN) and portable stations installed after the mainshocks. The Landers earthquake of June 28, 1992, a M_w 7.3 strike-slip event, ruptured a cumulative length of 85 km along five faults. The event occurred in the Eastern California Shear Zone, a 80 km wide and 400 km long region of right-lateral strike-slip faults, east of the San Andreas fault, thought to be taking up ~8 mm/yr of the 48 mm/yr Pacific-North America relative plate motion. The Landers sequence is discussed in detail by *Hauksson et al.* [1993].

The January 17, 1994, M_w 6.7 Northridge earthquake occurred on a 20 km length of a previously unrecognized blind thrust beneath the western San Fernando Valley. The earthquake occurred in a region of north-south contractional deformation related to the uplift of the Transverse Ranges at a constraining bend in the San Andreas fault. The Northridge sequence is described by *Hauksson et al.* [1995].

We determine locations and focal mechanisms for $M \geq 2.0$ recorded events in a box around each mainshock, including events not strictly considered aftershocks. Arrival time data from selected aftershocks recorded by the SCSN are used with the VELEST code *Kissling et al.*, [1994] to jointly determine hypocenters and a refined velocity model. Hypocenters for the remaining events are then determined using HYPOINVERSE [*Klein*, 1985], and mechanisms found using the codes of *Reasenberg and Oppenheimer* [1985]. Only events with focal mechanism parameter uncertainties less than 30° are used.

4.4 *Method*

We model the Landers and Northridge mainshocks as dislocations in an elastic half-space and compute the resulting static stress changes. The Coulomb stress changes on aftershock nodal planes are determined, and the Coulomb index (the percent of events consistent with static stress change triggering) is found. The Coulomb index for the first month of each observed sequence is compared to the Coulomb indices of 500 random synthetic sequences (chosen from appropriate probability distributions) to test the null hypothesis that the Coulomb index of the observed sequence is no greater than the Coulomb indices of the synthetic sequences. This test is performed for various subsets of the data.

4.4.1 Coulomb Failure

The Coulomb failure criterion is commonly used to quantify the effect of static stress change on a plane [e.g., *Reasenberg and Simpson*, 1992; *Harris and Simpson*, 1992; *Jaumé and Sykes,* 1992; *Stein et al.*, 1994; *King et al.*, 1994]. We compute only the incremental stress added by the mainshock because we are testing whether the mainshock-induced static stress changes could have triggered the aftershocks. The importance of the background stress state will be addressed in the comparison of results from the two aftershock sequences.

The change in Coulomb stress, ΔCS, on a plane is

$$\Delta CS = \Delta\tau + \mu'\Delta\sigma \qquad \text{(EQ 4.1)}$$

where $\Delta\tau$ is the change in shear stress in the direction of slip on the plane, $\Delta\sigma$ is the change in normal stress (tension positive), and μ is the effective coefficient of friction.

We find the Coulomb stress change using the nodal planes and slip directions of individual aftershocks (following *Harris et al.* [1994] and *Simpson et al.* [1994]) because

it is important to test whether aftershock slip occurs in a direction consistent with the static stress change model. We feel that using representative planes (such as optimally oriented planes) is not as accurate, considering the diversity of aftershock mechanisms that can occur in close proximity (e.g., Figure 4.2 and Figure 4.3). Determining the stress changes on representative planes causes a loss of information by reducing the static stress change tensor to a scalar and not incorporating the aftershock focal mechanisms.

The effective coefficient of friction, μ, accounts for the effect of fluid pressure on the failure plane. When $\mu = \mu$ (the coefficient of friction for dry rock), the pore pressure has no effect on the normal stress. At the other extreme, when $\mu = 0$, the rock is so saturated that the pore pressure cancels the effect of the normal stress on the plane. Laboratory experiments on rocks typically find values for μ of around 0.6 to 0.85 [e.g., *Byerlee*, 1978], and values of μ between 0 and 0.75 are considered plausible [e.g., *King et al.*, 1994]. Low values of μ (0 to 0.4) are typical in the stress change literature [e.g., *Reasenberg and Simpson*, 1992; *King et al.*, 1994; *Kagan*, 1994]. In this paper, we try a range of values for μ between 0 and 0.8.

4.4.2 Technique

We model the mainshocks as planar dislocations in an elastic half-space. The Landers earthquake is modeled as three vertical faults (Camp Rock/Emerson, Homestead Valley, and Landers/Johnson Valley from north to south) with 186 subfaults and a maximum slip near 7 m [*Wald and Heaton*, 1994]. A single fault plane with 196 subfaults and a maximum slip of about 3 m is employed for the Northridge earthquake [*Wald et al.*, 1996]. The M_w 6.1 Joshua Tree preshock and M_w 6.2 Big Bear aftershock of the Landers sequence are modeled as single dislocations of 12 to 15 km diameter (from the inferred

rupture lengths of *Hauksson et al.* [1993]) and average slip of 0.35 m. The smaller aftershocks are not modeled because it is impractical to do so and because their effects on the stress field are small compared to those of larger events.

The changes in the stress tensor at the hypocenters of the aftershocks are calculated using the subroutines of *Okada* [1992], assuming the half-space is a Poisson solid with a shear modulus of 3 GPa. We resolve the change in the stress tensor onto the two nodal planes of each aftershock and calculate the Coulomb stress change on each plane.

We then compute the Coulomb index, the percent of aftershocks in an aftershock sequence consistent with static stress change triggering. An aftershock is considered to be consistent with static stress change triggering if it occurred on a plane with $\Delta CS > 0$. Aftershocks with positive ΔCS on both nodal planes are clearly consistent with static stress change triggering, while those with negative ΔCS on both planes are clearly inconsistent. We initially assume that 50% of the events with only one $\Delta CS > 0$ nodal plane occurred on the plane with the static stress increase, and vary this parameter during error estimation. (Since the shear stress changes on the two nodal planes are always the same, fewer than 20% of all events fall into this ambiguous category.)

A confidence interval for the Coulomb index of an aftershock sequence is obtained via a bootstrapping technique. We resample the observed sequence 500 times, with replacement, with the focal mechanism parameters randomly chosen from their confidence intervals. The fraction of events with only one $\Delta CS > 0$ plane considered consistent with triggering is chosen from a binomial distribution with a mean of 0.5. The 2σ confidence interval is obtained from the distribution of the Coulomb indices of the resampled sequences.

4.4.3 Random Synthetic Sequences

We test the static stress change triggering model by comparing the Coulomb indices of the observed sequences with the Coulomb indices of random synthetic sequences (e.g., Figure 4.4). The synthetic sequences serve as a control group, separating the effects of basic aftershock sequence geometry on Coulomb index from the effects of triggering. The synthetic sequences are designed to geometrically resemble aftershock sequences in that the events are clustered around the mainshock fault plane and in seismogenic depth ranges.

Each parameter of a synthetic event is chosen randomly from a plausible distribution of values. To facilitate creating the synthetic sequences, we use a somewhat unusual, mainshock-fault-plane-dependent coordinate system. The three coordinates are depth, strike direction distance, and normal distance to the fault plane (Figure 4.5). Each coordinate is chosen randomly and independently for the events in a synthetic sequence, with the probability distributions as shown in Figure 4.6a-Figure 4.6f. Because aftershocks also occur in spatial clusters, ~25% of the synthetic events are placed in clusters. The first event in a cluster is located randomly using the given probability distributions, and the locations of the subsequent events are determined by perturbing the parameters. The focal mechanisms are also chosen randomly, the P axis trend and P and T axis plunges selected independently with the probability distributions shown in Figure 4.6g-Figure 4.6l. Magnitudes are randomly assigned assuming a Gutenberg-Richter distribution.

The probability distribution functions are created using the relevant parameters of the observed aftershock sequences as guides. These parameters are as follows: how fast the synthetic seismicity drops off as one goes away from the fault, the seismogenic depth

ranges, the kinds of focal mechanisms, and the b values. We do not generate the synthetic sequences by resampling the observed hypocenters or attempt to recreate the details of the observed sequences. We wish to include synthetic events in areas which are unrepresented in the observed sequences (perhaps due to inhibiting static stress changes) and avoid bias towards areas of aftershock clusters (possibly areas of encouraging stress changes.)

The Coulomb indices of 500 synthetic sequences are calculated in the same way as the Coulomb indices of the observed sequences. All of the synthetic events with two $\Delta CS > 0$ nodal planes and a random fraction of events with only one $\Delta CS > 0$ nodal plane are considered consistent with triggering.

4.4.4 Statistical Test

We perform a simple statistical test of the null hypothesis that the Coulomb index of the observed sequence is no greater than the Coulomb indices of the synthetic sequences. Since this is a one-tailed test, the null hypothesis can be rejected at the 95% confidence level if the Coulomb index of the observed sequence is greater than the Coulomb indices of 95% of the synthetic sequences.

We include the error estimate for the Coulomb index of the observed sequence by taking the average confidence level determined from the bootstrap resamplings. This can be expressed as a weighted average of the confidence levels corresponding to each possible observed Coulomb index

$$CL = \sum_{CI=0}^{100} O(CI)S(CI) \qquad \text{(EQ 4.2)}$$

where CL is the average confidence level of rejecting the null hypothesis. O(CI) is the fraction of observed sequence resamplings with a Coulomb index of CI (the weight), and S(CI) is the cumulative fraction of synthetic sequences with a Coulomb index less than CI (the corresponding confidence level.) If CL ≥ 95%, the null hypothesis can be rejected, and we can conclude that the static stress change triggering model explains the aftershocks better than it does a random set of events.

Repeated trials with the Landers dataset indicate that CL is stable to within ±2%. Therefore, we consider CL ≥ 97% firm basis to reject the null hypothesis, and 93% ≤ CL < 97% to be ambiguous.

4.5 Results

Both the Landers and Northridge sequences include events consistent and inconsistent with static stress change triggering. These have generally indistinguishable distributions of hypocenters and mechanisms. The spatial mixture of aftershocks consistent and inconsistent with static stress change triggering can be seen in the map views and fault-normal cross sections in Figure 4.2 and Figure 4.3. Many events inconsistent with static stress triggering appear to concentrate around the mainshock fault planes, which may be explained by limitations of the data and models, as discussed later. Events consistent and inconsistent with triggering also have similar focal mechanisms, as illustrated by the stereographic projections of the tensional and compressional axes (Figure 4.7). The mechanisms are consistent with the inferred first-order southern California stress field of NNE trending compression [e.g., *Zoback and Zoback*, 1980].

Approximately 65% of the Landers and 60% of the Northridge aftershocks occurring within a month of the mainshock are consistent with static stress change triggering. The null hypothesis, that the Coulomb index of the observed sequence is no greater than the Coulomb indices of the synthetic sequences, can be rejected at the 95% confidence level for the Landers sequence, indicating that static stress change triggering is a useful model in explaining that sequence. However, the null hypothesis cannot be rejected at the 95% confidence level for the Northridge sequence, or any of its subsets we tested. The null hypothesis could be rejected for the Northridge sequence (for $\mu = 0.4$) with only 75% confidence. Since there are 1200 events in our Northridge data set, we interpret this as a failure of the model, not as a case of insufficient data to test the hypothesis.

The quantitative results for all the data subsets tested are shown in Figure 4.8 and are summarized in Table 4.1. We find that the results are independent of aftershock magnitude and time after the mainshock. Varying μ also does not make a significant difference to our results, since the null hypothesis can be rejected for the Landers sequence and cannot be rejected for the Northridge sequence for most tested values of μ (Figure 4.8a and Figure 4.8b). The only possible exceptions are for the Landers data with $\mu = 0.8$ or $t \leq$ 2 days, for which the confidence level is in the ambiguous region.

For the Landers sequence, the null hypothesis cannot be rejected at the 95% confidence level for aftershocks less than 5 km or greater than 75 km from the mainshock fault plane (Figure 4.8e), or for aftershocks with $|\Delta CS| < 0.01$ MPa or $|\Delta CS| > 0.5$ to 1 MPa (Figure 4.8g). This means that the static stress change triggering model is not useful close to the fault where stress changes are high or far from the fault where stress changes are

low. Between these extremes, ~85% of the aftershocks and 50% of the synthetics events are consistent with static stress change triggering.

The Coulomb index is found for 4.5 years of seismicity both preceeding and following the Landers mainshock (Figure 4.9). The premainshock events serve as a control group reflecting regional seismicity patterns independent of mainshock-induced static stress changes, although they may not be an ideal control because they may reflect processes leading up to the mainshock. The Coulomb index of pre-event seismicity is consistently 50 ± 8, while that of the aftershocks is 65 ± 8. There is no detectable decrease in Coulomb index in the 4.5 years following the mainshock, indicating that mainshock-induced static stress changes can be useful in explaining regional seismicity for at least that long.

4.6 Discussion

We find that the aftershocks consistent and inconsistent with triggering by static stress changes are spatially mixed, with a majority of aftershock mechanisms in agreement with the first-order regional stress field. Because mainshock-induced static stress changes are very small, they are more likely to trigger earthquakes on planes already close to failure. These planes are presumably primarily loaded by tectonic stresses, and so it is not surprising that they fail oriented with the regional stress field.

The static stress change triggering model is useful in explaining the first month of the Landers aftershock sequence but not the first month of the Northridge sequence. This difference is not because the stress changes from the Landers mainshock are a stronger signal, since for the same range of stress changes, 0.01 to 0.5 MPa, the model works well for the Landers sequence and not for Northridge.

However, the static stress changes due to the Landers mainshock may be a stronger signal relative to the local background stress and failure stress of faults. *Hauksson* [1994] inferred that the Eastern California Shear Zone is a weak zone, supporting low shear stresses, based on stress inversions indicating that the northern part of the Landers rupture relieved nearly all of the applied shear stress. The stress field inferred from Northridge aftershocks [e.g., *Zhao et al.*, 1997; *Kerkela and Stock*, 1996], on the other hand, implies that the Northridge earthquake was not a complete stress drop event, and hence that fault is relatively strong. Faults in thrust regimes are generally expected to support higher stresses because the overburden pressure is the minimum principal stress, whereas in strike-slip regimes one of the horizontal principal stresses is less than the overburden.

If the Landers area is relatively weak, and static stress triggering is observed there but not at Northridge, this implies that static stress changes may be too small to trigger a detectable number of events except in relatively weak areas. Presumably, this is because the small stress changes are a more significant fraction of the failure stress of a weak fault.

The difference between the results from the two sequences may also be due in part to limitations of the modeling. Approximating the Earth as a homogeneous elastic half-space may be appropriate for the Landers sequence because the Eastern California Shear Zone is relatively homogeneous on a 85 km length scale but inappropriate for the Northridge sequence, which is partially in the Transverse Ranges and partially in the San Fernando Valley. The Northridge mainshock was also smaller and did not rupture the surface, so there may be more error in the modeling of mainshock slip.

Regardless of its source, the difference between the results for the Landers and Northridge sequences implies that, although the static stress change triggering model can

be useful in explaining aftershock triggering, it is not consistently applicable for different events. This is also indicated by the variability of the results from other studies.

A study of larger events found that the model performs much better than it does in this study. *Harris et al.* [1995] studied 16 pairs of $M \geq 5$ southern California earthquakes occurring less than 1.5 years apart, 5 km distant, and with $|\Delta CS|$ on the plane of the second event due to the first at least 0.01 MPa. They find that 15 event pairs, or 94%, have $\Delta CS > 0$ on the failure plane of the second event.

In other studies, 70% to 75% of the first few months of Northridge aftershocks have been found to be consistent with static stress change triggering [*Simpson et al.*, 1994; *Harris et al.*, 1994], a greater percentage than we find for the first month of aftershocks. The difference may be due in part to the use of different criteria, the other studies consider consistent with triggering all events with at least one $\Delta CS > 0$ nodal plane, and in part to the use of different events.

Beroza and Zoback [1993] and *Kilb et al.* [1997] study the Loma Prieta sequence and conclude that mainshock-induced static stress changes do not adequately explain the individual aftershock mechanisms. However, the poor performance of the model may be because many Loma Prieta aftershocks occur very close to the mainshock rupture. It appears that the Loma Prieta aftershocks consistent with mainshock-induced shear increase are generally farther away from the major slip patches, while those inconsistent are closer to these patches [see *Beroza and Zoback*, 1993, Figure 3], consistent with the observation that the static stress triggering model does not work very close to the main-shock.

The presence of a minimum distance for which static stress change appears to be a viable triggering mechanism for Landers and other sequences need not reflect any physical process; it may merely reflect limitations of the data and models used. The slip models lack small-scale detail and are discretized, affecting the computed value of ΔCS for events near the fault plane. Location errors may also be more important for events close to the fault plane than for those farther away. Other studies also find or assume that the static stress change triggering model shouldn't be used closer to the fault than a few km [e.g., *Harris et al.*, 1995; *King et al.*, 1994].

The minimum Coulomb stress change for which the model appears to be valid for the Landers sequence, 0.01 MPa, is similar to values found in other studies: 0.01 MPa for Loma Prieta [*Reasenberg and Simpson*, 1992], 0.01 to 0.03 MPa for Landers [*King et al.*, 1994], and 0.02 MPa for Double Springs Flat, Nevada [*Jaumé*, 1996]. The corresponding maximum distance from the fault plane, 75 km, or approximately one fault length, however, is smaller than those determined from seismicity rates: 80 to 100 km, or about two fault lengths, for Loma Prieta [*Reasenberg and Simpson*, 1992], and about three fault lengths for Landers [*King et al.*, 1994].

There is no theoretical reason why a minimum stress change capable of triggering should exist, and it seems reasonable that an arbitrarily small static stress increase should be able to trigger an earthquake on a plane arbitrarily close to failure. A possible explanation for the existence of an apparent minimum triggering stress is that smaller static stresses trigger so few events that they are undetectable with the data sets used.

The effects of the static stress changes on regional seismicity appear to continue for at least 4.5 years after the Landers mainshock. This is longer than the 1.5 year interval

found by *Harris et al.* [1995] for $M \geq 5$ events but considerably shorter than the decades which can pass between larger events postulated to be linked by static stress changes [e.g., *Stein et al.*, 1992; *King et al.*, 1994; *Stein et al.*, 1994; *Jaumé and Sykes*, 1996; *Deng and Sykes*, 1997].

Although coseismic static stress changes are essentially instantaneous, the aftershocks triggered by them do not necessarily occur immediately after the mainshock. A static stress increase could advance the time of an earthquake, which may then occur in the following months or years. Additionally, postseismic relaxation at depth may continue to load the brittle upper crust in the same patterns as the coseismic static stress changes [e.g., *King et al.*, 1994]. The rate- and state-dependent seismicity model of *Dieterich* [1994] also explains how a static stress change can produce an Omori's law temporal distribution of aftershocks.

The poor performance of the static stress change triggering model for the Northridge sequence and the presence of many aftershocks in the Landers sequence not consistent with static stress change triggering imply that there are other triggering mechanisms involved. Other triggering models, primarily proposed for far-field triggering, include dynamic strains [e.g., *Anderson et al.*, 1994; *Hill et al.*, 1993], transient changes in pore pressure due to dynamic strains [e.g., *Hill et al.*, 1993], long-term changes in pore pressure due to pore-fluid movements after fluid seals are broken [e.g., *Hill et al.*, 1993], and increases in pore pressure by dynamic strains via rectified diffusion [*Sturtevant et al.*, 1996].

4.7 *Conclusions*

The static stress change triggering model has been quantitatively evaluated for the 1992 Landers and 1994 Northridge aftershock sequences. Specifically, we test whether the fraction of aftershocks consistent with static stress change triggering is significantly greater than the fraction of random events which would appear consistent by chance.

We find that the model is useful in explaining the Landers aftershocks, particularly those which are not too close to ($d < 5$ km or $|\Delta CS| > 0.5$ to 1 MPa) or too far from ($d > 75$ km or $|\Delta CS| < 0.01$ MPa) the mainshock fault plane. However, the model is not useful in explaining the first month of the Northridge sequence. The difference between the two sequences may be due to differences in tectonic regime and stress state, with weaker faults in the Landers region being more susceptible to triggering by small stress increases.

Our results suggest that the static stress change triggering model has some validity and can be useful in explaining apparently triggered seismicity within one fault length of a large mainshock. However, because its applicability varies between different sequences, its general application to seismic hazard evaluation requires more refinement and the inclusion of parameters such as tectonic regime, regional stress state, and fault strength.

4.8. References

Anderson, J. G., J. N. Brune, J. N. Louie, Y. Zeng, M. Savage, G. Yu, Q. Chen, and D. dePolo, Seismicity in the western Great Basin apparently triggered by the Landers, California, earthquake, 28 June 1992, *Bull. Seismol. Soc. Am.*, *84*, 863-891, 1994.

Beroza, G. C., and M. D. Zoback, Mechanism diversity of the Loma Prieta aftershocks and the mechanics of mainshock-aftershock interaction, *Science*, *259*, 210-213, 1993.

Byerlee, J. D., Friction of rock, *Pure Appl. Geophys.*, *116*, 615-626, 1978.

Deng, J., and L. R. Sykes, Evolution of the stress field in southern California and triggering of moderate-size earthquakes: A 200-year perspective, *J. Geophys. Res.*, *102*, 9859-9886, 1997.

Dieterich, J., A constitutive law for rate of earthquake production and its application to earthquake clustering, *J. Geophys. Res.*, *99*, 2601-2618, 1994.

Harris, R. A., and R. W. Simpson, Changes in static stress on southern California faults after the 1992 Landers earthquake, *Nature*, *360*, 251-254,1992.

Harris, R. A., R. W. Simpson, and P. A. Reasenberg, Static stress changes influence future earthquake locations in southern California (abstract), *Eos Trans AGU*, *75* (44), Fall Meet. Suppl., 169, 1994.

Harris, R. A., R. W. Simpson, and P. A. Reasenberg, Influence of static stress changes on earthquake locations in southern California, *Nature*, *375*, 221-224, 1995.

Hauksson, E., State of stress from focal mechanisms before and after the1992 Landers earthquake sequence, *Bull. Seismol. Soc. Am.*, *84*, 917-934, 1994.

Hauksson, E., L. M. Jones, K. Hutton, and D. Eberhart-Phillips, The 1992 Landers earthquake sequence: Seismological observations, *J. Geophys. Res.*, *98*, 19835-19858, 1993.

Hauksson, E., L. M. Jones, and K. Hutton, The 1994 Northridge earthquake sequence in California: Seismological and tectonic aspects, *J. Geophys. Res.*, *100*, 12335-12355, 1995.

Hill, D. P., et al., Seismicity remotely triggered by the magnitude 7.3 Landers, California, earthquake, *Science*, *260*, 1617-1623, 1993.

Jaumé, S. C., Just how much static stress does it take to trigger an aftershock? (abstract), *Eos Trans AGU*, *77* (46), Fall Meet. Suppl., F500, 1996.

Jaumé, S. C., and L. R. Sykes, Changes in state of stress on the southern San Andreas fault resulting from the California earthquake sequence of April to June 1992, *Science*, *258*, 1325-1328, 1992.

Jaumé, S. C., and L. R. Sykes, Evolution of moderate seismicity in the San Francisco Bay region, 1850 to 1993: Seismicity changes related to the occurrence of large and great earthquakes, *J. Geophys. Res.*, *101*, 765-789, 1996.

Kagan, Y. Y., Incremental stress and earthquakes, *Geophys. J. Int.*, *117*, 345-364, 1994.

Kerkela, S., and J. M. Stock, Compression directions north of the San Fernando Valley determined from borehole breakouts, *Geophys. Res. Lett.*, *23*, 3365-3368, 1996.

Kilb, D., M. Ellis, J. Gomberg, and S. Davis, On the origin of diverse aftershock mechanisms following the 1989 Loma Prieta earthquake, *Geophys. J. Int.*, *128*, 557-570, 1997.

King, G. C. P., R. S. Stein, and J. Lin, Static stress changes and the triggering of earthquakes, *Bull. Seismol. Soc. Am.*, *84*, 935-953, 1994.

Kissling, E., W. L. Ellsworth, D. Eberhart-Phillips, and U. Kradolfer, Initial reference models in local earthquake tomography, *J. Geophys. Res.*, *99*, 19,635-19,646, 1994.

Klein, F. W., User's guide to HYPOINVERSE; A program for VAX and PC350 computers to solve for earthquake locations, *U.S. Geol. Surv. Open File Rep., 85-159*, 24 pp., 1985.

Okada, Y., Internal deformation due to shear and tensile faults in a half-space, *Bull. Seismol. Soc. Am., 82*, 1018-1040, 1992.

Reasenberg, P., and D. Oppenheimer, FPFIT, FPPLOT and FPPAGE: FORTRAN computer programs for calculating and displaying earthquake fault-plane solutions, *U.S. Geol. Surv. Open File Rep., 85-739*, 109 pp., 1985.

Reasenberg, P. A., and R. W. Simpson, Response of regional seismicity to the static stress change produced by the Loma Prieta earthquake, *Science, 255*, 687-1690, 1992.

Simpson, R. W., and P. A. Reasenberg, Earthquake-induced static stress changes on central California faults, *in The Loma Prieta,California, Earthquake of October 17, 1989-Tectonic Processes and Models*, edited by R. W. Simpson, *U.S.Geol. Surv. Prof. Pap., 1550-F*, F55-F89, 1994.

Simpson, R. W., R. A. Harris, and P. A. Reasenberg, Stress changes caused by the 1994 Northridge earthquake, paper presented at the1994 SSA Meeting, Seismol. Soc. of Am., Pasadena, 1994.

Stein, R. S., G. C. P. King, and J. Lin, Change in failure stress on the southern San Andreas fault system caused by the 1992 magnitude = 7.4 Landers earthquake, *Science, 258*, 1328-1332, 1992.

Stein, R. S., G. C. P. King, and J. Lin, Stress triggering of the 1994 M=6.7 Northridge, California, earthquake by its predecessors, *Science, 265*, 1432-1435, 1994.

Sturtevant, B., H. Kanamori, and E. E. Brodsky, Seismic triggering by rectified diffusion in geothermal systems, *J. Geophys. Res., 101*, 25,269-25,282, 1996.

Wald, D. J., and T. H. Heaton, Spatial and temporal distribution of slip for the 1992 Landers, California earthquake, *Bull. Seismol. Soc. Am.*, *84*, 668-691, 1994.

Wald, D. J., T. H. Heaton, and K. W. Hudnut, The slip history of the 1994 Northridge, California, earthquake determined from strong-motion, teleseismic, GPS, and leveling data, *Bull. Seismol. Soc. Am.*, *86*, S49-S70, 1996.

Zhao, D., H. Kanamori, and D. Wiens, State of stress before and after the 1994 Northridge earthquake, *Geophys. Res. Lett.*, *24*, 519-522, 1997.

Zoback, M. L., and M. Zoback, State of stress in the conterminous United States, *J. Geophys. Res.*, *85*, 6113-6156, 1980.

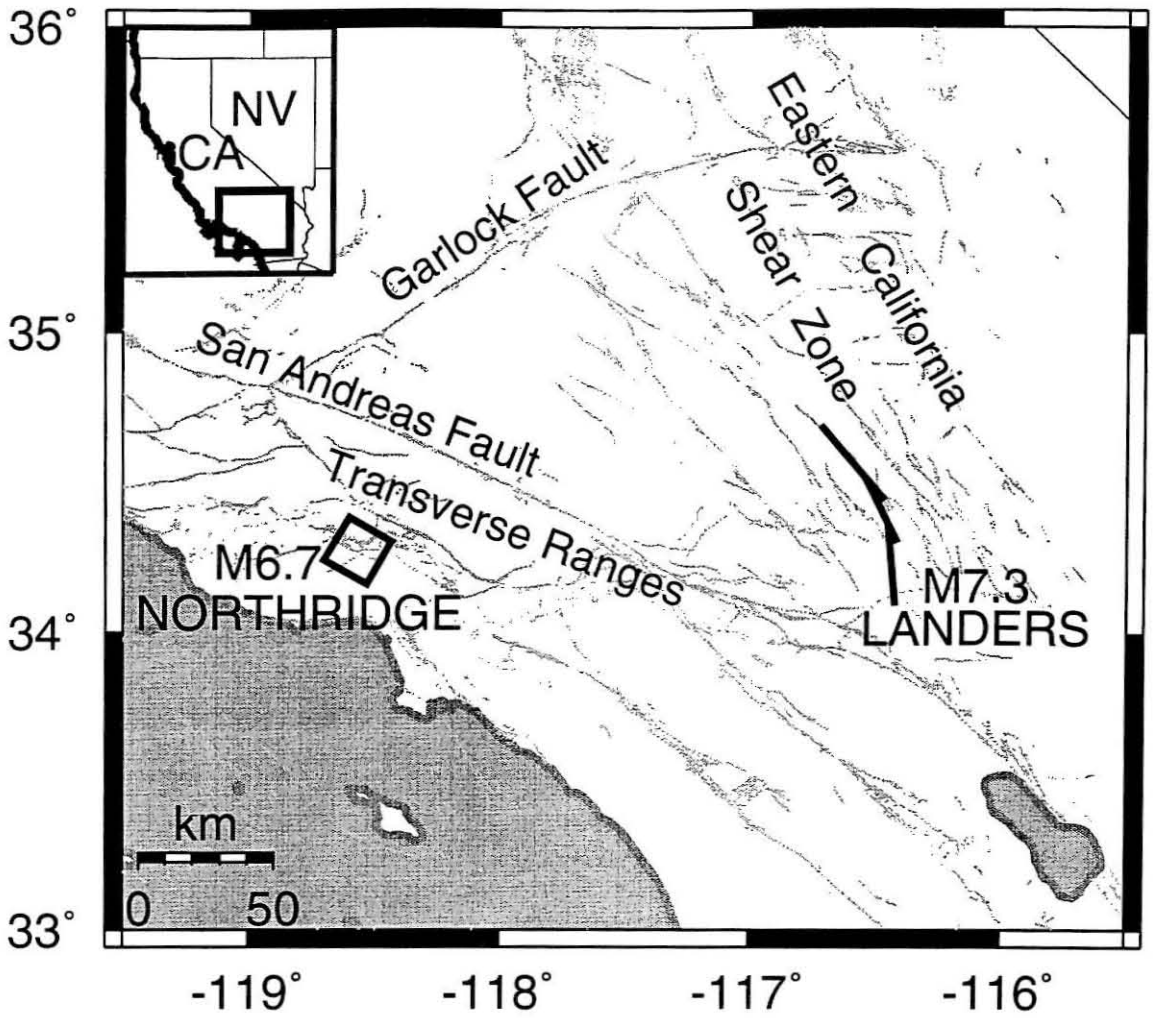

Figure 4.1 **Map of southern California showing the Landers and Northridge mainshocks. Surface projections, solid, from rupture models of *Wald and Heaton* [1994] and *Wald et al.* [1996]. Traces of mapped faults shown shaded.**

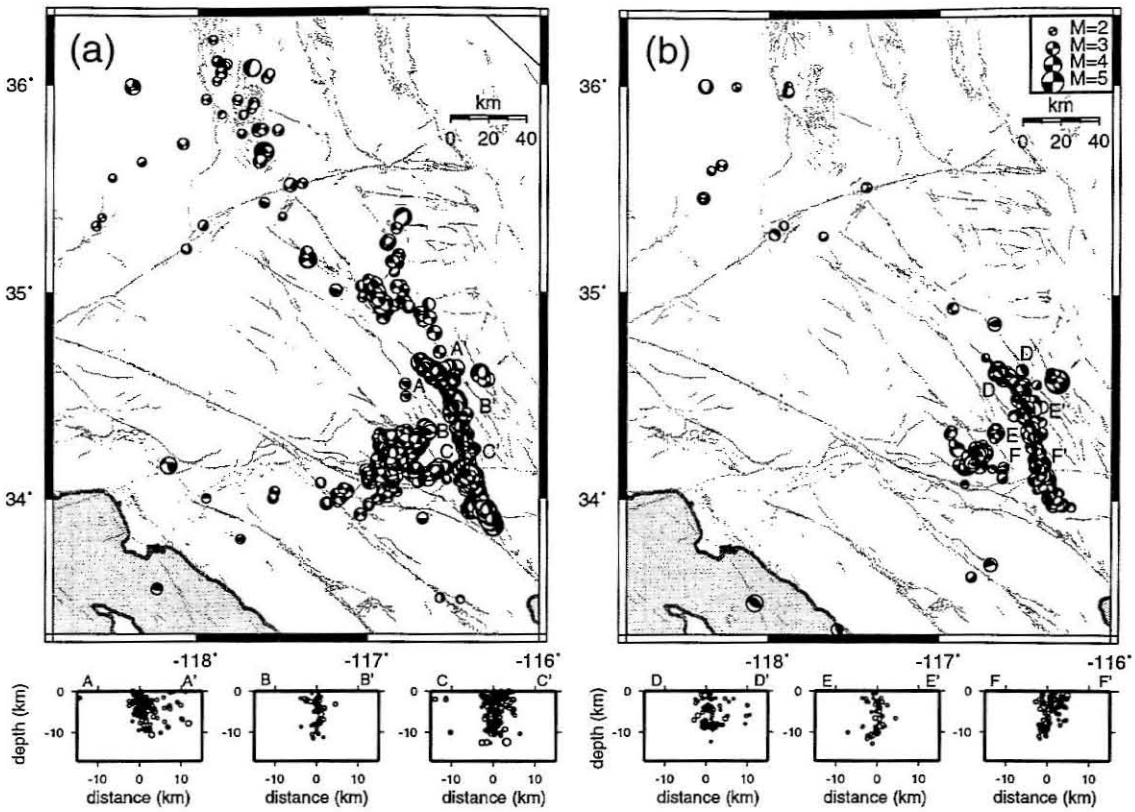

Figure 4.2 **Map view and cross sections of the first month of Landers aftershocks used in this study. (a) Aftershocks with at least one plane consistent with static stress change triggering. (b) Aftershocks with both planes inconsistent. Here $\mu' = 0.4$. Mapped faults shown shaded. The mainshock fault plane (adapted from *Wald and Heaton* [1994]) is indicated with solid lines.**

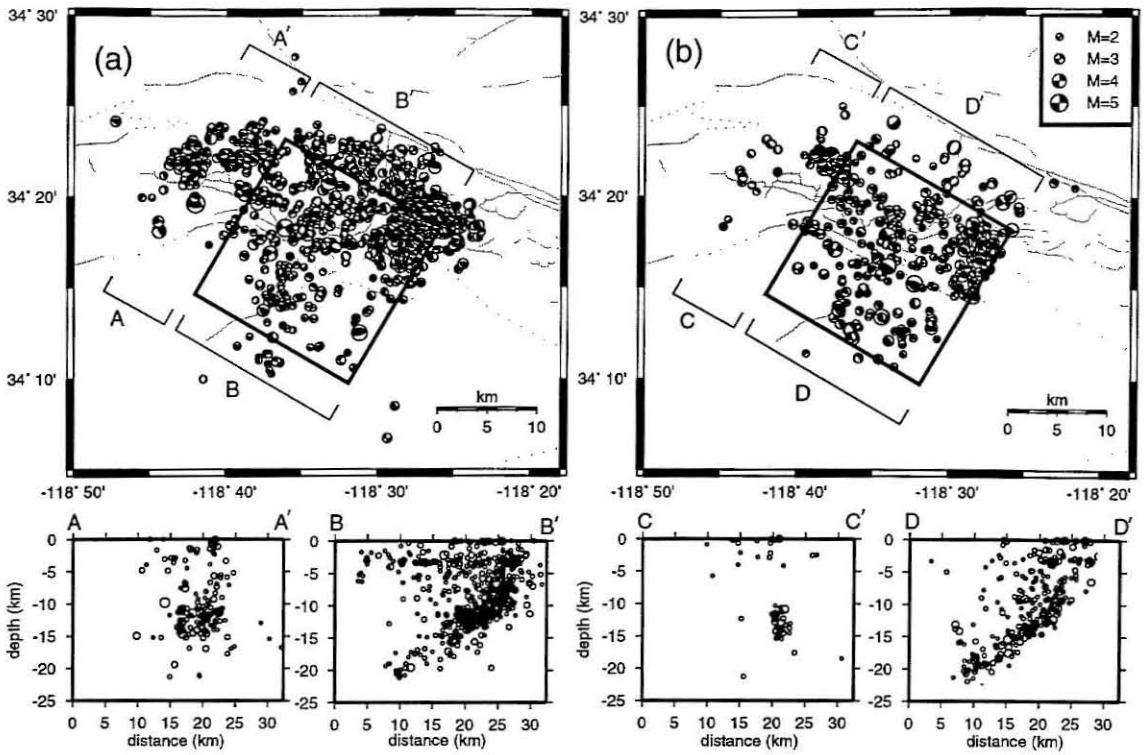

Figure 4.3 **Map view and cross sections of the first month of Northridge aftershocks used in this study. (a) Aftershocks with at least one plane consistent with static stress change triggering. (b) Aftershocks with both planes inconsistent. Here $\mu' = 0.4$. Mapped faults are shown shaded. The projection of the mainshock fault plane (adapted from *Wald et al.* [1996]) is shown as a solid rectangle.**

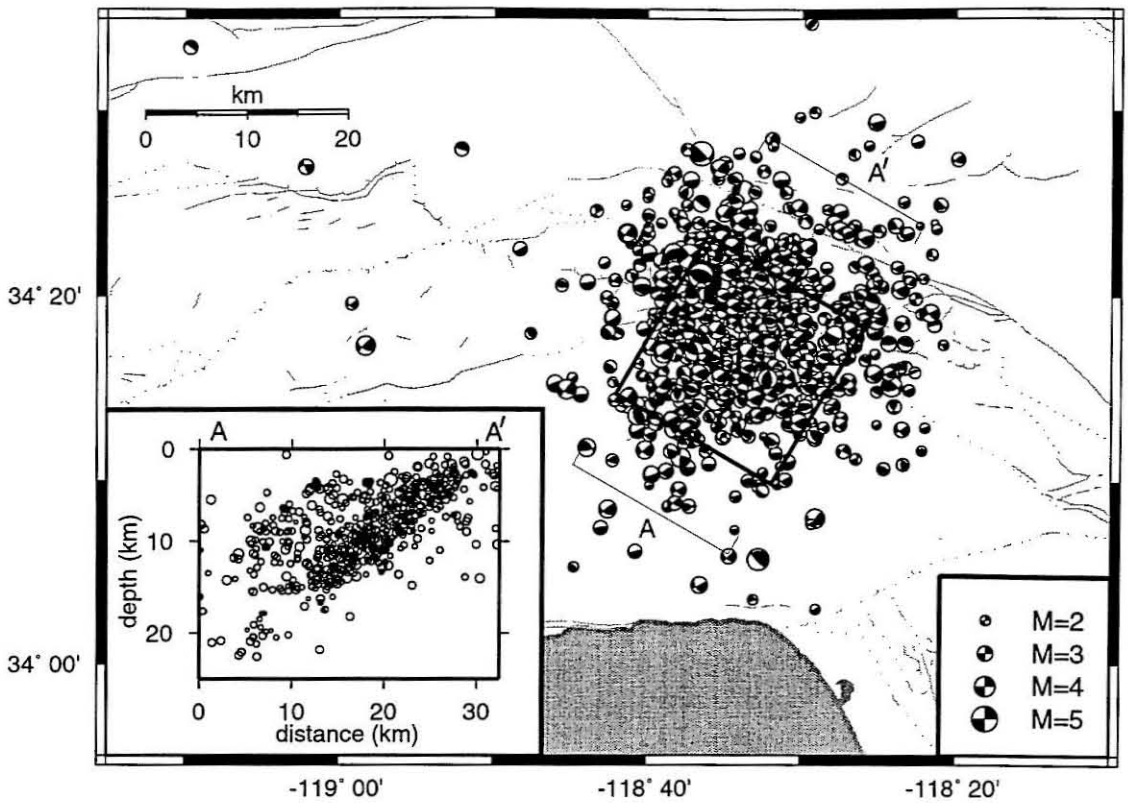

Figure 4.4 A random synthetic sequence of events for Northridge, shown in map view and fault-normal cross section. The projection of the mainshock slip plane (adapted from *Wald et al.* [1996]) is shown as a rectangle in map view.

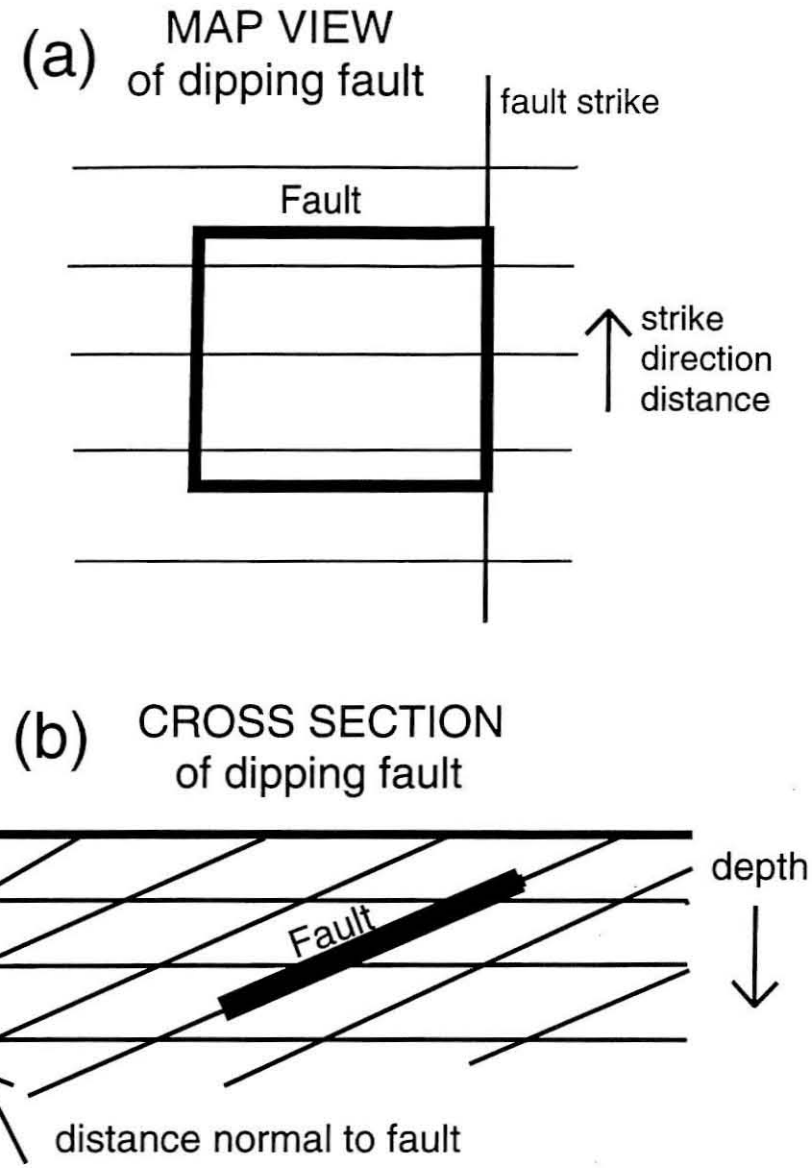

Figure 4.5 Cartoon (a) map view and (b) fault-normal cross section of a dipping rectangular fault which illustrates the coordinate system used in defining aftershock locations: depth, strike direction distance, and normal distance from the fault plane.

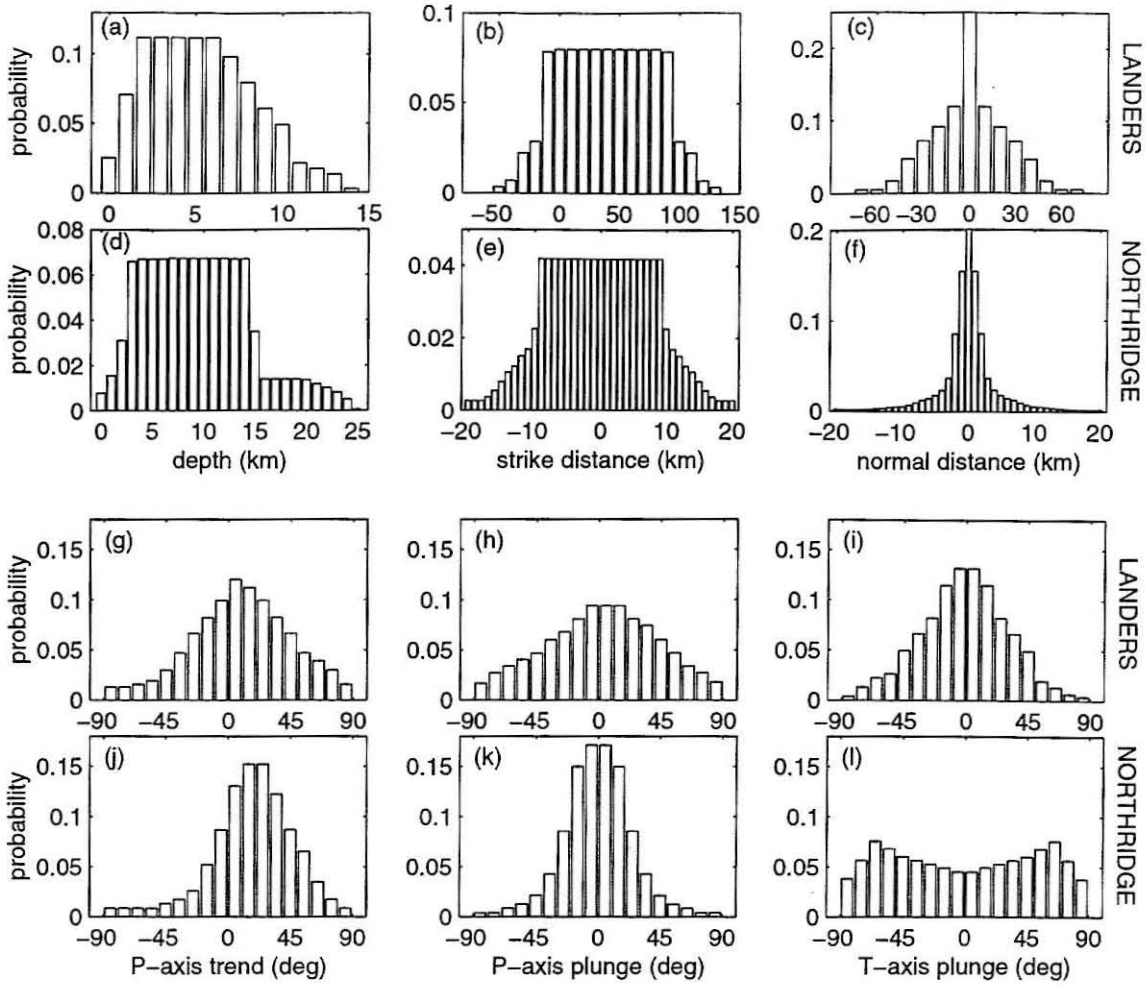

Figure 4.6 Probability distribution of synthetic event coordinates: (a)-(c) Landers sequence spatial coordinates, (d)-(f) Northridge sequence spatial coordinates, (g)-(i) Landers sequence focal mechanism parameters, (j)-(l) Northridge sequence focal mechanisms parameters. The spatial coordinates are as shown in Figure 4.5. The strike distance is measured east from the center of the Northridge fault and north from the southern tip of the Landers fault, with the approximation that the three fault segments are end-to-end, and normal distance is measured from the nearest segment or its extension. The *P* axis trend is measured clockwise from north, and the plunge is down from horizontal. The *T* axis plunge is positive for a clockwise rotation about the *P* axis.

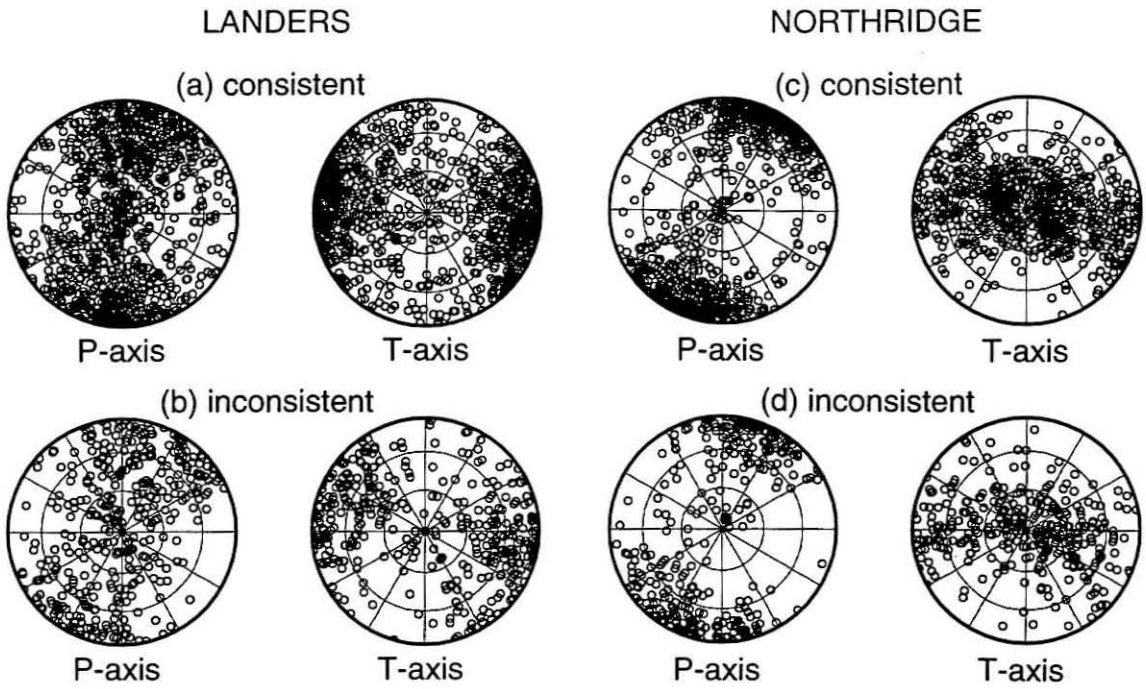

Figure 4.7 **Stereographic plots of the compressional (*P*) and tensional (*T*) axes of the first month of aftershocks. Here $\mu' = 0.4$. (a) Landers aftershocks with at least one plane consistent with static stress change triggering. (b) Landers aftershocks with both planes inconsistent. (c) Northridge aftershocks with at least one plane consistent. (d) Northridge aftershocks with both planes inconsistent.**

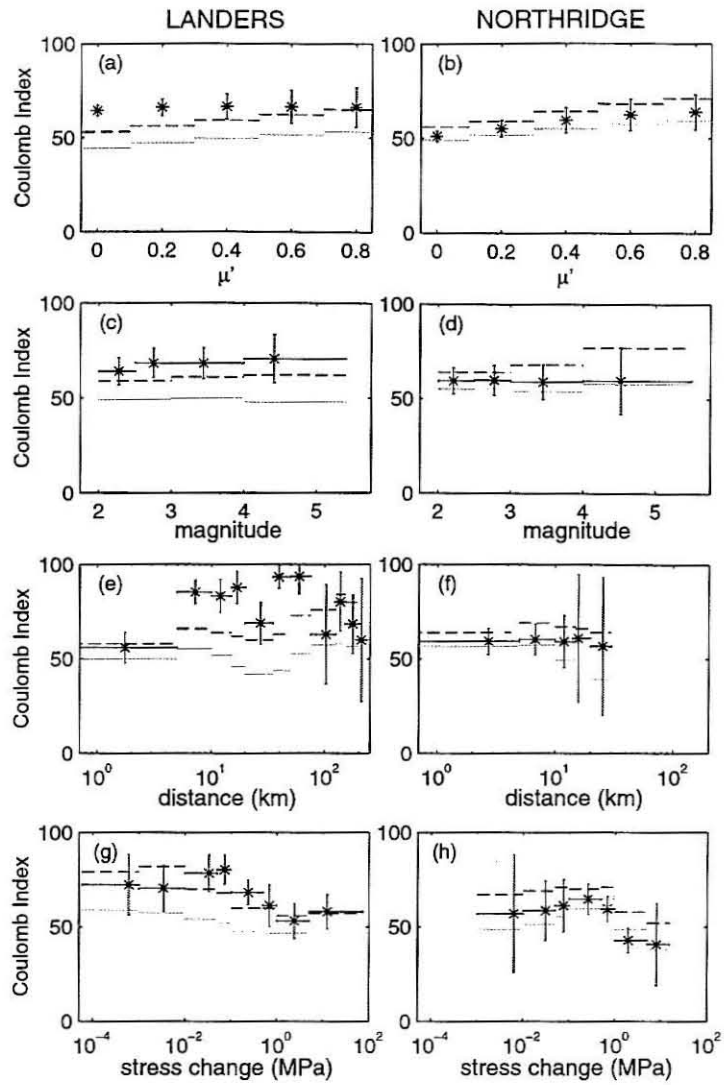

Figure 4.8 **Coulomb index (CI), the percent of events consistent with static stress change triggering, versus various parameters. The asterisks indicate the Coulomb index for a bin versus the mean parameter value of events in that bin. The vertical error bars are the 2σ error estimates, and the horizontal error bars indicate the bins. The horizontal dotted and dashed lines represent the mean Coulomb index of 100 random synthetic sequences and the division between the upper 5% and the lower 95%, respectively. If the Coulomb index of the observed sequence is above this dashed line, one can conclude with 95% confidence that the static stress change triggering model explains the aftershocks better than it can a random set of events. (Aftershocks from the first month are used. Here $\mu' = 0.4$ except in Figure 4.8a and Figure 4.8b.) (a) CI versus μ', Landers. (b) CI versus μ', Northridge. (c) CI versus aftershock magnitude, Landers. (d) CI versus magnitude, Northridge. (e) CI versus distance to the nearest point on a modeled rupture plane, Landers. (f) CI versus distance, Northridge. (g) CI versus stress change, $|\Delta CS|$, the average of the absolute values of the Coulomb stress changes on the two nodal planes, Landers. (h) CI versus $|\Delta CS|$, Northridge.**

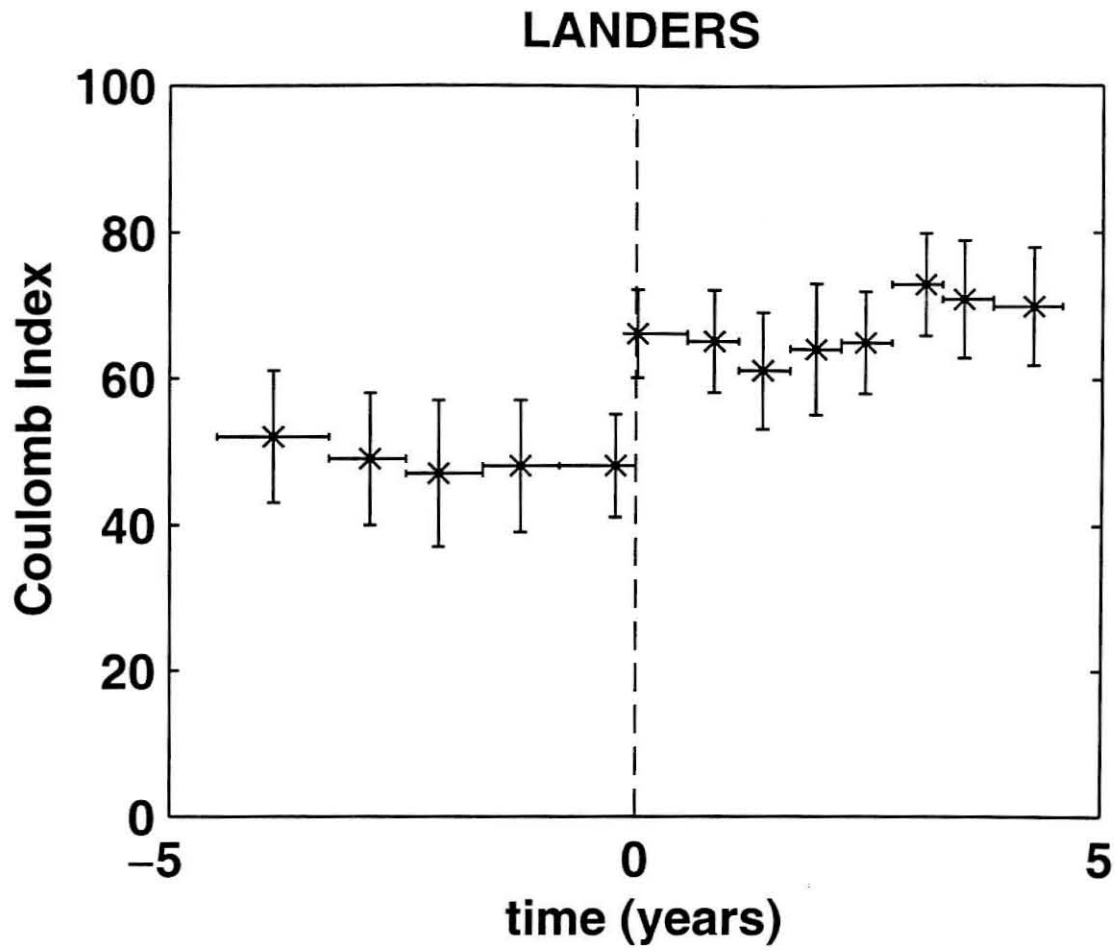

Figure 4.9 Coulomb index versus time in years for 4.5 years of seismicity preceeding and following the Landers mainshock. The vertical error bars are the 2σ error estimates and the horizontal error bars indicate the bins. The vertical dotted line indicates the time of the mainshock.

Table 4.1 Coulomb Index of First Month of Aftershock Sequences

Data Set or Parameter Value	Number of Events	Observed CI	Observed (±2σ)	Synthetic CI	Synthetic (±2σ)	Confidence Level	Number of Events	Observed CI	Observed (±2σ)	Synthetic CI	Synthetic (±2σ)	Confidence Level
μ'=0	1471	64	±3	45	±10	99%	1200	51	±3	49	±8	61%
μ'=0.2	1471	66	±4	47	±10	99%	1200	55	±4	52	±8	73%
μ'=0.4	1471	66	±7	49	±11	99%	1200	59	±7	55	±10	75%
μ'=0.6	1471	66	±9	52	±12	97%	1200	62	±8	57	±12	72%
μ'=0.8	1471	66	±10	53	±13	93%	1200	64	±9	59	±13	70%
M≤2.5	734	64	±7	49	±12	98%	741	59	±7	55	±11	73%
2.5<M≤3	416	68	±8	49	±12	99%	265	60	±8	56	±9	73%
3<M≤4	264	68	±8	50	±12	99%	163	59	±9	54	±15	70%
M>4	57	71	±13	48	±16	98%	31	60	±18	58	±23	52%
D≤5km	897	56	±8	50	±8	84%	883	59	±7	57	±8	64%
5<D≤10	225	85	±6	55	±12	99%	253	60	±8	57	±14	60%
10<D≤15	70	83	±9	52	±14	99%	48	59	±14	49	±21	77%
15<D≤20	54	88	±8	46	±19	99%	8	61	±34	38	±27	84%
20<D≤35	65	69	±11	42	±19	98%	7	57	±37	39	±27	77%
35<D≤50	60	93	±6	44	±24	99%	1	-	-	-	-	-
50<D≤75	20	94	±9	53	±26	99%	0	-	-	-	-	-
75<D≤125	14	63	±26	57	±22	63%	0	-	-	-	-	-
125<D≤150	23	80	±15	58	±29	90%	0	-	-	-	-	-
150<D≤200	33	69	±15	57	±27	78%	0	-	-	-	-	-
D>200	10	60	±32	55	±63	55%	0	-	-	-	-	-
$\lvert\Delta CS\rvert \leq 0.001$ MPa	29	72	±16	59	±24	81%	1	-	-	-	-	-
$0.001 < \lvert\Delta CS\rvert \leq 0.01$	65	70	±12	57	±24	86%	6	57	±31	49	±25	64%
$0.01 < \lvert\Delta CS\rvert \leq 0.05$	150	78	±10	54	±18	98%	58	59	±16	51	±21	68%
$0.05 < \lvert\Delta CS\rvert \leq 0.1$	160	80	±8	52	±18	99%	104	61	±14	55	±18	67%
$0.1 < \lvert\Delta CS\rvert \leq 0.5$	506	68	±7	48	±15	99%	649	65	±8	60	±12	73%
$0.5 < \lvert\Delta CS\rvert \leq 1$	119	61	±11	47	±15	93%	207	60	±7	61	±10	38%
$1 < \lvert\Delta CS\rvert \leq 5$	311	53	±9	47	±10	81%	156	43	±7	49	±9	13%
$\lvert\Delta CS\rvert > 5$	131	58	±9	44	±13	94%	19	41	±22	38	±16	56%
t≤2days	137	64	±10	49	±14	95%	345	60	±8	55	±13	71%
2<t≤7	359	68	±8	49	±12	99%	396	59	±7	55	±13	70%
7<t≤14	437	64	±7	49	±12	98%	279	60	±8	55	±14	72%
t>14	538	67	±7	49	±12	99%	180	60	±9	55	±14	69%